NASA CONTRACTOR REPORT

NASA CR-2554

NASA CR-2554

COMPARISON OF WIND-TUNNEL TEST RESULTS AT $M_\infty = 0.7$ WITH RESULTS FROM THE BOEING TEA-230 SUBSONIC FLOW METHOD

L. W. Mohn

Prepared by
BOEING COMMERCIAL AIRPLANE COMPANY
Seattle, Wash. 98124

for Langley Research Center

NATIONAL AERONAUTICS AND SPACE ADMINISTRATION • WASHINGTON, D. C. • JULY 1975

1. Report No.	2. Government Accession No.	3. Recipient's Catalog No.
NASA CR-2554		

4. Title and Subtitle	5. Report Date
COMPARISON OF WIND-TUNNEL TEST RESULTS AT $M_\infty = 0.7$ WITH RESULTS FROM THE BOEING TEA-230 SUBSONIC FLOW METHOD	July 1975
	6. Performing Organization Code D6-41780

7. Author(s)	8. Performing Organization Report No.
L. W. Mohn	
	10. Work Unit No.

9. Performing Organization Name and Address	11. Contract or Grant No.
Boeing Commercial Airplane Company P.O. Box 3707 Seattle, Washington 98124	NAS1-12214, Mod. 4
	13. Type of Report and Period Covered
12. Sponsoring Agency Name and Address	Contractor Report
National Aeronautics and Space Administration Washington, D. C. 20546	14. Sponsoring Agency Code

15. Supplementary Notes

Final Report

16. Abstract

A study was made to verify the use of the Boeing TEA-230 Subsonic Flow Analysis method as a primary design tool in the development of cruise overwing nacelle configurations under contract NAS1-12214 (already completed). Surface pressure characteristics at 0.7 Mach number were determined by the TEA-230 method for a selected overwing flow-through nacelle configuration. Results of this analysis showed excellent overall agreement with corresponding wind tunnel data. Effects of the presence of the nacelle on the wing pressure field were predicted accurately by the theoretical method. Evidence is provided that differences between theoretical and experimental pressure distributions in the present study would not result in significant discrepancies in the nacelle lines or nacelle drag estimates determined under contract NAS1-12214.

17. Key Words (Suggested by Author(s))	18. Distribution Statement
Potential flow analysis Wind tunnel data Pressure distribution Test-theory comparison Overwing nacelle	Unclassified–unlimited Subject Category 02

19. Security Classif. (of this report)	20. Security Classif. (of this page)	21. No. of Pages	22. Price*
Unclassified	Unclassified	91	$4.75

*For sale by the National Technical Information Service, Springfield, Virginia 22151

CONTENTS

FIGURES

FIGURES—Continued

FIGURES–Concluded

COMPARISON OF WIND-TUNNEL TEST RESULTS FROM $M_\infty = 0.7$ WITH RESULTS FROM THE BOEING TEA-230 SUBSONIC FLOW METHOD

by L. W. Mohn

1.0 SUMMARY

The underlying goal of this study was to verify the use of the Boeing TEA-230 Subsonic Flow Analysis method as a primary design tool in the development of cruise overwing nacelle configurations under contract NAS1-12214 (already completed). The technical approach taken in the present study was to demonstrate the capability of the TEA-230 computer program to determine the surface pressure characteristics at 0.7 Mach number of a selected overwing flow-through nacelle configuration. This capability is confirmed in the present study by comparisons with existing corresponding wind-tunnel test data.

Wing chordwise pressure distributions from theory and experiment are compared at eight spanwise stations for $M_\infty = 0.7$. Both wing-body and wing-body-nacelle data comparisons are made, and the results of the TEA-230 analysis show excellent overall agreement with the corresponding wind-tunnel data. Effects of the presence of the nacelle on the wing pressure field were also predicted with good accuracy. Some of the small differences between theory and experiment are interpreted in terms of limitations of the TEA-230 theory. For example, the theoretical model does not account for viscous or transonic Mach number effects. Minor discrepancies in the wind-tunnel model surface geometry are described and related to the test-theory data comparisons. Results are also presented to show the effects of Mach number ($M_\infty = 0.7$, 0.8, and 0.84) on the wing pressure data measured in the wind tunnel.

Theoretical and experimental data are included from supporting studies which provide evidence that the pressure differences between test results and theory presented herein would not result in significant discrepancies in the nacelle lines or nacelle drag estimates determined under contract NAS1-12214. The present study, therefore, adds a degree of confidence to the nacelle designs developed under the latter contract.

2.0 INTRODUCTION

The study documented in this report is an addition to NASA contract NAS1-12214, entitled "Upper-Surface-Blowing Nacelle Design Study for a Swept Wing Airplane at Cruise Conditions." Initial work under this contract was completed in May 1974 (ref. 1), and will be referred to in this report as the "main contract." In the main contract, two types of overwing nacelles were designed for an existing wing-body at a design Mach number of 0.8. The nacelle designs were based on an iterative process of aerodynamic potential-flow analysis, using the Boeing TEA-230 Subsonic Flow Analysis System (refs. 2 and 3). The goal of the design was the development of external nacelle lines that would minimize high-speed aerodynamic interference effects. Section 4.0 presents a brief review of the pertinent results of the main contract.

In the present contract study, the capability of the TEA-230 method to analyze a cruise wing-body-nacelle configuration of the type designed in the main contract was demonstrated. This capability was established by comparing existing wing pressure distributions from wind-tunnel tests with TEA-230 pressure distributions for wing-body and wing-body-nacelle configurations.

The airplane configuration selected for the comparison is one of many overwing nacelle arrangements designed and tested at Boeing. Detailed section shapes for this configuration are proprietary and are not included in this report. Such contour details are not, however, essential to the objectives of this study.

Section 5.0 presents the overall geometry of the configuration selected for this study, followed by wing pressure distributions from the wind-tunnel tests at free-stream Mach numbers of 0.7, 0.8, and 0.84. Section 6.0 compares the pressure and lift data measured in the wind tunnel at $M_\infty = 0.7$ with corresponding theoretical results from the TEA-230 Subsonic Flow method. Analysis of these test-theory comparisons is presented in section 7.0, including an assessment of the impact of any significant test-theory discrepancies on the nacelle lines and nacelle drag estimates developed in the main contract.

3.0 SYMBOLS

AR_{WING}	aspect ratio of wing
b	wing span, m (ft)
c	local wing chord, m (ft)
$\bar{c}$	reference chord - S_{ref}/b, m (ft)
C_D	drag coefficient = $D/q_\infty S_{ref}$
$\Delta C_{D_{MOD}}$	increment in drag coefficient due to geometry modification
$\Delta C_{D_{nac}}$	increment in drag coefficient due to addition of nacelle to configuration
C_ℓ	sectional wing lift coefficient, $L'/q_\infty c$
C_L	lift coefficient, $L/q_\infty S_{ref}$
$\mathcal{C}_L$	centerline of configuration geometry
C_p	pressure coefficient, $(p - p_\infty)/q_\infty$
$\Delta C_{p_{nac}}$	increment in pressure coefficient due to addition of nacelle to configuration
D	total drag, N (lb)
L	total lift, N (lb)
L'	local lift per unit span, N/m (lb/ft)
M_∞	flight Mach number (cruise or free stream)
M_{crit}	wing-body critical Mach number (occurs at $\Delta C_D = 0.0020$ above the C_D at $M_\infty = 0.7$ at constant C_L)
M_L	local Mach number
p	local pressure, N/m^2 (lb/ft^2)
p_∞	atmospheric pressure, N/m^2 (lb/ft^2)
q_∞	dynamic pressure, N/m^2 (lb/ft^2)
Re	Reynolds number = $\frac{\rho U_\infty c}{\mu}$

S_{ref}	reference wing area, m^2 (ft^2)
t	wing section thickness, m (ft)
U_∞	flight velocity (cruise or free stream), m/sec (ft/sec)
WBL	wing buttock line
WL	water line
x	coordinate along direction of free stream, m (ft)
ΔZ	increment in vertical ordinate, m (ft)
α	angle of attack, deg
η	fraction of wing semispan
λ	wing taper ratio = tip chord/root chord
$\Lambda c/4$	wing sweep at quarter-chord position, deg
μ	coefficient of viscosity
ρ	mass density, kg/m^3 ($slugs/ft^3$)

4.0 REVIEW OF MAIN CONTRACT: NAS1-12214

Reference 1 reports the work performed under NASA contract NAS1-12214 entitled "Upper-Surface-Blowing Nacelle Design Study for a Swept Wing Airplane at Cruise Conditions." Inasmuch as this main contract study was the basis for the additional study reported here, a brief review of the results of the main contract will be presented in this section.

During the main contract, upper-surface-blowing nacelles were designed for a given high-wing wind-tunnel model. The configurations represented two- and four-engine airplanes, with nacelles having D-nozzles or high aspect ratio rectangular nozzles. The objective of the design for each of the four configurations was to develop a practical overwing nacelle external geometry that would have a minimum adverse impact on high-speed performance. The wind-tunnel model nacelles were designed as flow-through configurations, with the external lines representing the full-scale nacelle external lines. Ground rules for the designs were:

- Total airplane thrust 178 000 to 356 000 N (40 000 to 80 000 lb)
- Field length 610 to 915 m (2000 to 3000 ft)
- Noise goal 95 EPNdB at 153 m (500 ft)
- Cruise Mach number 0.80.

The general arrangement of each airplane configuration was determined before the detailed aerodynamic design of the nacelles was begun. These preliminary design studies took into account various real-airplane considerations such as weights, structures, and stability and control, in addition to the basic aerodynamic and propulsion considerations. The primary design rule was to design the nacelle inboard contours along wing-body streamlines and allow the nacelle outboard contours to develop in accordance with the required nacelle internal volume. The spanwise location of these nacelles was selected to provide optimum coverage of the trailing-edge flap by the exhaust flow.

Evaluations of the designs were made in light of the TEA-230 aerodynamic analyses and corresponding Boeing experience. Theoretical pressure distributions on the wing and nacelle, configuration isobar plots, and wing sectional lift and span-load distributions were computed at $M_\infty = 0.7$ and indicated that, at that design condition, the nacelle geometries achieved the design goals. In some cases, the initial nacelle design required modification to provide acceptable aerodynamic characteristics. The pressure levels and gradients calculated along the final nacelle surfaces were reasonably well behaved for both D-nozzle and spread nozzle nacelles.

Incremental nacelle drag estimates were made for flow-through wind-tunnel models of each of the four configurations. The effect of the nacelles on the wing-body polar shape was small for all but the four-engine spread nozzle case, and the increment of nacelle drag improved the configuration drag rise in all four cases.

The TEA-230 Subsonic Flow Analysis program played an essential role as a design tool during the main contract and provided valuable insight concerning the flow fields and the nacelle contouring required for minimum drag. The TEA-230 method was applied to the nacelle designs of the main contract in the following ways:

- The inboard contours of the external surface of each nacelle were designed along streamlines calculated by the TEA-230 program. Ideally, the nacelle is then "invisible" to the wing flow inboard of the nacelle, and the wing isobar sweep and resulting shock sweep at cruise inboard of the nacelle will be similar to that before the nacelle was added. This was the primary design principle and was applied to the outboard nacelle of the four-engine configurations as well as to the inboard nacelles.

- TEA-230 streamlines approaching the wing were the basis for the orientation of the nacelle inlet to meet the oncoming flow. In a typical case, the inlet was drooped by 1° and toed in by 1°.

- Second-cycle modifications to the nacelle designs were made in some cases on the basis of the TEA-230 analysis of the first-cycle wing-body-nacelle configurations. This included both the external surface and the internal duct surface of the nacelles. The given wing-body geometry was not modified.

Figures 1 and 2 provide a simple review of the flow of a streamline past a swept wing. In figure 1, typical wing upper-surface pressure gradients are shown to deflect an approaching streamline differently from the lower surface pressure gradients. Figure 2 illustrates the effect on the flow field of adding an infinite vertical plate aligned with the free stream approaching an infinite swept wing. Before the plate is added, two undisturbed streamlines approach the wing and follow the paths indicated over the upper and lower wing surfaces. If the plate is then added midway between these two approaching streamlines, the wing span load distribution is perturbed as shown in the lower half of the figure. The portion of the plate over the wing upper surface is at an angle of attack to the flow of the undisturbed streamlines, and negative pressures develop on the left side of the plate, positive pressures on the right side. On the wing lower surface, the effect of the plate is not as pronounced, since its angle of attack to the undisturbed lower surface streamlines is much smaller. Therefore, the wing loading is increased to the left of the plate and decreased to the right. From consideration of the plate as one side of a fuselage or of a nacelle, it is apparent that failing to streamline-contour such a surface would result in undesirable changes in the chordwise and spanwise pressure distributions. The deterioration would include isobar and shock unsweeping and more adverse pressure levels, pressure gradients, and load distribution.

Figures 3 through 8 are reproductions from the main contract report and highlight some of the features of the main contract study, including those that are pertinent to the present study. Figure 3 shows one of the overwing nacelle designs in plan and side views, including section cuts along the nozzle. This nacelle has a D-shaped exit and is designed for a two-engine airplane. Note the streamline-contoured inboard side of the nacelle in the plan view and the cant and droop of the inlet. The nacelle outboard contour cannot follow streamlines because of the thickness of the nacelle and the volume requirements of the internal duct. Based on the TEA-230 wing-body-nacelle analysis of the initial nacelle design, modifications were made to the lines as indicated in figure 4. The upper surface isobar

pattern calculated by the TEA-230 program for the final four-engine, D-nozzle design is shown in figure 5.

Figures 6 and 7 illustrate the calculation of streamlines by the TEA-230 method during the main contract. After analyzing the wing-body alone in TEA-230, streamlines which originated around the perimeter of the desired nacelle exit (fig. 6) were calculated from this solution and were traced forward ahead of the wing. The inboard streamlines then served as the basis for the nacelle external surface design. In the case of a four-engine configuration, the design of the outboard nacelle accounted for the influence of the inboard nacelle. Based on a TEA-230 analysis of the wing, body, and inboard nacelle, streamlines were calculated at the desired location of the outboard nacelle. One such streamline is shown in side and plan views in figure 7 as a dashed line. For comparison purposes, the solid line is the streamline originating from the same point on the wing upper surface for the case of wing-body alone.

Figure 8 illustrates the nacelle drag increment estimates that were prepared for each nacelle configuration designed during the main contract. These estimates were made on the basis of Boeing wind tunnel experience with overwing nacelle configurations, together with empirical methods. The present study includes an additional estimated nacelle drag increment. This latter increment takes account of possible discrepancies in the nacelle lines resulting from any limitations of the TEA-230 method in determining the actual pressure distributions and streamlines on such configurations.

5.0 WIND-TUNNEL AERODYNAMIC RESULTS FOR SELECTED OVERWING NACELLE CONFIGURATION

5.1 WIND-TUNNEL MODEL CONFIGURATION SELECTED FOR THIS STUDY

The overwing nacelle configuration shown in figure 9 was tested in 1973 in the Boeing transonic wind tunnel as one of a large number of overwing nacelle configurations studied at Boeing. The model configuration can be identified by its part number W19 B7 N26 and was selected as the best candidate for the present contract study. Considerations that influenced selection of this model are given below:

- The wing characteristics are similar to those of the wing given in the design study of the main contract:

Wing characteristics	NASA wing used in main contract	Wing 19 used in present study
Quarter-chord sweep	31°	27°
Aspect ratio	7.50	7.80
Taper ratio (basic trapezoid)	0.30	0.30
Type of wing section	Aft-loaded, high Mach no.	Aft-loaded high Mach no.
Max t/c, outboard wing	9.3%	9.3%
Cruise Mach no.	Not known	0.825
Fuselage mount	High wing	Low wing
Spanwise location of nacelle, percent of wing semispan	29%	42%
Side body, percent of wing semispan	12.5%	11.5%

- Many of the same nacelle design principles were applied in the designs during the main contract (sec. 4.0) as were applied in the design of the N26 nacelle. In particular, the streamline contouring of the inboard side of the nacelle was a common design guideline. In fact, the experience gained during this Boeing program of overwing nacelle configuration development significantly influenced the overall design of the nacelles during the main contract. Two differences between the nacelle types are: (1) the N26 nacelle was not designed for upper surface blowing whereas the contract nacelles were, and (2) the N26 nacelle was designed for smaller engines (bypass ratio = 5) compared with the contract nacelles (bypass ratio = 10).

- The W19 B7 N26 geometry represents a successful high-speed overwing flow-through nacelle configuration. At $M_\infty = 0.7$ where the test-theory comparisons were made, the effects of shock waves and boundary-layer separation were minimal.

- The W_{19} wing was fabricated in the wind-tunnel model shop using a numerical control cutting machine. This fabrication method has an advantage for the purposes of a test-theory comparison of wing pressure distributions, since the same cubic-spline numerical wing loft leads directly to the wing panel representation in TEA-230 as well as to the cutting of the model wing for the wind tunnel test. In addition, the numerical control cutting process produces smooth, accurate surface contours superior to surfaces prepared on the basis of several two-dimensional templates.

- Wing W_{19} had an ample distribution of pressure taps, including stations just inboard and outboard of the nacelle (see fig. 9). The pressure definition capability permitted a detailed comparison with theoretical results from the TEA-230 program.

- The model nacelle N_{26} was defined for the wind-tunnel model shop in considerable detail. Defining nacelle cross sections were given at nine stations together with side and plan views. This definition made possible an accurate modeling of the internal and external nacelle surfaces in TEA-230.

5.2 EXPERIMENTAL WING Cp DISTRIBUTIONS AT M_∞ = 0.7, 0.8, AND 0.84

Figures 10 through 24 present wing pressure distributions measured in the wind tunnel at M_∞ = 0.7, 0.8, and 0.84 on the configuration described in the previous subsection (5.1). No theoretical data are included in these plots. The small wing planform on each figure indicates the semispan station at which the data was recorded and whether or not the nacelles were present. The first seven of these figures show data with the nacelle off, and the next eight figures show corresponding data with the nacelle on. Data at section G for wing-body alone were not successfully recorded because of an instrumentation problem.

An isolated instrumentation or data reduction error is apparent on the lower surface C_p distribution of section E, wing-body alone, at M_∞ = 0.7 (fig. 14). The C_p level over the entire chord is too positive, judging from comparisons with data at adjacent sections D and F and with nacelle-on data at section E.

For the wing-body configuration, the wing pressure distributions developed in a typical manner with increasing Mach number. The lower surface remained subsonic at all wing stations and the pressure level became more negative as M_∞ increased to 0.84, much as would be predicted by theoretical compressibility rules. The critical C_p levels at which the local Mach number reaches unity are indicated below:

M_∞	$C_p]_{M_L = 1}$
0.7	-0.78
0.8	-0.43
0.84	-0.32

Except for the leading-edge region on the inboard wing, the upper surface C_p's at M_∞ = 0.7 are completely subsonic. At M_∞ = 0.8, regions of supersonic or near-sonic flow occur across most of the span, but a distinct shock pattern is apparent only in the M_∞ = 0.84 data. At M_∞ = 0.84, a shock is present on the outboard part of the wing at 65 percent of chord, and

a more highly swept shock occurred across the inboard wing between 10 percent and 25 percent of chord.

With the addition of the nacelle, the wing C_p distributions adjacent to the nacelle become more negative on both the upper and lower surfaces. However, the beneficial effect of the streamline contouring on the inboard side of the nacelle is evident on the inboard wing. At $M_\infty = 0.7$, for example, the influence of the nacelle on the wing pressures at section D (figs. 13 and 20) is far greater than at section C (figs. 12 and 19). At section D just outboard of the nacelle, the effect of the nacelle is to create a"peaky"-type C_p distribution on the wing at lower Mach numbers. As the Mach number increased to 0.8 and then 0.84 (fig. 20), the shock location moved aft in the manner typical of "peaky" wing sections.

Some influence of the nacelle is also evident on the lower wing surface. This influence is expected since the nacelle keel-line fairs back under the wing (fig. 9). From section F outboard, the effect of the nacelle was negligible at $M_\infty = 0.7$ and 0.8 and small at $M_\infty = 0.84$.

6.0 COMPARISON WITH CORRESPONDING RESULTS FROM BOEING TEA-230 SUBSONIC FLOW METHOD

6.1 CONFIGURATION MODELING FOR TEA-230 POTENTIAL-FLOW ANALYSIS

The Boeing TEA-230 computer program is a generalized potential-flow method which uses panel distributions of source and vortex (or doublet) singularities to represent the surface geometry and lifting elements of arbitrary three-dimensional configurations. The solution consists of local pressure coefficients for all surface panels, flow conditions at specified points in the external flow field, and streamline tracing through desired points. Compressible subsonic flow problems are solved through application of the Gothert rule. The surface panel representation and lifting system panels can be plotted automatically in four views. References 2 and 3 describe this method and its implications. The details of the application of TEA-230 system to the overwing nacelle configurations developed during the main contract are presented in reference 1 and will not be repeated here.

Figure 25 illustrates the distribution of source panels used to represent the W19 B7 wing and fuselage surfaces (half-model only). Approximately 800 constant-strength panels simulated the wing and 200 panels simulated the body. About 200 more singularities (1040 individual panels) were distributed over the wing camber surface inside the wing to provide the proper circulation and lift. These vortex panels are shown in figure 26, including the trailing vorticity system aft of the wing. The total number of unknowns in the potential flow solution was therefore about 1200. This wing-body was analyzed at $M_\infty = 0.7$ and a range of 10 angles of attack. The design angle of attack for comparison with wind tunnel data was 2.3°.

The addition of the nacelle internal and external surfaces to the wing-body model required an additional 300 surface source panels and 100 vortex singularities distributed around the nacelle camber surface. Plan and side views of the source panels are displayed in figure 27 and the lifting system panels in figure 28. This 1600-singularity representation of the wing-body-nacelle is similar in detail to the configurations analyzed in TEA-230 during the nacelle designs of the main contract.

6.2 TEST-THEORY COMPARISON FOR WING-BODY AT $M_\infty = 0.7$

The wing-body configuration was analyzed in the TEA-230 program at $M_\infty = 0.7$ and streamwise wing C_p distributions were determined at sections A through H corresponding to the available wind tunnel C_p data. The test-theory comparisons at each wing station are displayed in figures 29 through 35. Note that the wind-tunnel data were determined at the same free-stream Mach number and angle of attack (including wind-tunnel corrections) as were the TEA-230 results. The lift coefficient for the wind-tunnel model was 0.35 and the Reynolds number per meter was 1.14×10^7 ($3.46 \times 10_6$ per ft). Note also that the C_p scale has been expanded compared to the pressure plots shown earlier (figs. 10 through 24), in order to magnify the details of the comparisons. The critical C_p level, at which the local Mach number is equal to 1.0, is indicated on each plot.

In this subsection and the next, the wind-tunnel and TEA-230 pressure data will be presented with some brief comments. A more comprehensive analysis of the comparisons, including suggested reasons for some of the differences between test and theory, will be presented in section 7.0.

As an overall evaluation of the pressure distribution comparisons shown in section 6.0, the results of the TEA-230 analysis show excellent agreement with the corresponding wind-tunnel data. The shapes of the wing upper and lower surface C_p distributions are predicted quite accurately by the program, and the C_p levels compare favorably on the inboard wing sections. On the outboard part of the wing, a small shift in C_p level is evident between the data. The increment in the C_p distributions due to the presence of the nacelle (subsection 6.3) was determined by the TEA-230 method with good accuracy, as compared with the wind-tunnel data. These favorable evaluations of the test-theory comparisons are made in light of existing comparisons published at Boeing and in the general literature for high-speed airplane configurations of comparable complexity.

Figures 29 and 30 display the agreement at sections A and B. On the leading-edge region of the upper surface, the local Mach number becomes supersonic and the TEA-230 potential-flow theory is not applicable. Differences in the predicted aft-loading and that measured in the wind tunnel as shown here are attributed to the decambering effect of the wing boundary layer. Again, this discrepancy is expected since the TEA-230 method does not include viscous effects, which will be discussed in detail in section 7.1.

At section C (fig. 31), the C_p comparison revealed an anomaly in the experimental data on the upper surface of the wing. The excessively negative C_p level forward of 25 percent chord led to the discovery of a surface irregularity in that region on the wind-tunnel model wing. A second problem was discovered with the wind-tunnel model wing geometry. The measured maximum section thickness at several stations across the wing proved to be slightly larger than it was supposed to be. Although these increments in thickness were small, they will be shown in section 7.0 to contribute to the differences in C_p level exhibited in these comparisons, more predominantly on the outboard wing sections (figs. 32 through 35).

Figure 36 shows the isobar pattern determined analytically for the upper surface of the wing.

6.3 TEST-THEORY COMPARISON FOR WING-BODY-NACELLE AT $M_\infty = 0.7$

Pressure comparisons at the same wing stations as for the wing-body configuration are presented in figures 37 through 45 for the case with nacelles present. The wing-body data presented in the previous section are included again here as a reference. At wing stations A and B, the effect of adding the nacelle is determined quite successfully by the TEA-230 method. At section C, the comparison is complicated by the previously mentioned surface irregularity on the wind tunnel model. However, the increment in C_p due to addition of the nacelle is still predicted with good accuracy, as illustrated in figure 40. Outboard of the nacelle, the test-theory comparisons are again favorable, when the TEA-230 theoretical

limitations (no supersonic or viscous capabilities) and the wind-tunnel model thickness discrepancies are taken into account. Again, these factors will be discussed in detail in a later section.

Figure 46 shows the effect of the presence of the nacelle on the wing upper surface isobar pattern determined analytically. The dashed lines indicate the wing-body isobars for reference. Isobars on the top of the nacelle are also shown. These results are similar to the isobar patterns determined for the nacelle designs of the main contract. In the present case, however, the N_{26} nacelle design shows more extensive isobar unsweeping inboard of the nacelle than was characteristic of the main contract designs.

The test-theory comparison of configuration lift curves for wing-body and wing-body-nacelle is shown in figure 47. As is typical of potential-flow versus real-flow lift comparisons, the wind-tunnel data exhibit a lower lift level. Such differences are normally attributed to the effective decambering of the wing by the boundary layer. For the wing-body-nacelle case, the analytically determined lift coefficient at the design angle of attack is 8 percent higher than the corresponding value from the wind tunnel.

Figure 48 compares theoretical and experimental wing span load and sectional lift distributions, determined by integrating the pressure distributions presented earlier. For the sectional C_{ℓ} data, the test-theory comparison is good on the inboard wing sections where the C_p comparison was also excellent. On the outboard part of the wing, the lift levels from experiment were substantially lower than indicated by the theory. Again, this lack of agreement is believed to be due to the effective decambering of the boundary layer on the aft-loaded outboard wing sections. The data for each wing span-load distribution shown have been normalized such that the area under each curve is equal to unity. Therefore, the lower experimental levels on the outboard wing sections lead to experimental loading levels on the inboard part of the wing which are higher than the theoretical levels.

7.0 ANALYSIS OF TEST-THEORY COMPARISON

7.1 LIMITATIONS OF THE TEA-230 METHOD

In this section, some aspects of the real flow over the wind-tunnel model are discussed which are not accounted for in the theory inherent to the TEA-230 method. These theoretical limitations are then related tentatively to some of the discrepancies between theoretical and experimental C_p distributions evident in subsections 6.2 and 6.3. The intent is to propose relationships between the observed differences of test data and theory compared with limitations of the TEA-230 theoretical model.

The TEA-230 computer program is based on a three-dimensional potential-flow solution to the Navier-Stokes equations. The basic incompressible, inviscid solution is then modified to account for subsonic compressibility effects by means of the Gothert rule. Since the theory is not applicable to transonic flow, the test-theory C_p differences over regions of the wing where the local Mach number exceeds unity are not unexpected. (See, for example, figs. 30, 38 and 41.)

Since the potential-flow theory takes no account of boundary-layer growth along the configuration surfaces in the wind tunnel, test-theory differences in C_p level are anticipated on both the upper and lower wing surfaces. For the wind-tunnel data presented in this report, the wing boundary layer was tripped at 10 percent of chord on both the upper and lower surfaces. Therefore, boundary layer thickening along the wing chord was significant.

The general effects of the boundary layer on a two-dimensional potential-flow solution for an airfoil are well known. Figure 49 illustrates these effects for a typical advanced, rear-loaded airfoil. The dashed line indicates the pure potential-flow C_p distribution on the airfoil and the solid line shows the potential-flow distribution calculated with the displacement effect of the boundary layer included. The symbols are for corresponding two-dimensional wind tunnel data. As indicated earlier, the effect of the boundary layer can be described as an effective decambering of the airfoil, with the lift contributions reduced along both the upper and lower surfaces. Three-dimensional boundary-layer growth on a wind-tunnel model wing includes spanwise boundary-layer flow and is not as clearly understood. However, the viscous effects displayed in the two-dimensional example of figure 49 can be related to the three-dimensional streamwise C_p comparisons of subsections 6.2 and 6.3. The compressed C_p scale in figure 49 should be noted when comparing increments in C_p level with the corresponding wing-body data. In figure 34, for example, boundary-layer effects on the outboard part of the wing could account for much of the test-theory C_p increment, especially along the lower surface. On the upper surface at this wing station the experimental C_p level over the midchord region is more negative than the theoretical level. Since viscous effects should tend to make the wind-tunnel data more positive over this region, other factors are believed to be contributing to this discrepancy. This characteristic of the test-theory comparison over the midchord region of the wing upper surface is present over the entire span of the wing (figs. 29 through 35).

A less significant limitation of the TEA-230 method involves the Gothert rule compressibility correction used in the program. Compressibility rules of the Gothert type are known to be incorrect in predicting the effect of free-stream Mach number on the leading edge pressure distribution on the upper surface of a wing. Figure 15 is typical of the effect observed in the wind tunnel. As M_∞ increased from 0.7 to 0.8 to 0.84, the velocity on the upper surface leading edge decreased, and the $C_{p_{min}}$ peak moved slightly aft. The same qualitative behavior is observed at lower Mach numbers and on two-dimensional as well as three-dimensional wing models. The Gothert rule is effective in determining subsonic Mach number effects over most of the wing by appropriately scaling the incompressible pressure values to a more negative level. However, such a scaling on the leading-edge upper surface C_p values is opposite to the observed real-flow behavior. The Gothert rule correction for $M_\infty = 0.7$ in the theoretical data presented in subsections 6.2 and 6.3 is believed to be responsible for the test-theory discrepancies on the leading edge of the outboard part of the wing (see figs. 32 through 35).

The modeling of the wing-body-nacelle surfaces using a finite number of flat panels in the TEA-230 method also represents some approximation to the real geometry. However, the panel density shown in figure 27, for example, is believed to be sufficient so that improvements in solution accuracy on the wing would not be anticipated if more panels were used. The analytical method uses constant-strength source panels to represent surfaces. Experience with the program has led to the criterion that paneling must be selected to minimize the differences in source strength between adjacent panels. This criterion was applied to the geometry modeling of the present study. Therefore, corresponding numerical errors in computed tangential surface velocity components are believed to be negligible.

Since streamlines determined by the TEA-230 program were the basis for the nacelle designs of the main contract, a discussion of the expected accuracy of the streamline calculation method is pertinent. The streamline calculation program determines a streamline upstream and/or downstream of a given initial point in the flow field based on the singularity strengths determined in the potential-flow solution. Small segments along the streamline are calculated using a Kutta-Merson numerical scheme, based on local velocity vectors determined at adjacent points in the flow field. The accuracy of the integration procedure is controlled by specifying maximum step sizes and a "relative error bound" parameter. Although no experimental data are available with which theoretically determined streamlines can be compared, indirect verification of the streamline method exists at Boeing in the form of successfully designed fairings for wind tunnel models. For example, wing-body fairings have been designed to alleviate flow problems by aligning the fairing with calculated streamlines. (See oil flow photographs in reference 2.) Based on the numerical sophistication of the TEA-230 streamline calculation procedure and the favorable wind-tunnel experiences with theoretically streamline-contoured surface designs, it is believed that errors in the analytical determination of streamlines are not significant.

7.2 WIND-TUNNEL MODEL SURFACE IRREGULARITIES

In subsection 6.2, it was indicated that anomalies in the experimental pressure data on the model wing led to the discovery of small deviations between the actual measured geometry and the desired geometry as defined by a numerical wing loft. The same numerical wing loft

was the basis for the theoretical wing model and for the wind-tunnel model wing. The effect of these deviations on the test-theory pressure comparisons will be discussed in this section.

The existing wind-tunnel model wing was measured to determine possible deviations in thickness or section shape from the loft definition. The maximum section thickness was measured by micrometer at each of the streamwise pressure-tap stations indicated in figure 9. Several independent repeat measurements were made in order to establish a mean error due to the measurement procedure. The results are shown in figure 50, with a greatly expanded scale of section thickness-to-chord ratio. Figure 51 illustrates the largest of the deviations in wing geometry that were determined by fabricating new chordwise wing section templates on the model. The chord lengths and surface thickness deviations shown in figure 51 are actual model scale, but the section shapes have been distorted to protect the proprietary nature of the geometry.

The magnitude of the surface deviations shown in figures 50 and 51 are considerably greater than expected, inasmuch as the wing was fabricated by a numerical control cutting machine. However, the surface tolerance requirements for wings fabricated for configuration development testing of this type are less stringent than usual. The "bump" on the nose of section C was a local irregularity and probably was overlooked following a modification to the original wing contour on the upper surface of the inboard part of the wing.

In order to assess the impact of these surface deviations on the test-theory comparisons presented in section 6.0, a simplified version of the thicker measured wing geometry was modeled for TEA-230 analysis. Based on the measured maximum thickness values shown in figure 50, the chordwise wing sections in the original numerical wing loft were scaled in thickness from the level of the dashed line to that of the solid line in figure 50. This scaling was performed while retaining the same camberline at each wing section. No attempt was made to determine whether the excess wing thickness was predominantly on the upper or lower surface, although the template at section H in figure 51 indicated a fuller lower surface. For the purposes of this additional TEA-230 analysis the increased thickness was distributed evenly on the upper and lower surfaces. The local irregularity on the nose of section C was not included in the new theoretical wing model.

The results of the TEA-230 wing-body analysis for the thickened wing are shown at selected stations in figures 52, 53, and 54 as a dashed line for the same conditions as in the original wing-body analysis. The analytical pressure data for the thicker wing shows a slightly more favorable comparison with the experimental pressure data, especially at the most outboard section H (fig. 54). However, the increment remaining between the dashed lines and the symbols over the midchord region of the wing upper surface is still not the result expected from the absence of viscous effects in the theoretical model.

Although the bump on the forward upper surface of the wing model at section C (fig. 51) was not modeled analytically to determine the corresponding deviation in pressure, wind-tunnel testing experience indicates that the magnitude of the geometry increment is sufficient to produce the experimental pressure discontinuity shown in figures 31 and 39.

7.3 WIND-TUNNEL FLOW ANGULARITY

A small spanwise variation of upflow is believed to exist across the test section of the wind tunnel in which the present model was tested. Although the overall upflow level at the model is accounted for in wind tunnel data corrections, this spanwise upflow variation is not accounted for. It is very small and is a function of the particular model mounting system. Although the upflow level corresponds to only a few tenths of a degree of angle of attack, a significant spanwise variation might be important to a detailed wing pressure data study of the present type. Such a variation would represent an effective increment in wing twist for the wind-tunnel model, not present in the theoretical model.

7.4 IMPACT OF TEST-THEORY COMPARISON ON NACELLE DESIGNS OF MAIN CONTRACT

One of the purposes of the present contract study was to assess the impact of any significant discrepancies in the test-theory pressure comparisons on the nacelle lines and nacelle drag estimates determined during the main contract. Such evaluations of theoretical design procedures are usually made by direct wind tunnel tests. However, these possible effects will have to be inferred because the nacelle design of the main contract was not tested experimentally. In this section, estimates will be made of the expected deviation in the streamlines along which the nacelle contours were designed, that may be attributed to test-theory discrepancies in streamwise pressure distribution of the type shown in section 6.0. In addition, the effect of these estimated deviations in the nacelle lines on the drag increment associated with the nacelles (see fig. 8) will be estimated in an order-of-magnitude sense.

A theoretical potential-flow study was made of the effect of two different chordwise pressure distributions on the deflection of streamlines passing over an infinite yawed wing. The two different wing section shapes and their corresponding potential flow pressure distributions on a 30° swept wing are shown in figure 55. Note that the section shapes differ somewhat in camber and angle of attack, but differ predominantly in thickness. The types of differences in the chordwise pressure distributions shown in figure 55 for the two wings are not unlike the test-theory comparisons observed, for example, in figure 52. The magnitude of the C_p differences in figure 55, however, is more than twice as large as that of the test-theory discrepancies in figure 52 (note C_p scale difference). For each of the two wing shapes in figure 55, the same cylindrical streamtube approaching the 30° swept wing was traced as it approached the wing leading edge and was deflected above and below the wing. Based on the respective potential-flow solutions, these streamtubes were defined by 20 streamlines spaced evenly around the perimeter of the initial circular tube. The rear view of the deflected streamtubes is shown in the top half of figure 56, at a streamwise wing station of 40 percent of chord. The increment in vertical displacement of the two streamtubes due to the differing wing thicknesses is removed in the bottom half of the figure by collapsing both streamtubes onto the wing 1 surface. In this way, the difference in the spanwise deflection and shape distortion of the two streamtubes can be more readily compared. It is observed that the two streamtubes differ significantly only on the inboard side of the upper half of the tube. The spanwise increment at that point is approximately 5 percent of the streamtube width or, in the nacelle analogy, about 5 percent of the width of a D-nozzle nacelle exit.

In terms of the nacelle designs developed during the main contract, the conclusion one reaches from the above study is as follows: test-theory discrepancies in wing pressures typified by figure 52 would be expected to result in test-theory discrepancies in streamtube displacement over a swept wing which are considerably less than shown in the lower half of figure 56. Since such streamtubes were the basis for the design of the inboard side of the nacelle contours during the main contract, no significant nacelle boattail angle to the streamlines would be expected.

For the sake of comparison, figure 57 shows the deflection of the same initial streamtube as a function of wing sweep. In this case, the same wing section (wing 1 in fig. 55) was used on an infinite yawed wing having 30° sweep and one having 40° sweep. The difference in the deflection of the streamtube at 40 percent of wing chord due to the two different wing sweeps is seen to be substantially greater than that due to the two differing chordwise pressure distributions.

The impact of such small deviations in streamtube deflection on the nacelle drag increment in the wind tunnel remains to be assessed. That is, if the theoretical streamtube, along which the nacelle inboard contours were designed, differs from the corresponding real-flow streamtube over the wind tunnel wing model, what nacelle drag increment would be estimated due to this misalignment? Two items of Boeing wind-tunnel data will be presented which are pertinent to this question.

In figure 58 the effects of streamline-contouring an overwing nacelle are shown as they relate to configuration drag rise curves determined in wind-tunnel tests. The drag levels are compared for the same wing-body with a straight-sided nacelle and with a streamline-contoured nacelle. The data of interest are the increments in drag between a contoured nacelle and a nacelle with no contouring. Near the drag rise Mach number the contoured nacelle exhibits less drag by about $\Delta C_D = 0.0010$, which can be expressed as about 4 percent of total airplane drag.

The second pertinent item of wind-tunnel data resulted from a study of the effect of reduced outboard boattail angle on the nacelle drag and is summarized in figure 59. An existing overwing nacelle configuration was modified by reducing the boattail angle by 4° on the outboard side of the nacelle, as indicated in figure 59. The drag increment (actually an increase in drag) associated with this modification is shown in the figure at various Mach numbers and two lift levels. Between 0.7 and 0.85 Mach number, this drag increment averages about $\Delta C_D = 0.00035$, or about 1 percent of total airplane drag.

Both of the wind-tunnel studies described above give an indication of the order-of-magnitude of the drag increment that can be expected in a wind-tunnel test due to recontouring the overwing nacelle lines. Based on these data, no significant nacelle drag increment is expected due to the deviations estimated above in the design of nacelle lines along TEA-230 streamlines.

8.0 CONCLUDING REMARKS

The favorable comparison between experimental and analytical wing pressures in this report adds a measure of confidence to the nacelle design procedure used during the main contract, NAS1-12214. The present study not only confirms the competence of the TEA-230 Subsonic Flow Analysis method in such design/analysis roles, but includes wind tunnel data which substantiate some of the design principles applied during the main contract. The test-theory comparison points out the ability of the TEA-230 program to reveal anomalies in wind tunnel test results, due in this case to model surface irregularities.

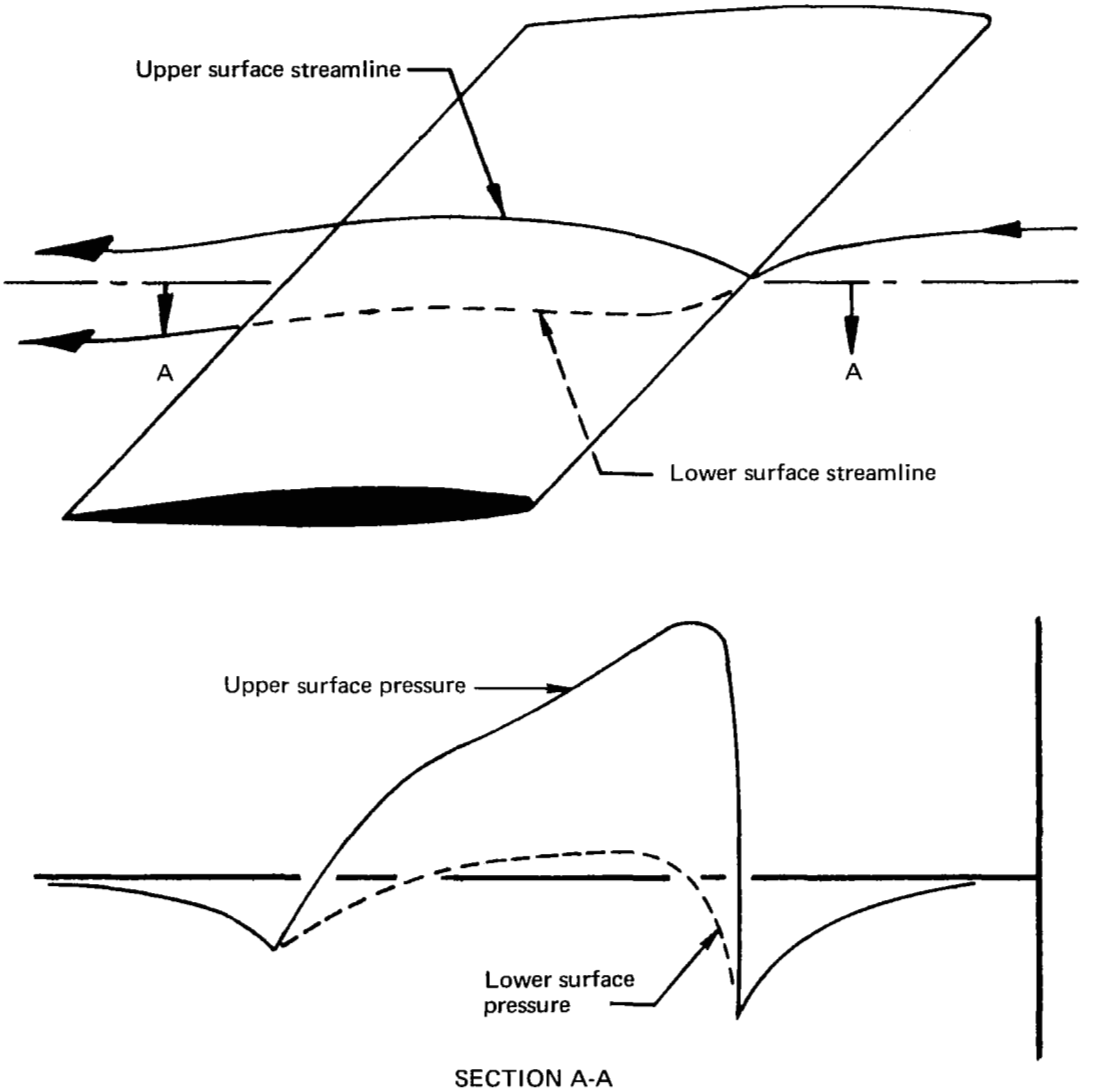

FIGURE 1.—TYPICAL FIELD PRESSURES AND STREAMLINE ON A SWEPT WING

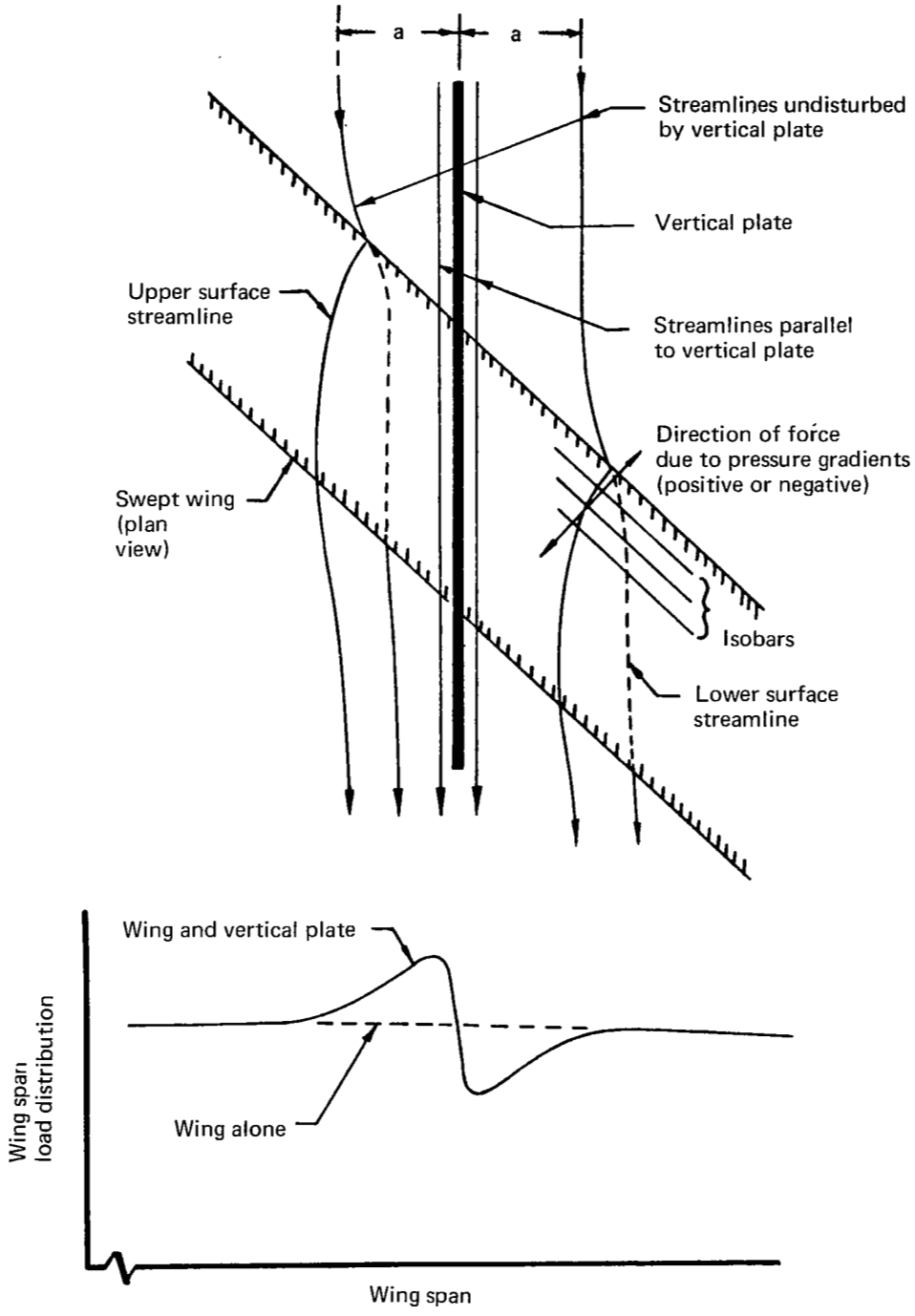

FIGURE 2.–EFFECT OF A VERTICAL PLATE ON THE FLOW FIELD OF A SWEPT WING

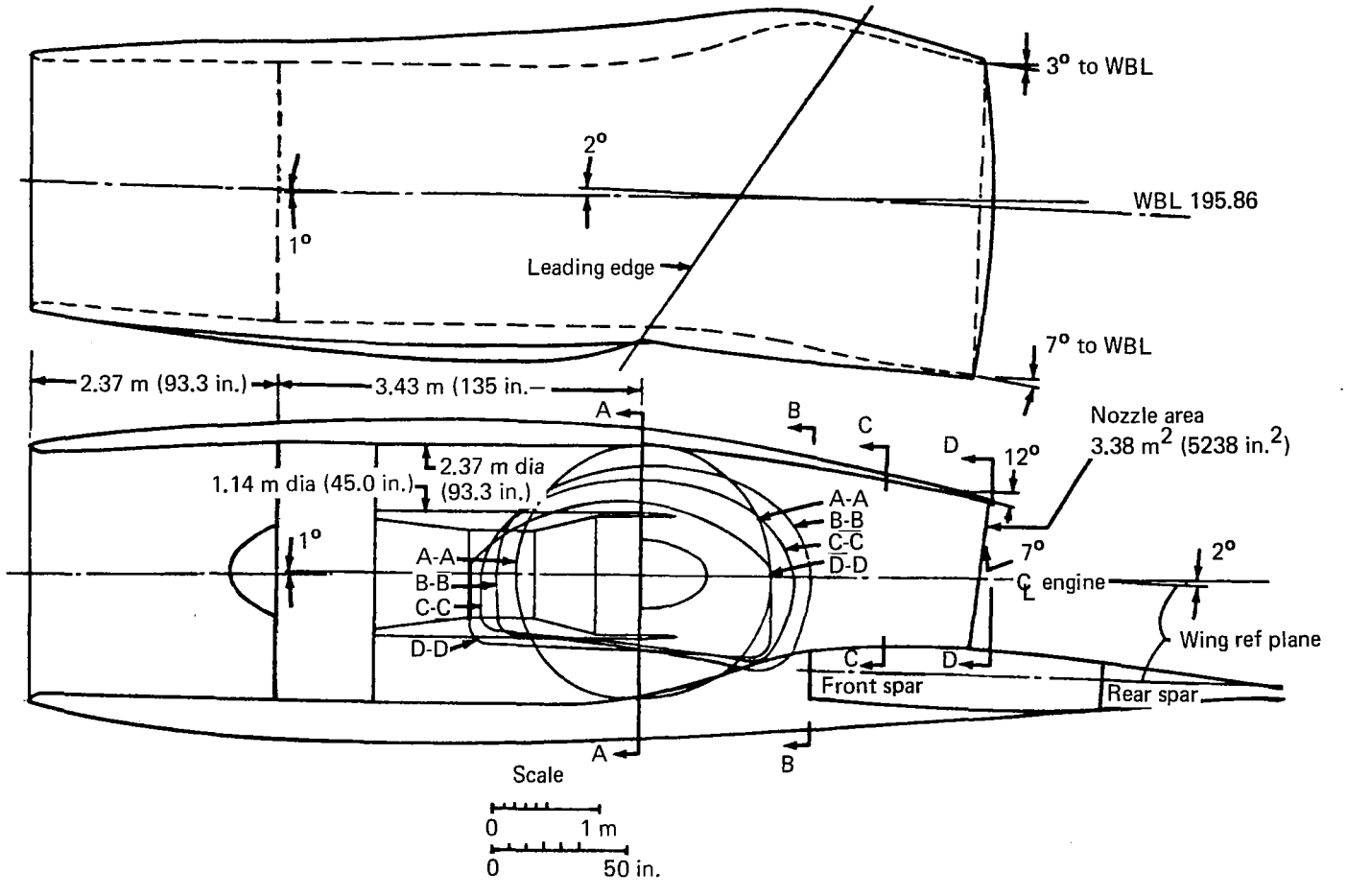

FIGURE 3.–D-NOZZLE NACELLE DESIGNED FOR TWO-ENGINE AIRPLANE DURING MAIN CONTRACT

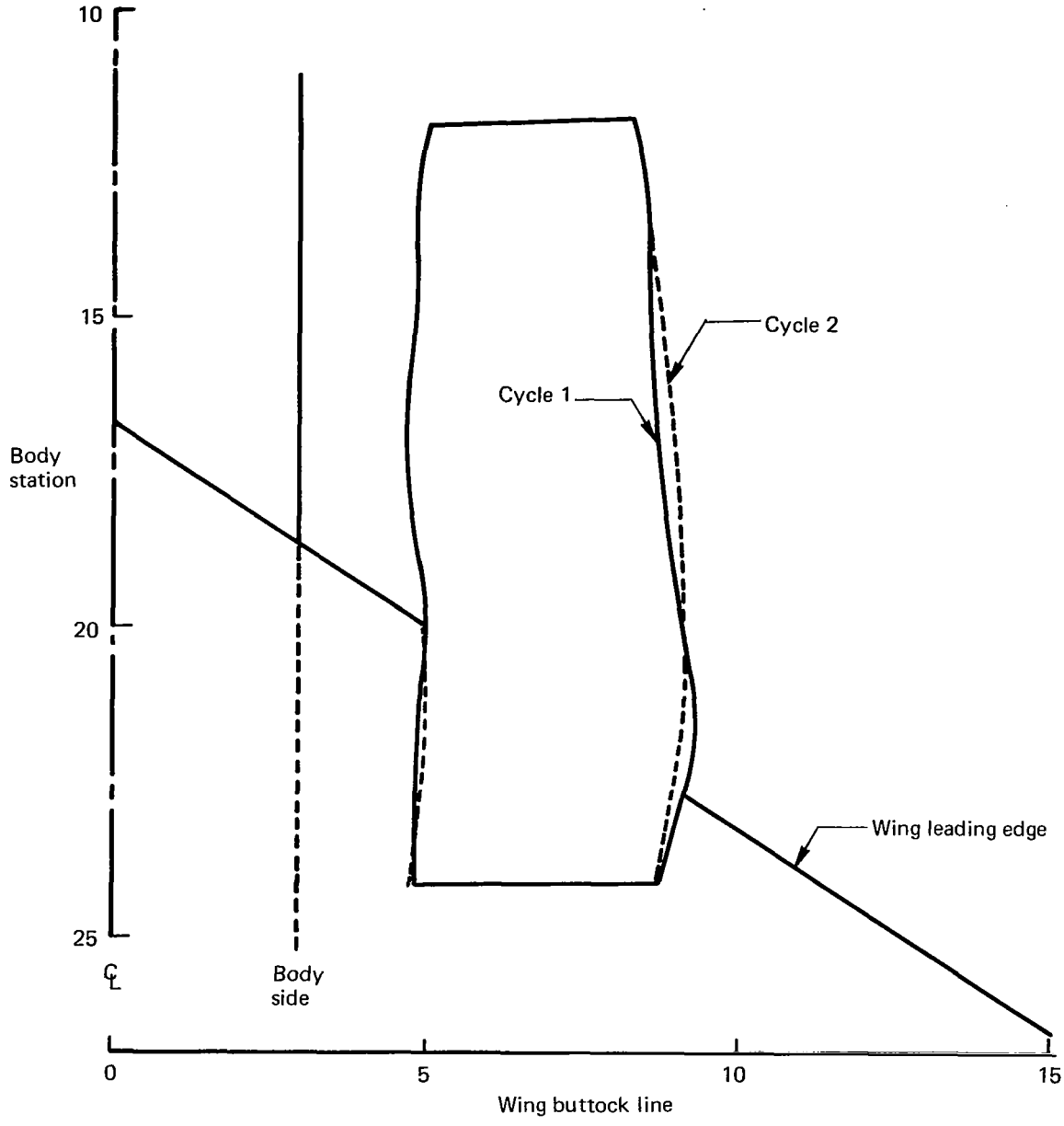

FIGURE 4.—TYPICAL MODIFICATIONS TO NACELLE LINES BASED ON TEA-230 ANALYSIS OF CYCLE 1 GEOMETRY (MAIN CONTRACT)

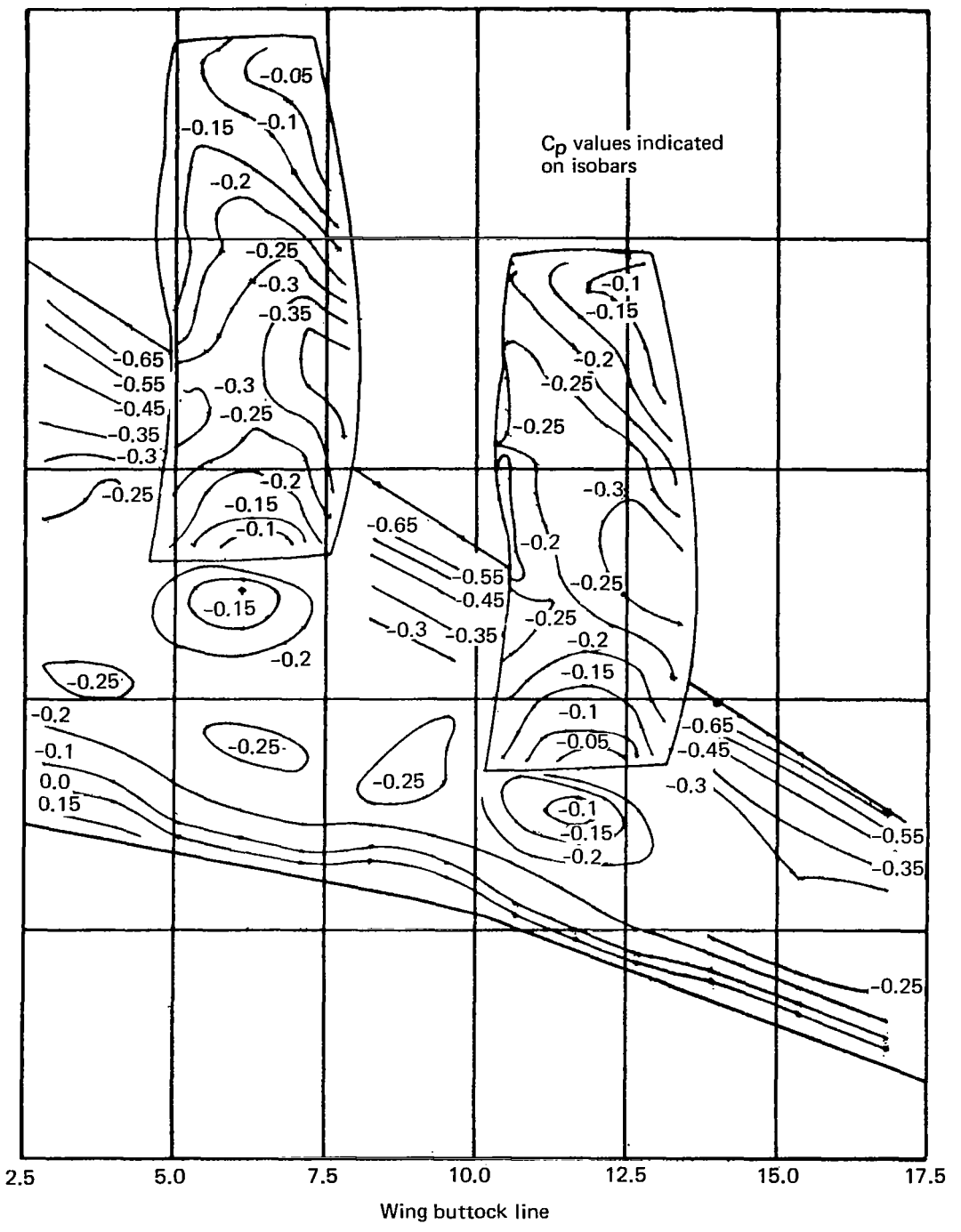

FIGURE 5.—UPPER-SURFACE ISOBARS DETERMINED BY TEA-230 DURING MAIN CONTRACT, FOUR-ENGINE D-NOZZLE CASE

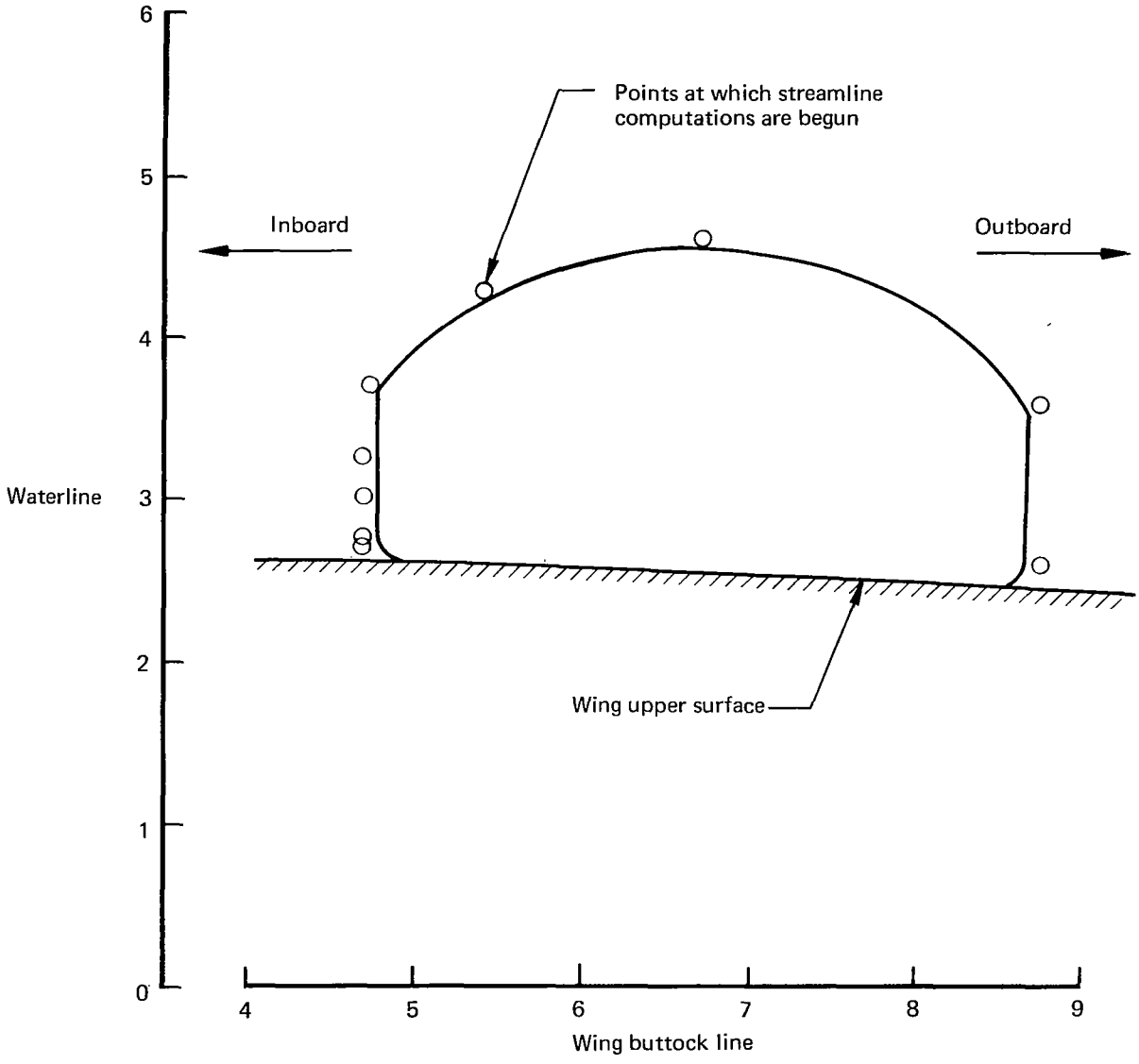

FIGURE 6.—STARTING POINTS AROUND NACELLE EXIT PLANE FOR CALCULATION OF NINE STREAMLINES IN POTENTIAL FLOW ANALYSIS, TWO-ENGINE D-NOZZLE CASE (MAIN CONTRACT)

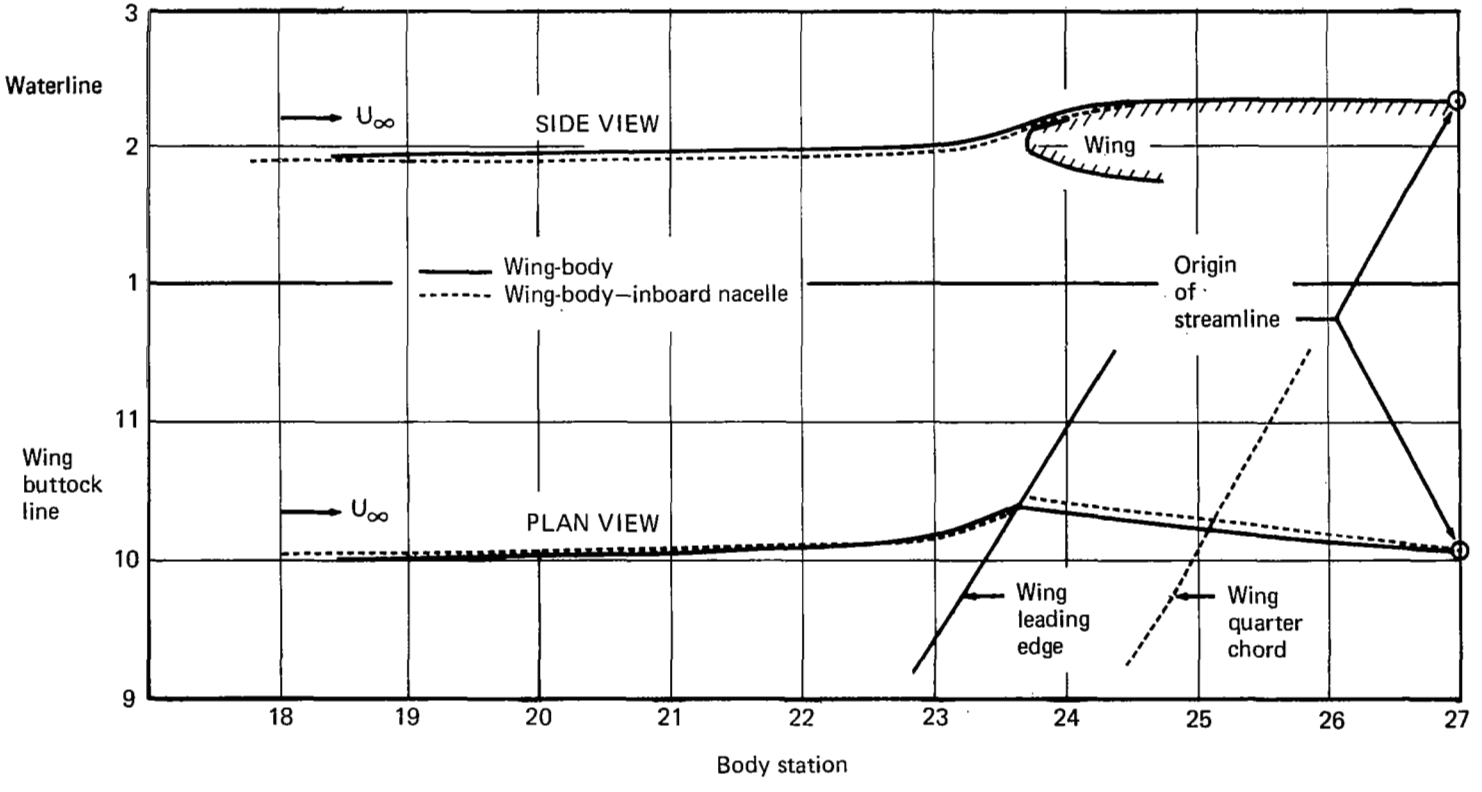

FIGURE 7.—EFFECT OF INBOARD NACELLE ON STREAMLINE PASSING OVER WING WHERE OUTBOARD NACELLE WILL BE LOCATED, FOUR-ENGINE D-NOZZLE CASE (MAIN CONTRACT)

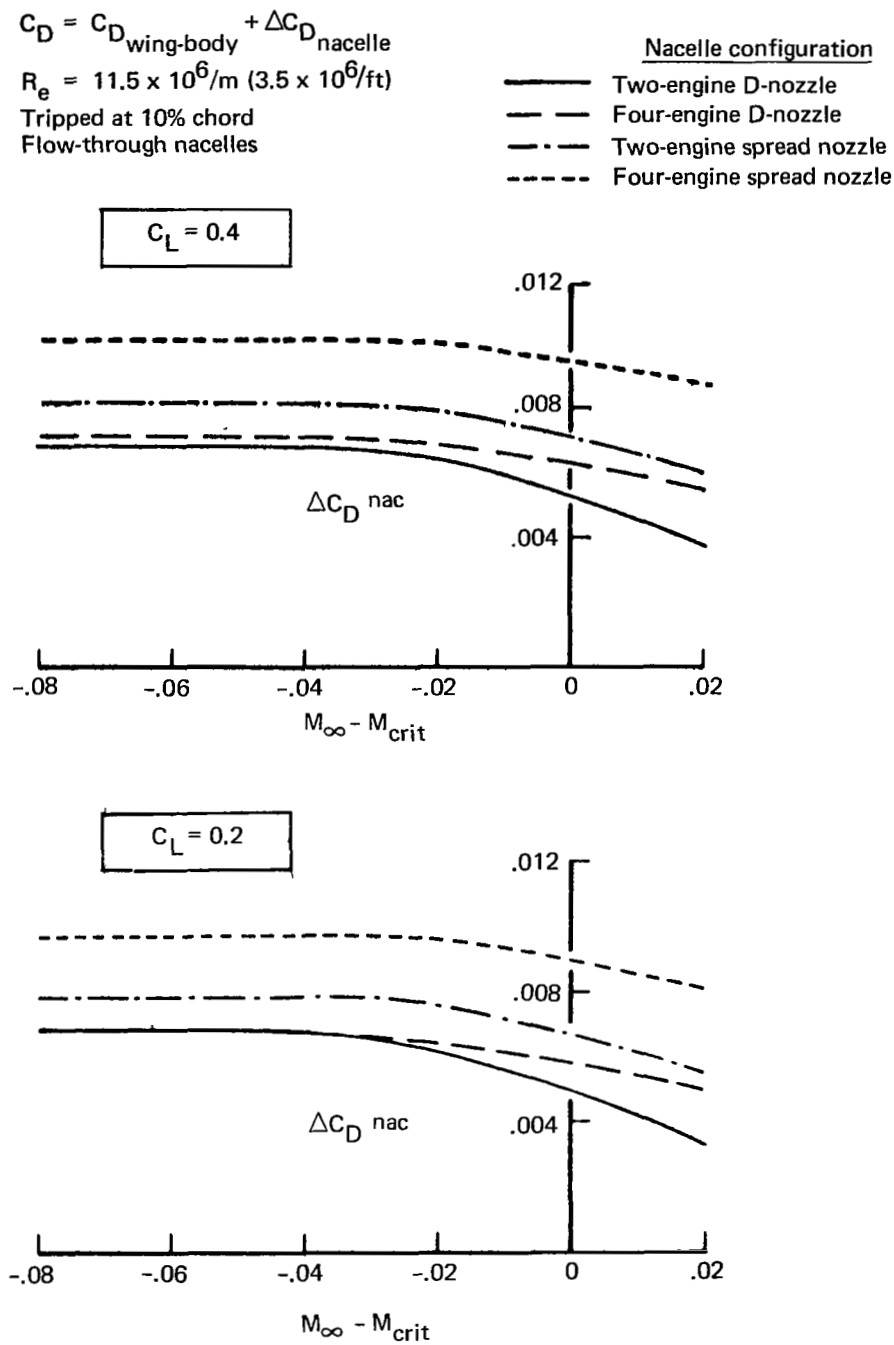

FIGURE 8.—ESTIMATED NACELLE DRAG INCREMENTS FOR MAIN CONTRACT

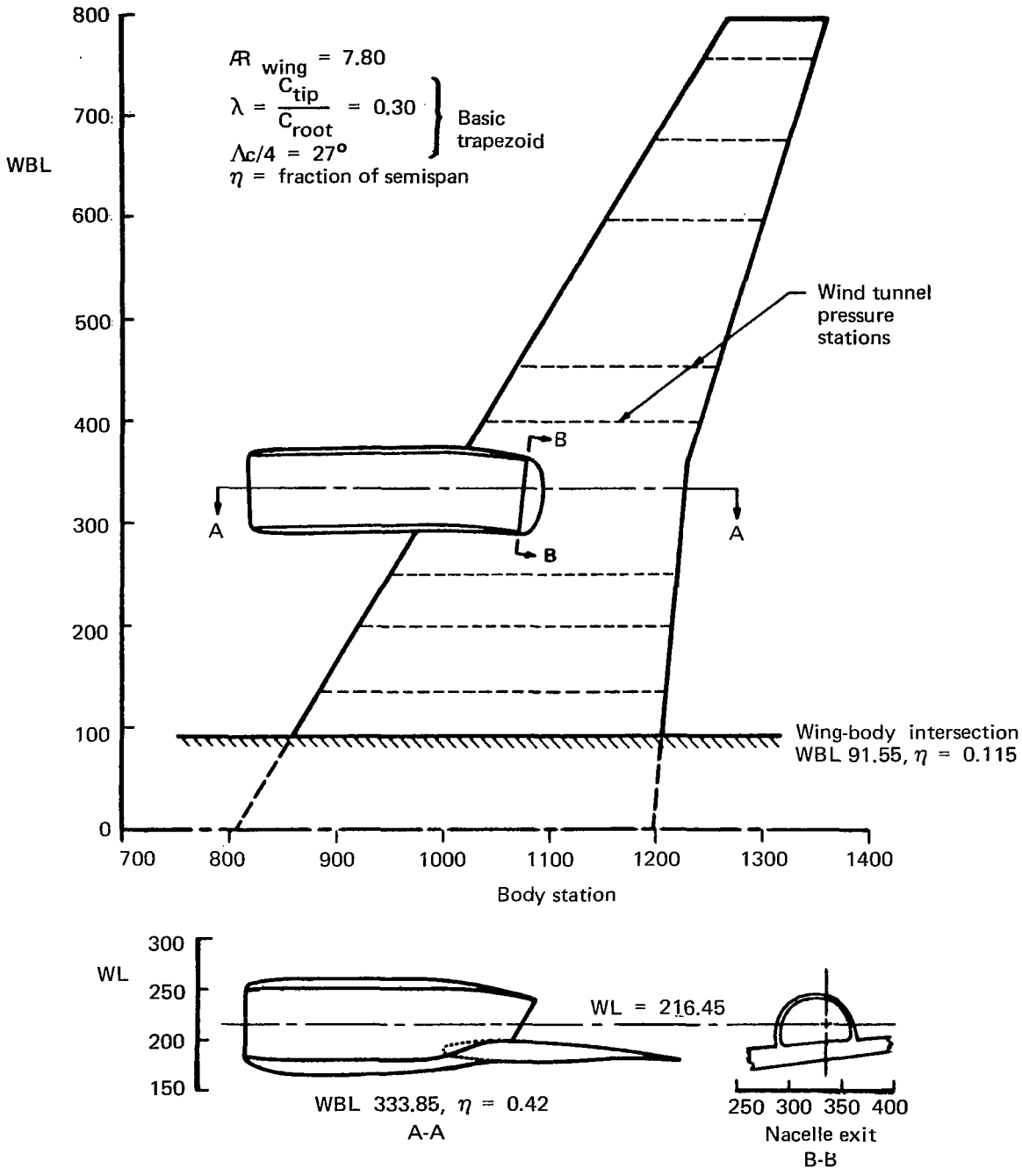

FIGURE 9.—CONFIGURATION GEOMETRY

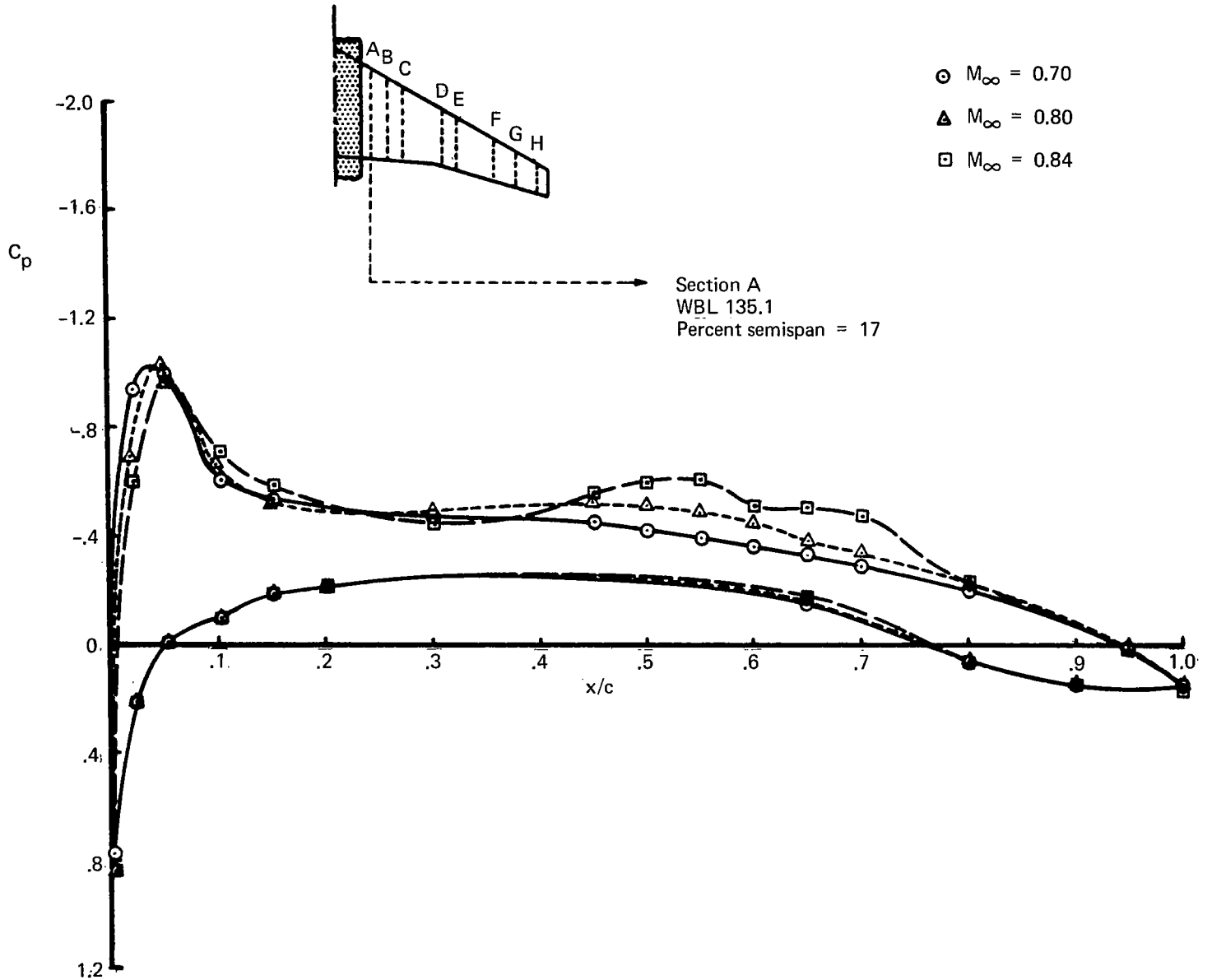

FIGURE 10.–EFFECT OF MACH NUMBER ON WING C_p DISTRIBUTION–WING-BODY ALONE, WIND TUNNEL DATA, α = 2.3°

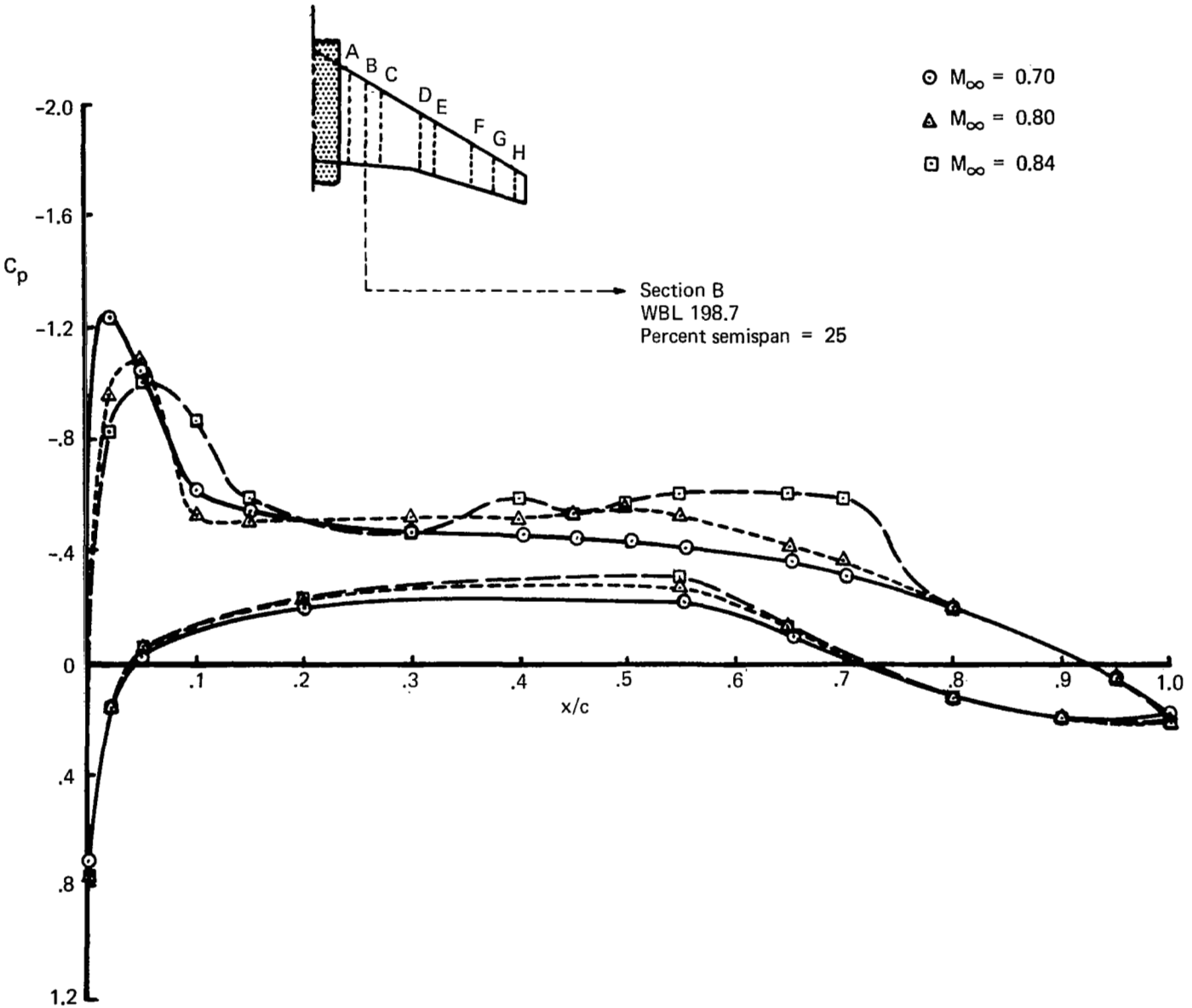

FIGURE 11.–EFFECT OF MACH NUMBER ON WING C_p DISTRIBUTION–WING-BODY ALONE, WIND TUNNEL DATA, $\alpha = 2.3°$

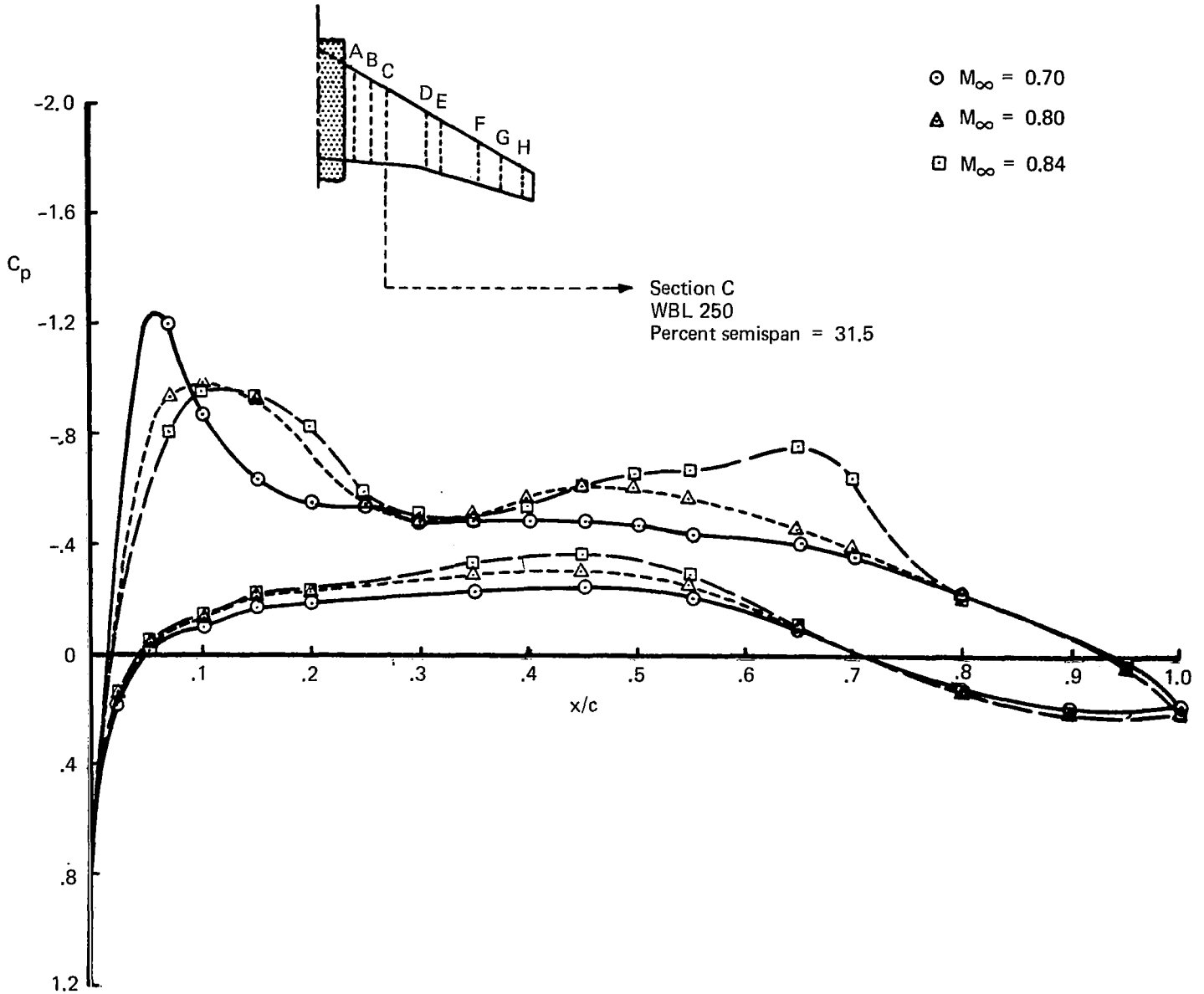

FIGURE 12.–EFFECT OF MACH NUMBER ON WING C_p DISTRIBUTION–WING-BODY ALONE, WIND TUNNEL DATA, $\alpha = 2.3°$

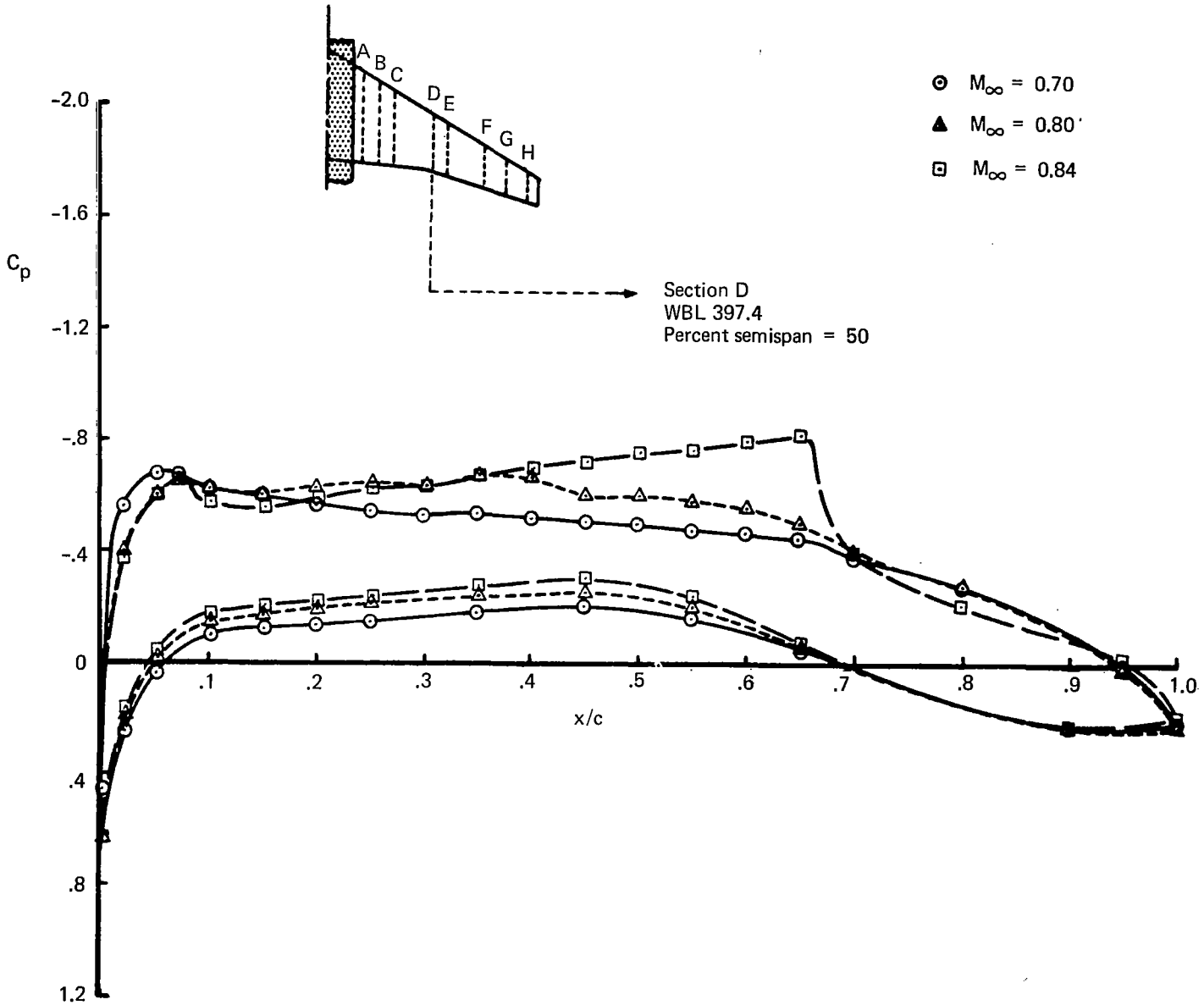

FIGURE 13.—EFFECT OF MACH NUMBER ON WING C_p DISTRIBUTION—WING-BODY ALONE, WIND TUNNEL DATA, $\alpha = 2.3°$

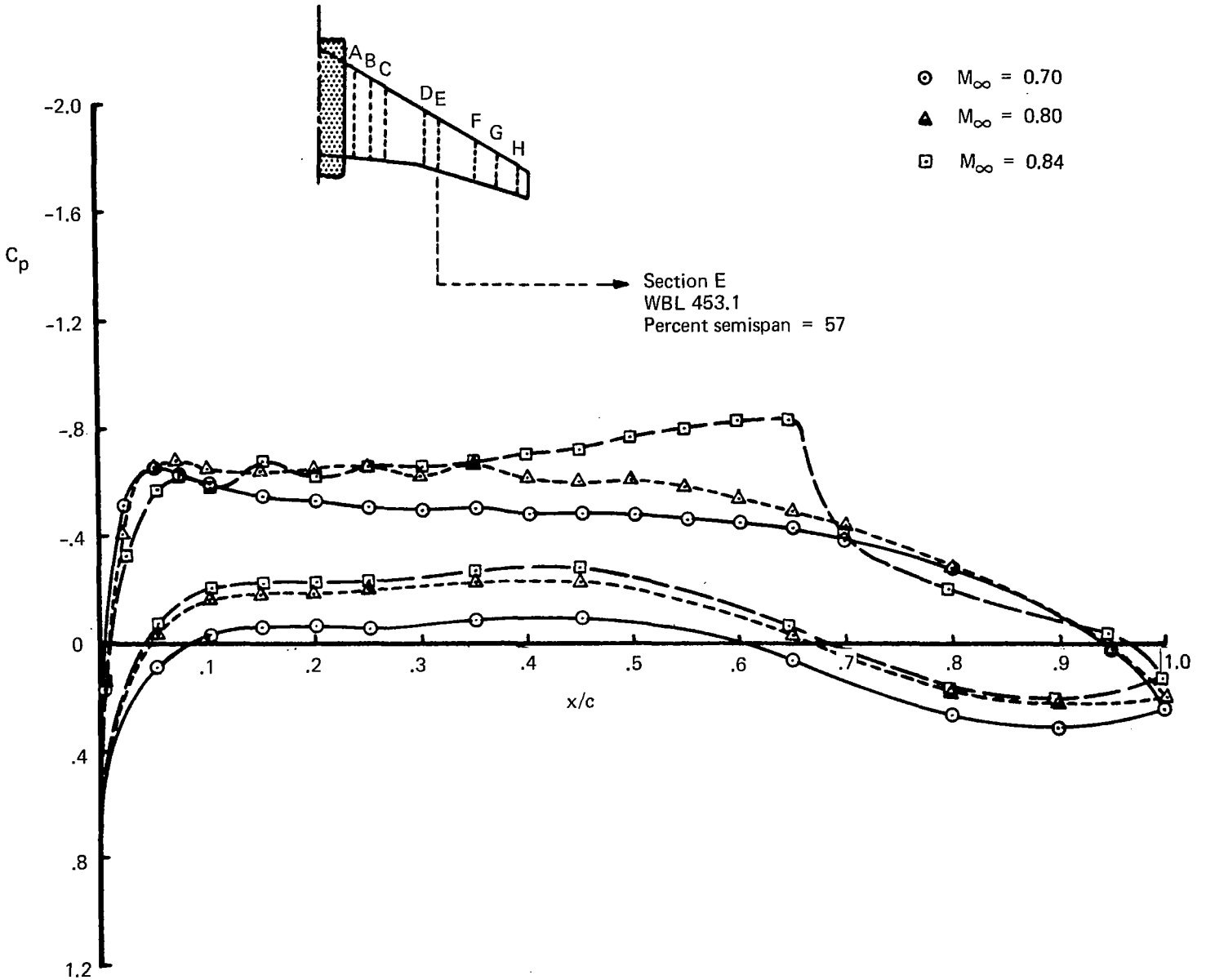

FIGURE 14.–EFFECT OF MACH NUMBER ON WING C_p DISTRIBUTION–WING-BODY ALONE, WIND TUNNEL DATA, $\alpha = 2.3°$

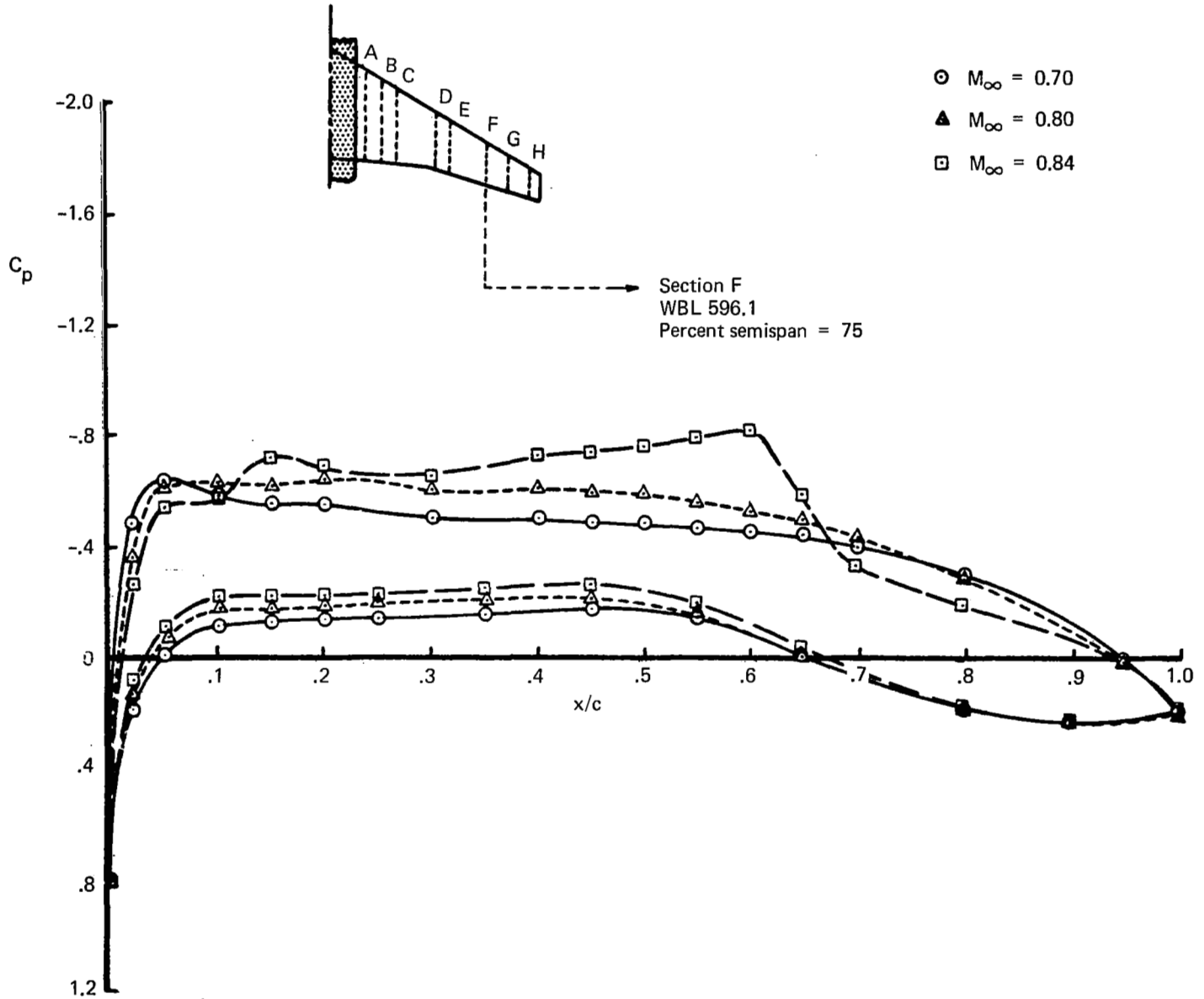

FIGURE 15.–EFFECT OF MACH NUMBER ON WING C_p DISTRIBUTION–WING-BODY ALONE, WIND TUNNEL DATA, $\alpha = 2.3°$

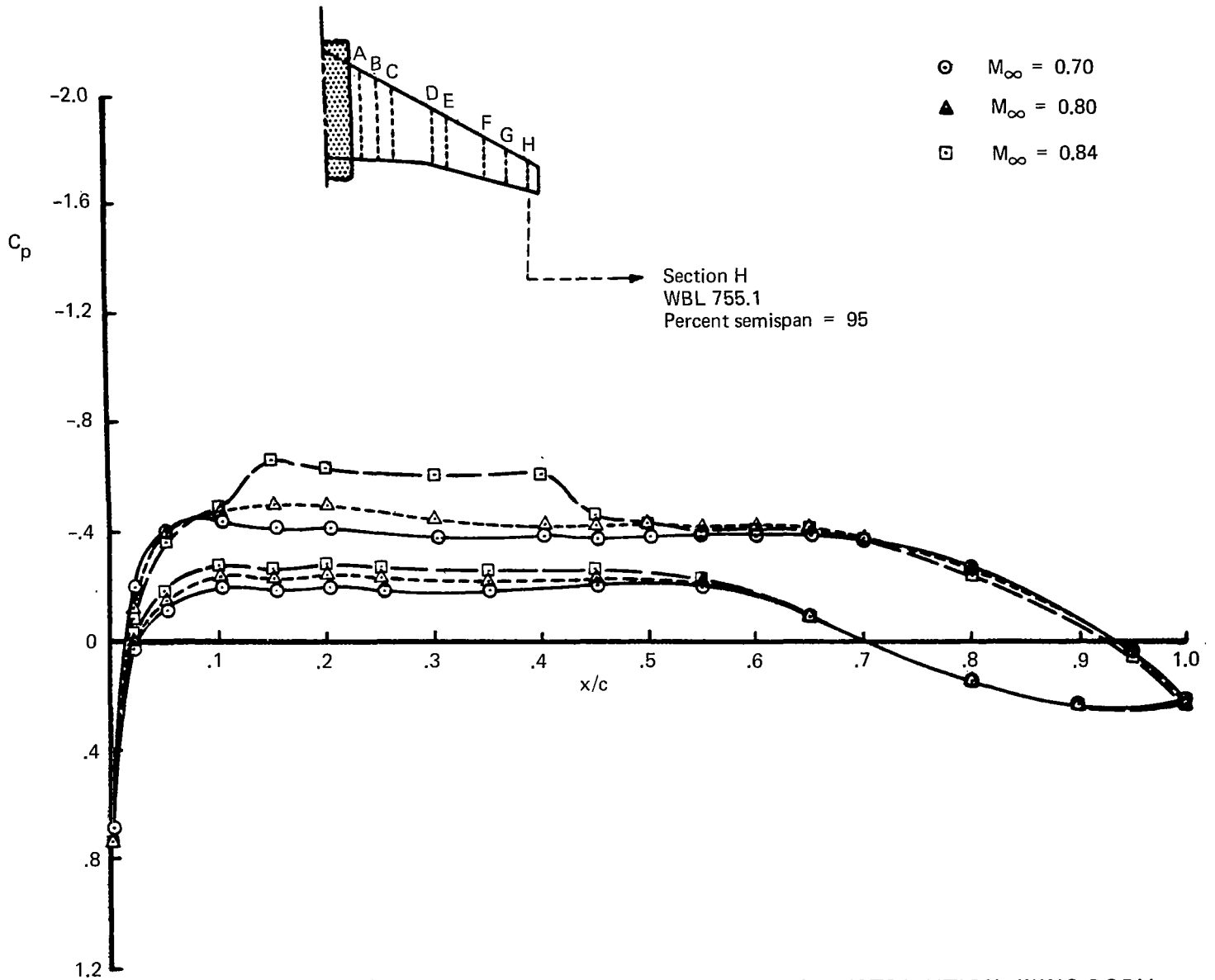

FIGURE 16.–EFFECT OF MACH NUMBER ON WING C_p DISTRIBUTION–WING-BODY ALONE, WIND TUNNEL DATA, $\alpha = 2.3°$

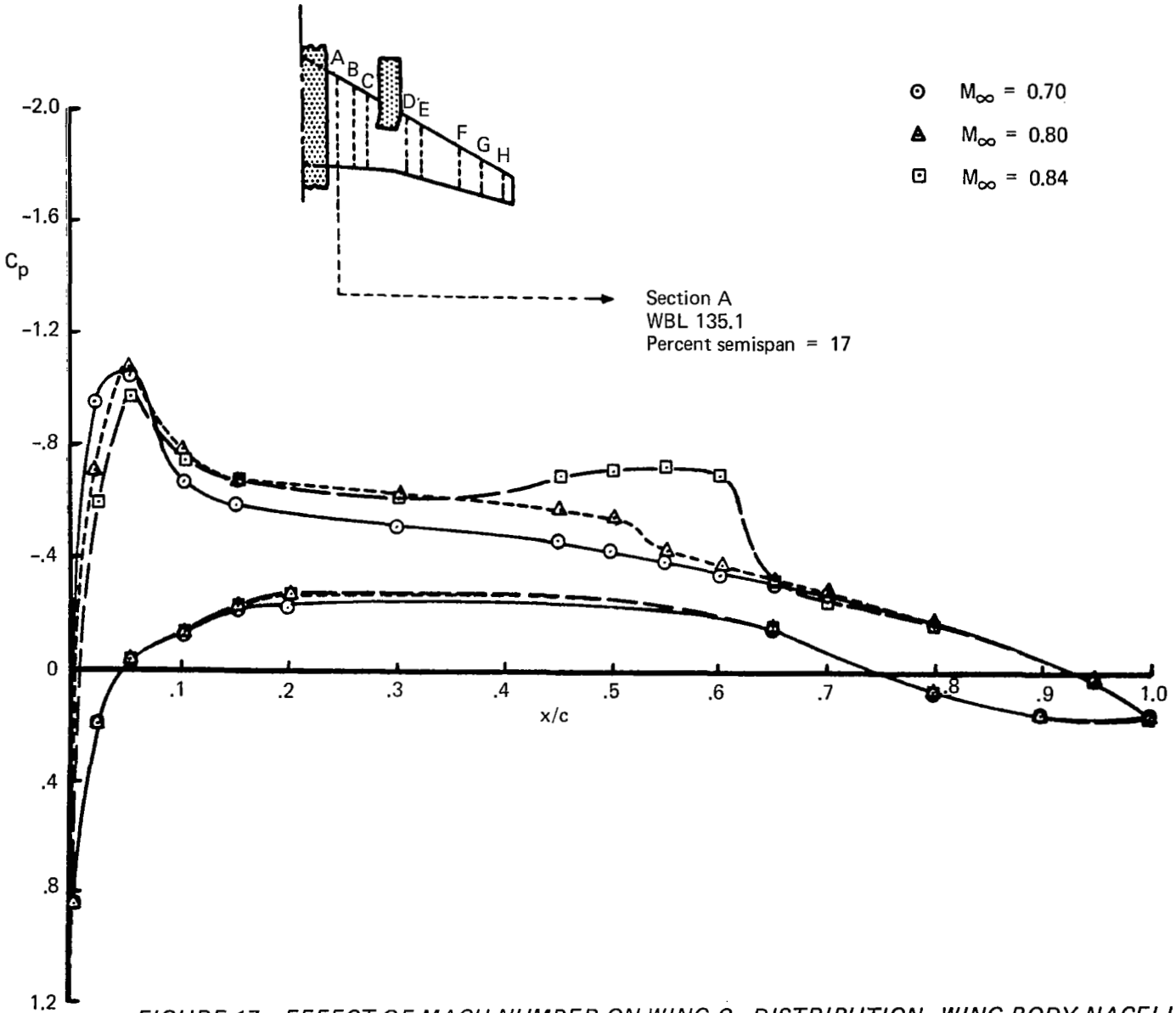

FIGURE 17.—EFFECT OF MACH NUMBER ON WING C_p DISTRIBUTION—WING-BODY-NACELLE, WIND TUNNEL DATA, $\alpha = 2.3°$

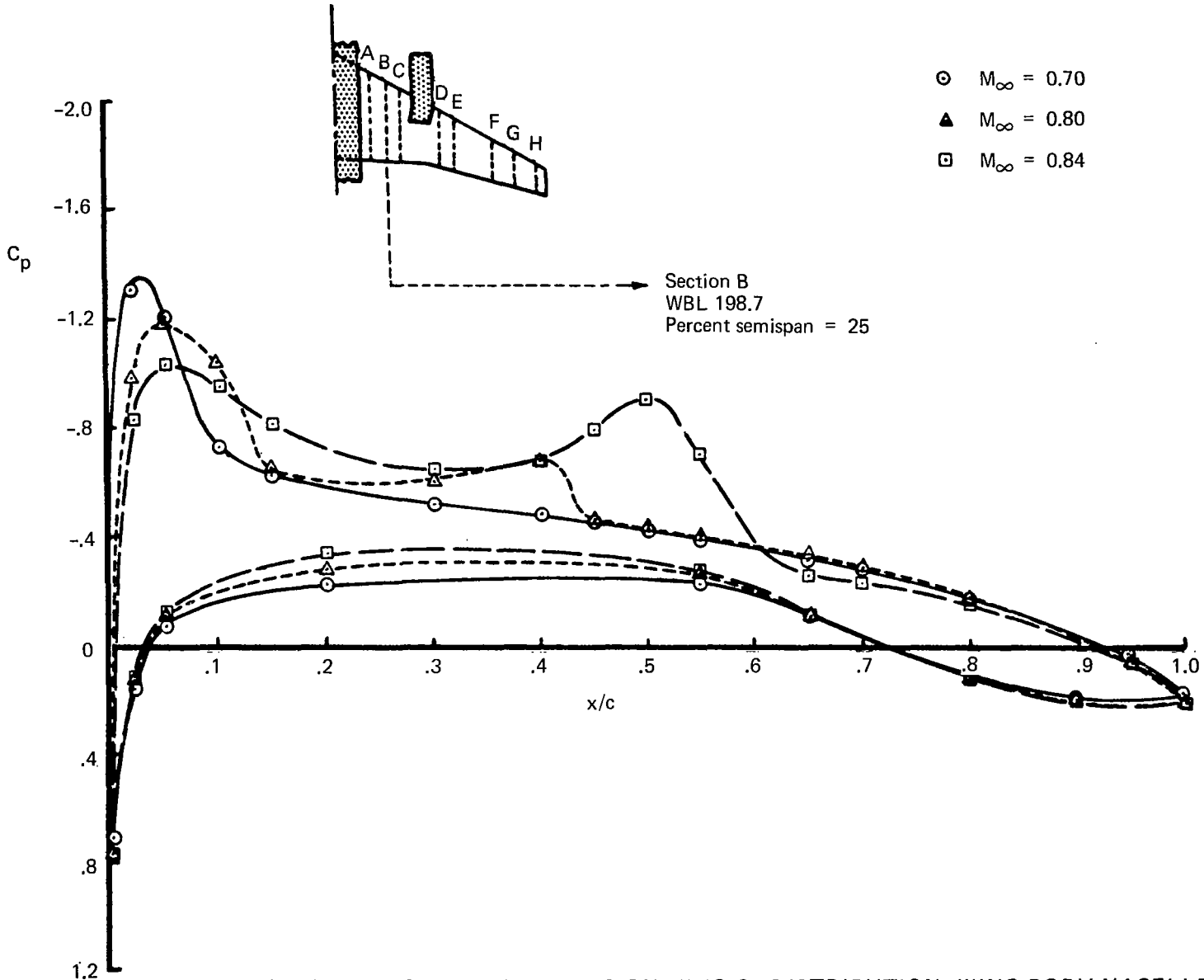

FIGURE 18.—EFFECT OF MACH NUMBER ON WING C_p DISTRIBUTION—WING-BODY-NACELLE, WIND TUNNEL DATA, $\alpha = 2.3°$

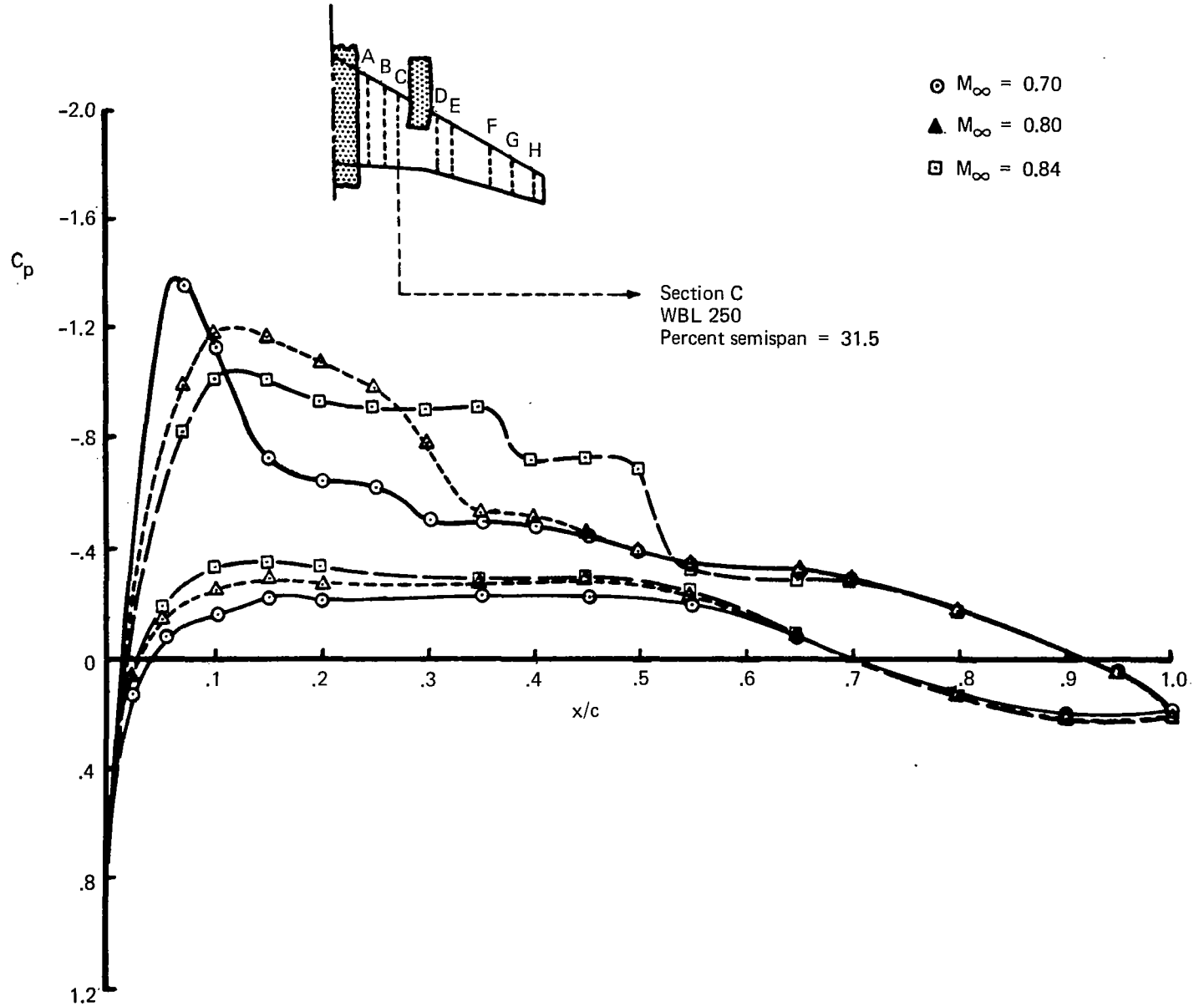

FIGURE 19.–EFFECT OF MACH NUMBER ON WING C_p DISTRIBUTION–WING-BODY-NACELLE, WIND TUNNEL DATA, α= 2.3°

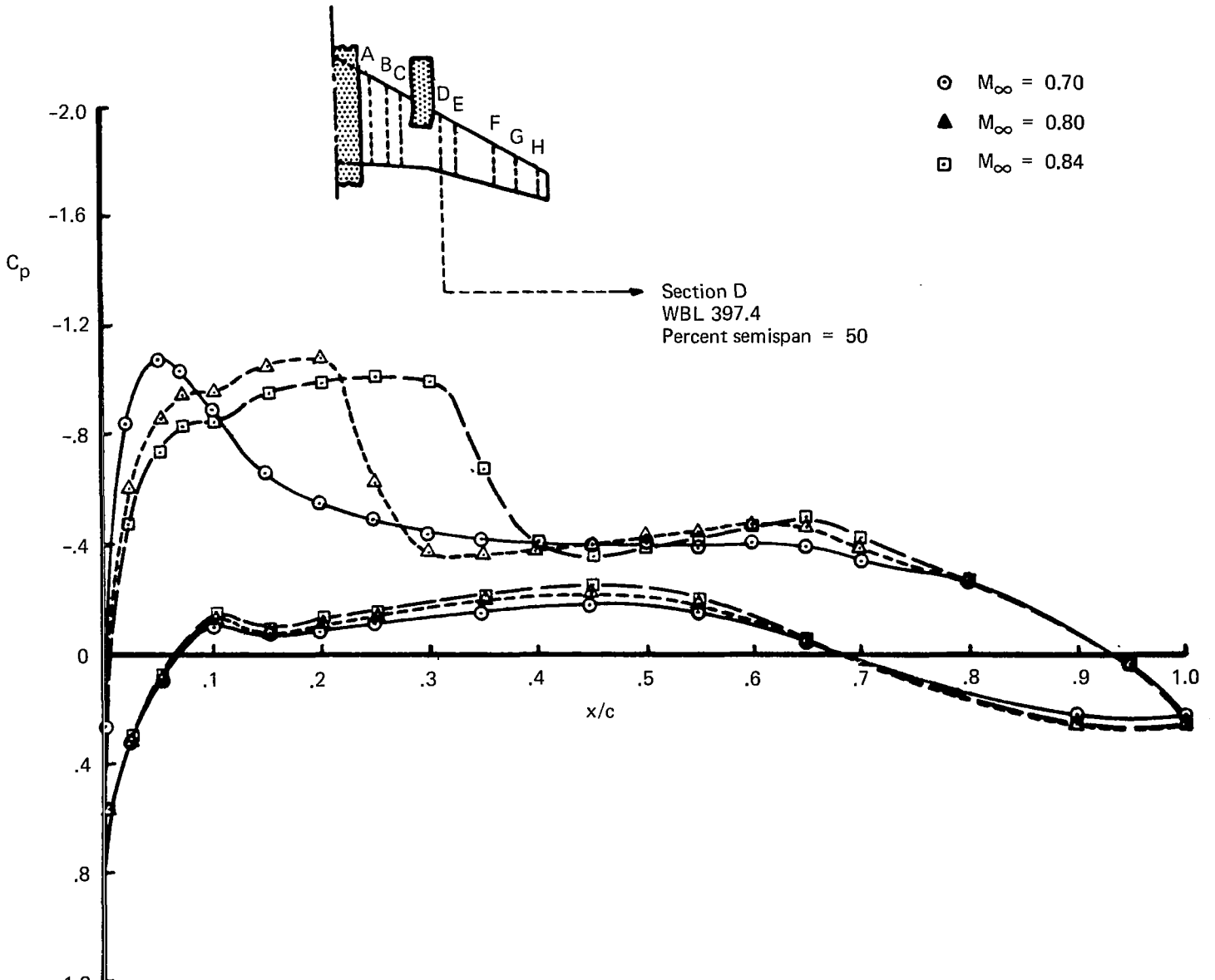

FIGURE 20.–EFFECT OF MACH NUMBER ON WING C_p DISTRIBUTION–WING-BODY-NACELLE, WIND TUNNEL DATA, $\alpha = 2.3°$

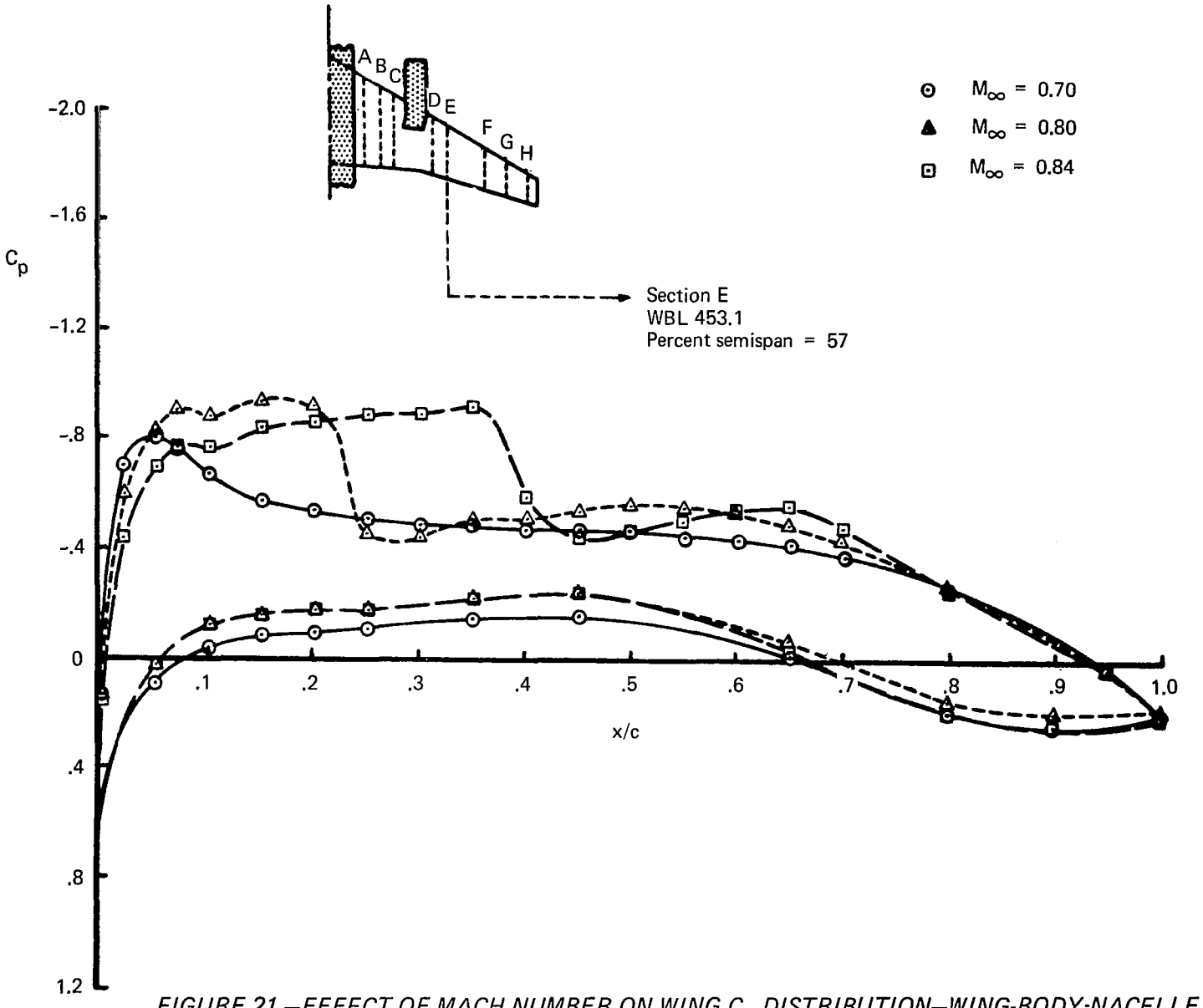

FIGURE 21.—EFFECT OF MACH NUMBER ON WING C_p DISTRIBUTION—WING-BODY-NACELLE, WIND TUNNEL DATA, $\alpha = 2.3°$

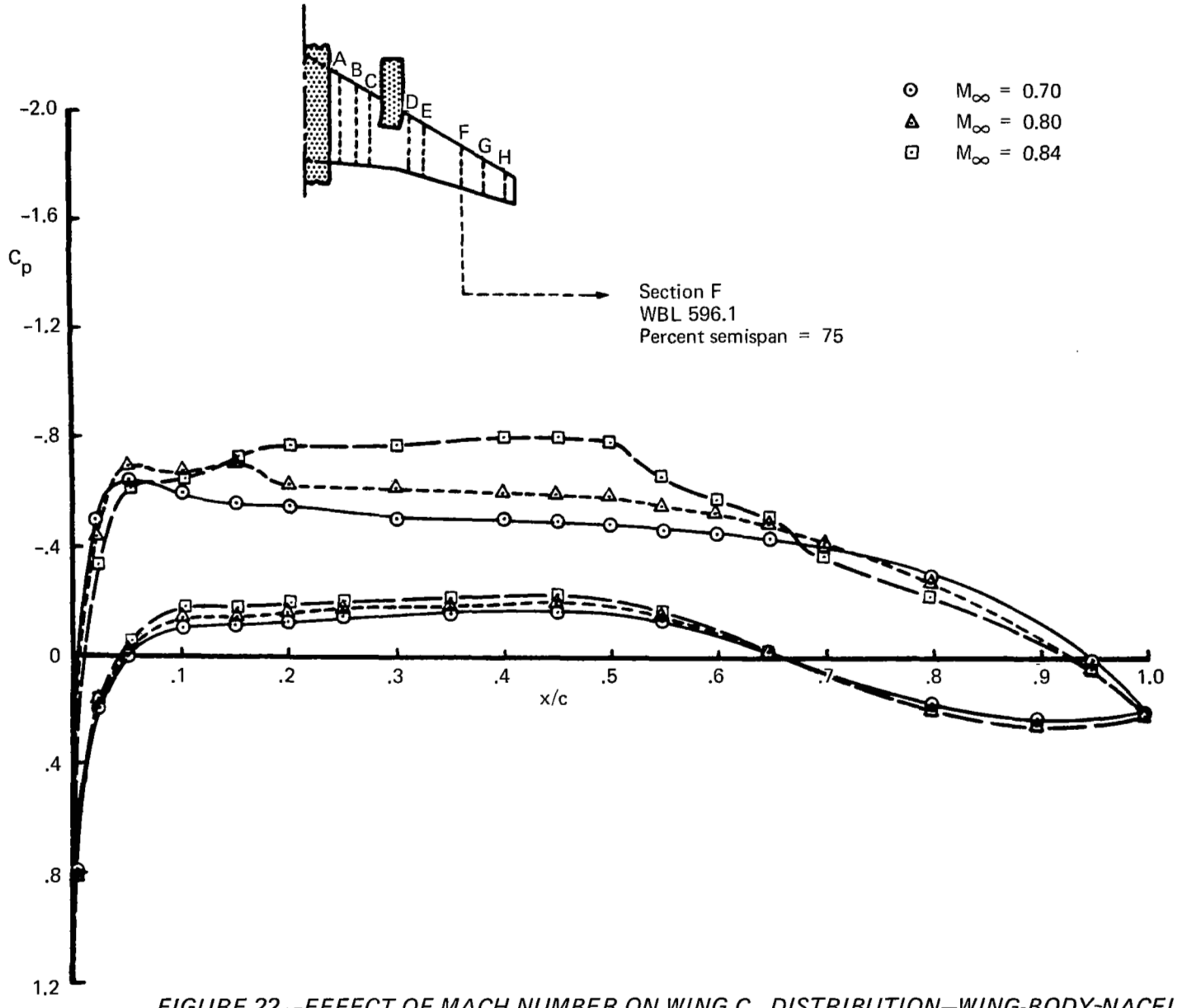

FIGURE 22.–EFFECT OF MACH NUMBER ON WING C_p DISTRIBUTION–WING-BODY-NACELLE, WIND TUNNEL DATA, $\alpha = 2.3°$

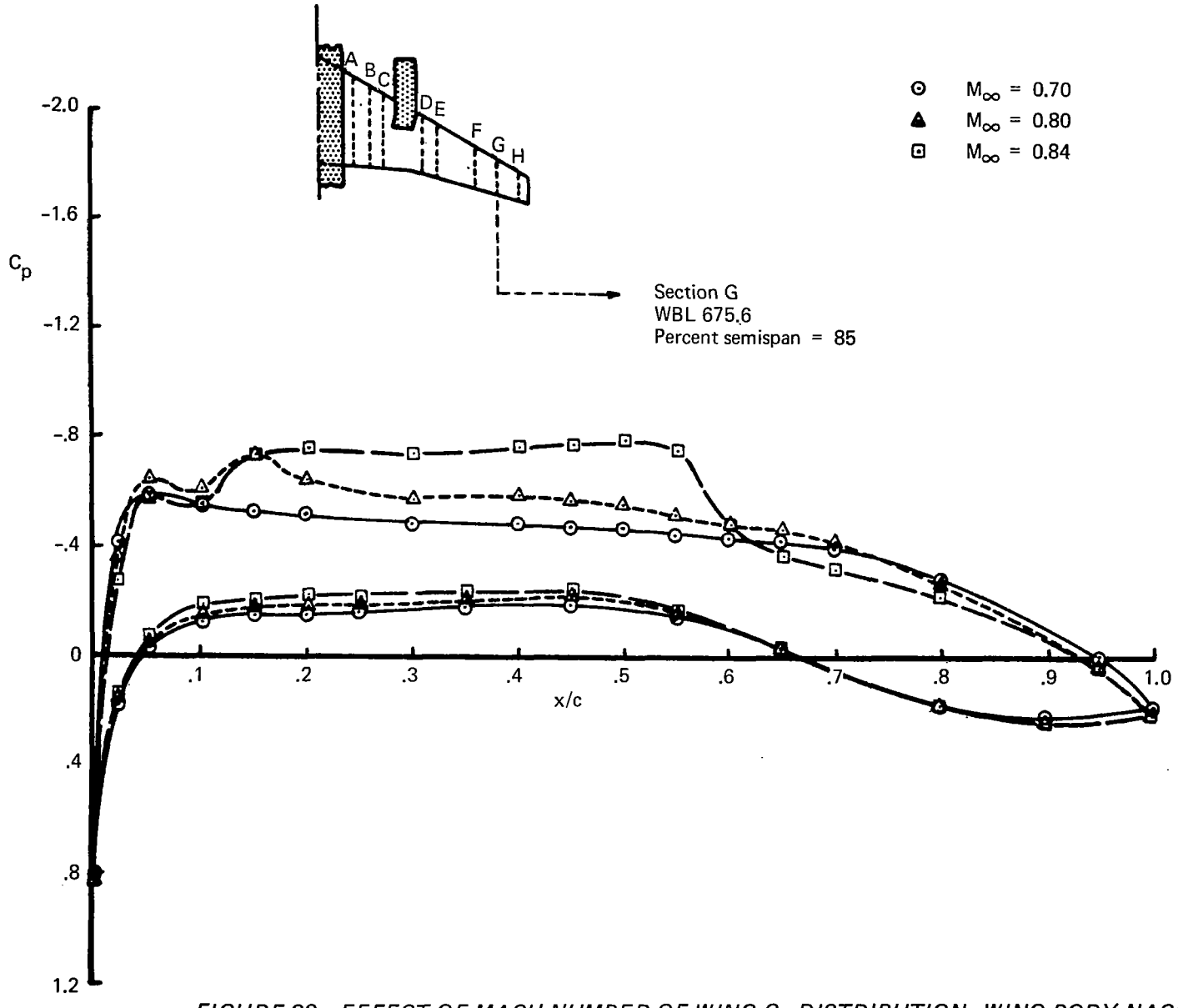

FIGURE 23.—EFFECT OF MACH NUMBER OF WING C_p DISTRIBUTION—WING-BODY-NACELLE, WIND TUNNEL DATA, $\alpha = 2.3^\circ$

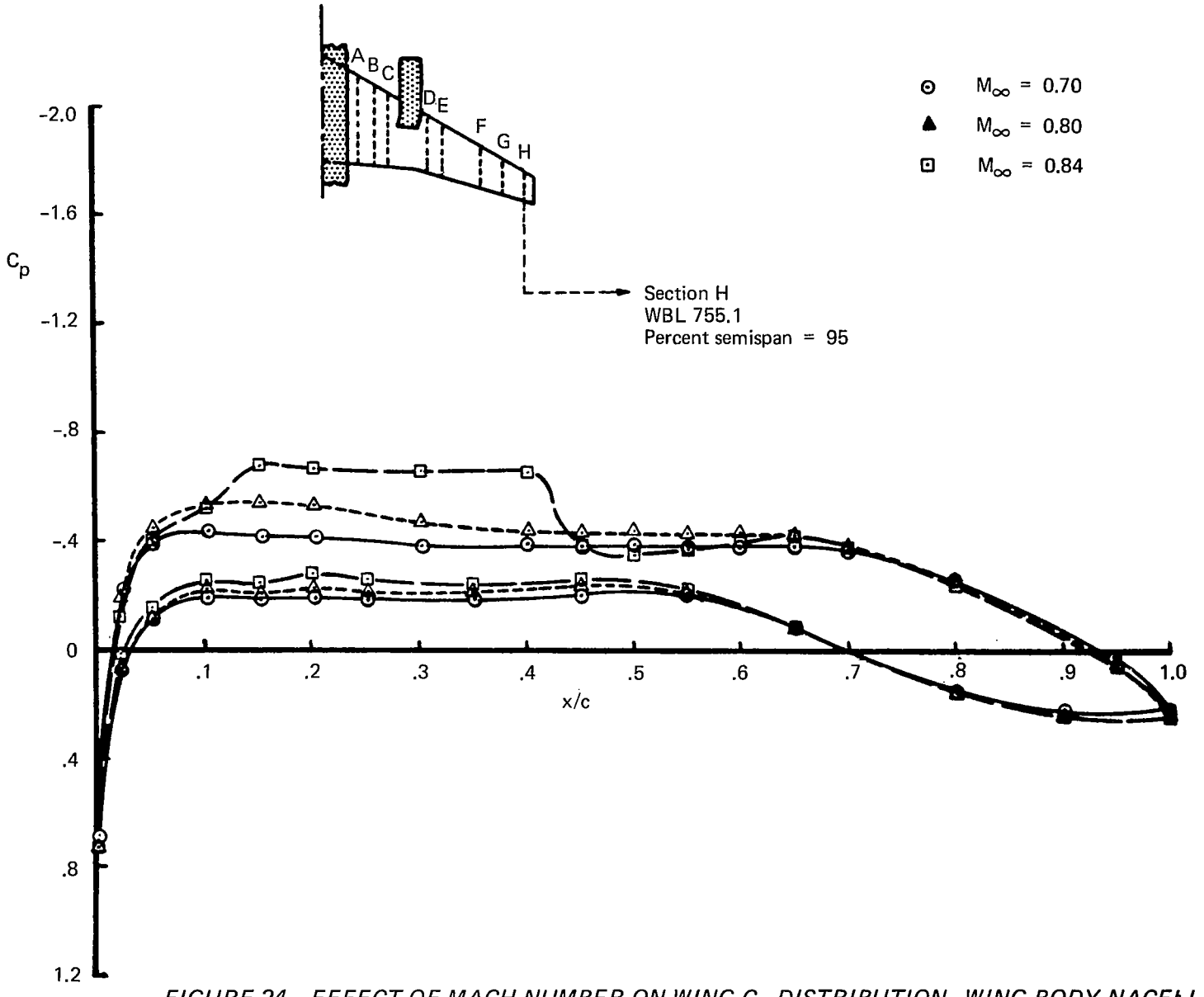

FIGURE 24.–EFFECT OF MACH NUMBER ON WING C_p DISTRIBUTION–WING-BODY-NACELLE, WIND TUNNEL DATA, $\alpha = 2.3°$

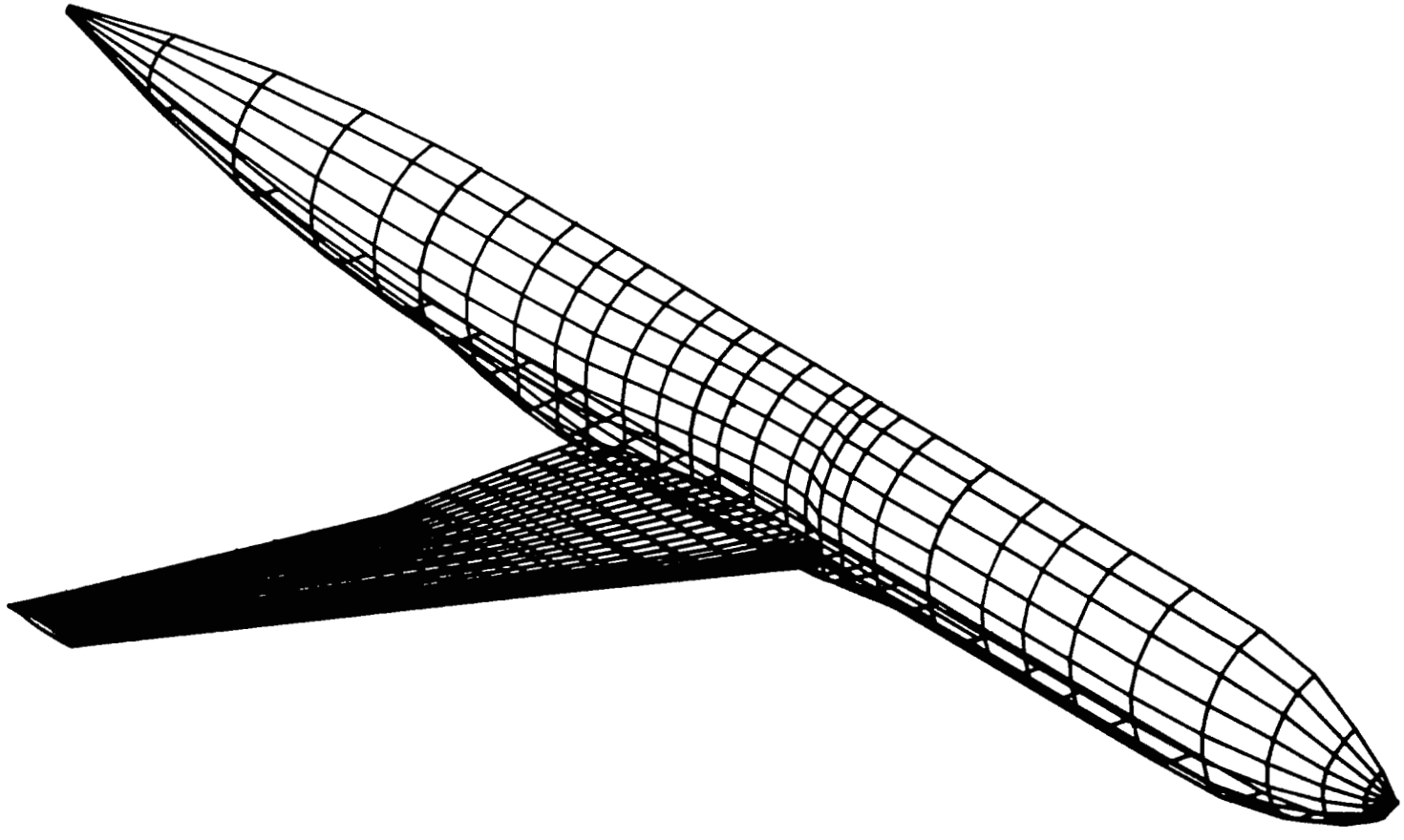

FIGURE 25.—SOURCE PANEL REPRESENTATION OF WING-BODY FOR TEA-230 ANALYSIS

FIGURE 26.—LIFTING SYSTEM PANELS OF WING-BODY FOR TEA-230 ANALYSIS

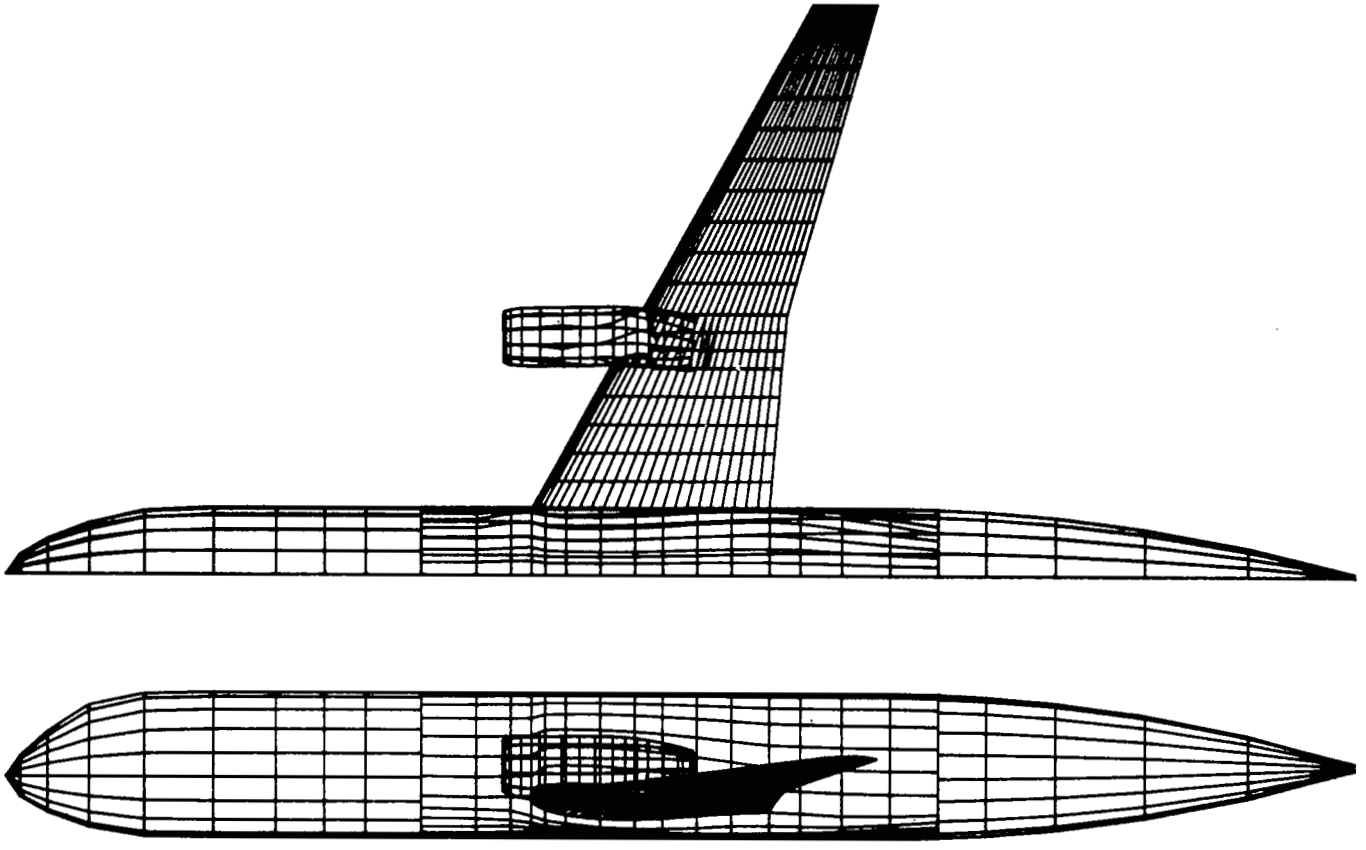

FIGURE 27.—PLAN AND SIDE VIEWS OF TEA-230 SOURCE PANEL REPRESENTATION OF WING-BODY-NACELLE

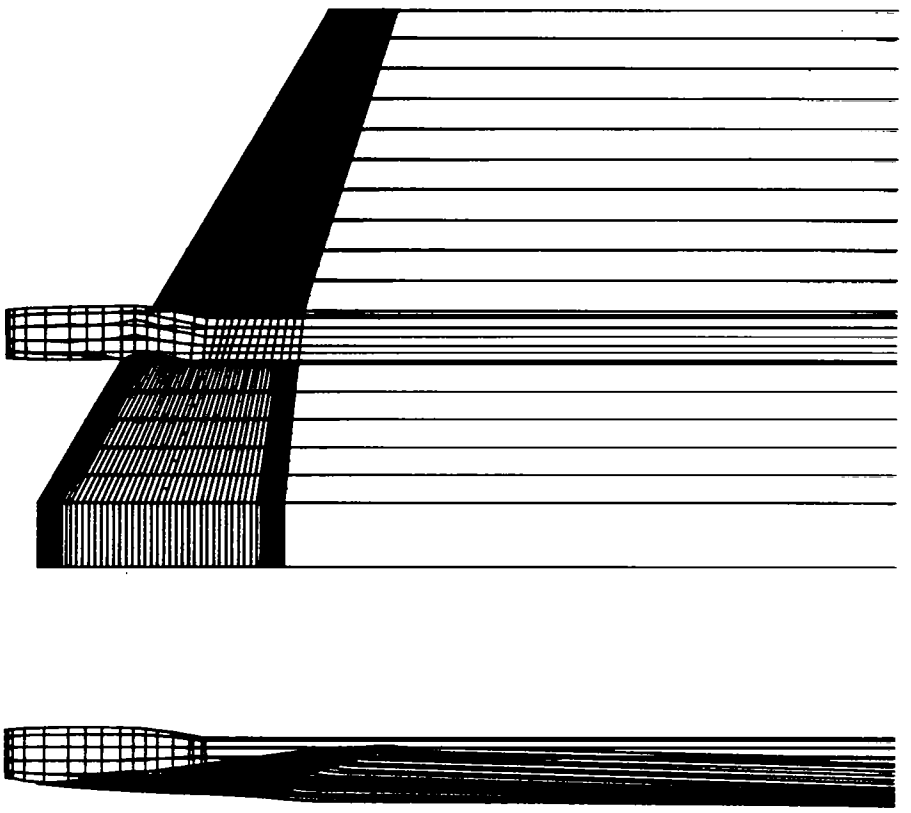

FIGURE 28.—PLAN AND SIDE VIEWS OF TEA-230 LIFTING SYSTEM PANELS FOR WING-BODY-NACELLE

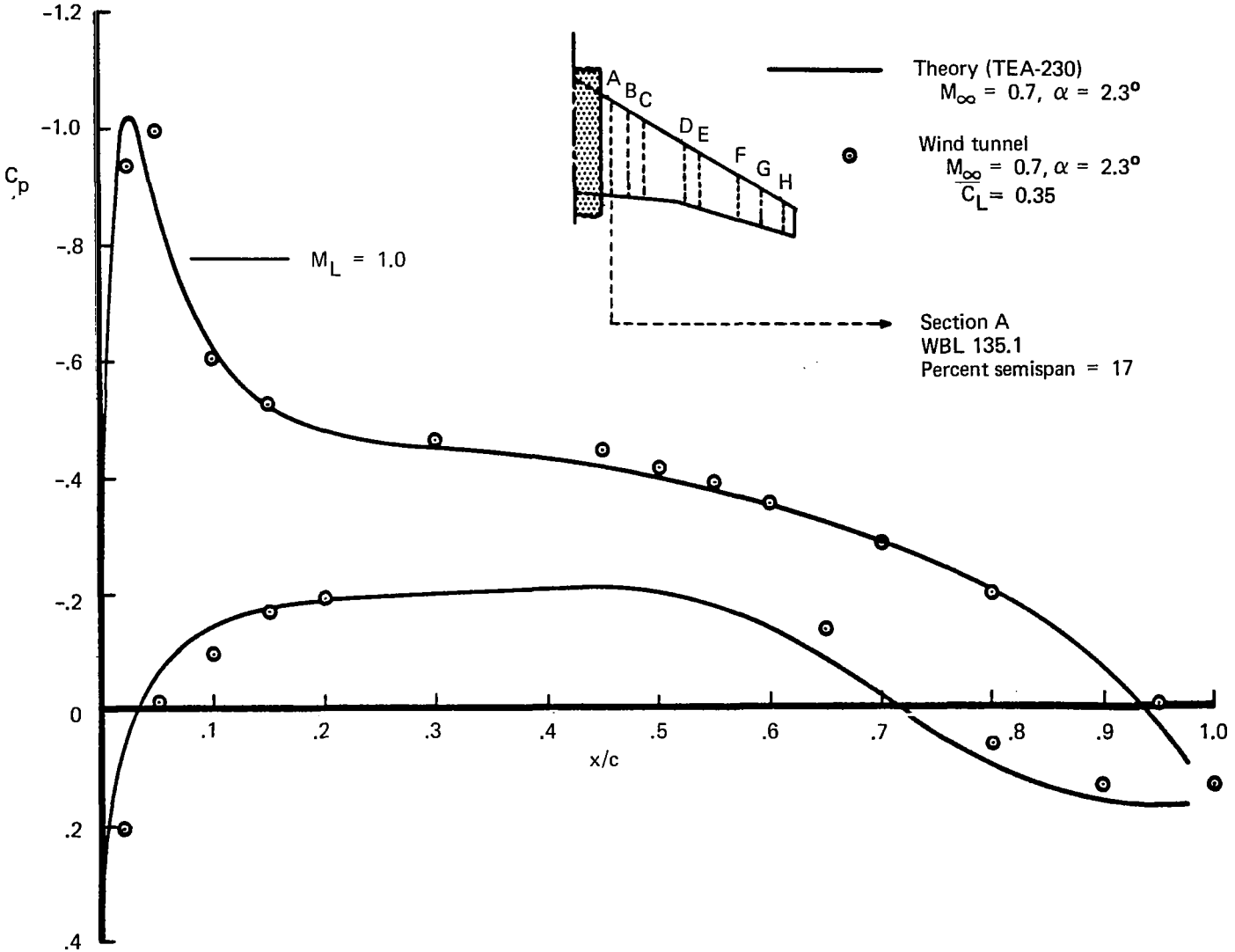

FIGURE 29.—COMPARISON OF WING PRESSURE DISTRIBUTION FROM TEA-230 ANALYSIS WITH WIND TUNNEL DATA—WING-BODY CONFIGURATION

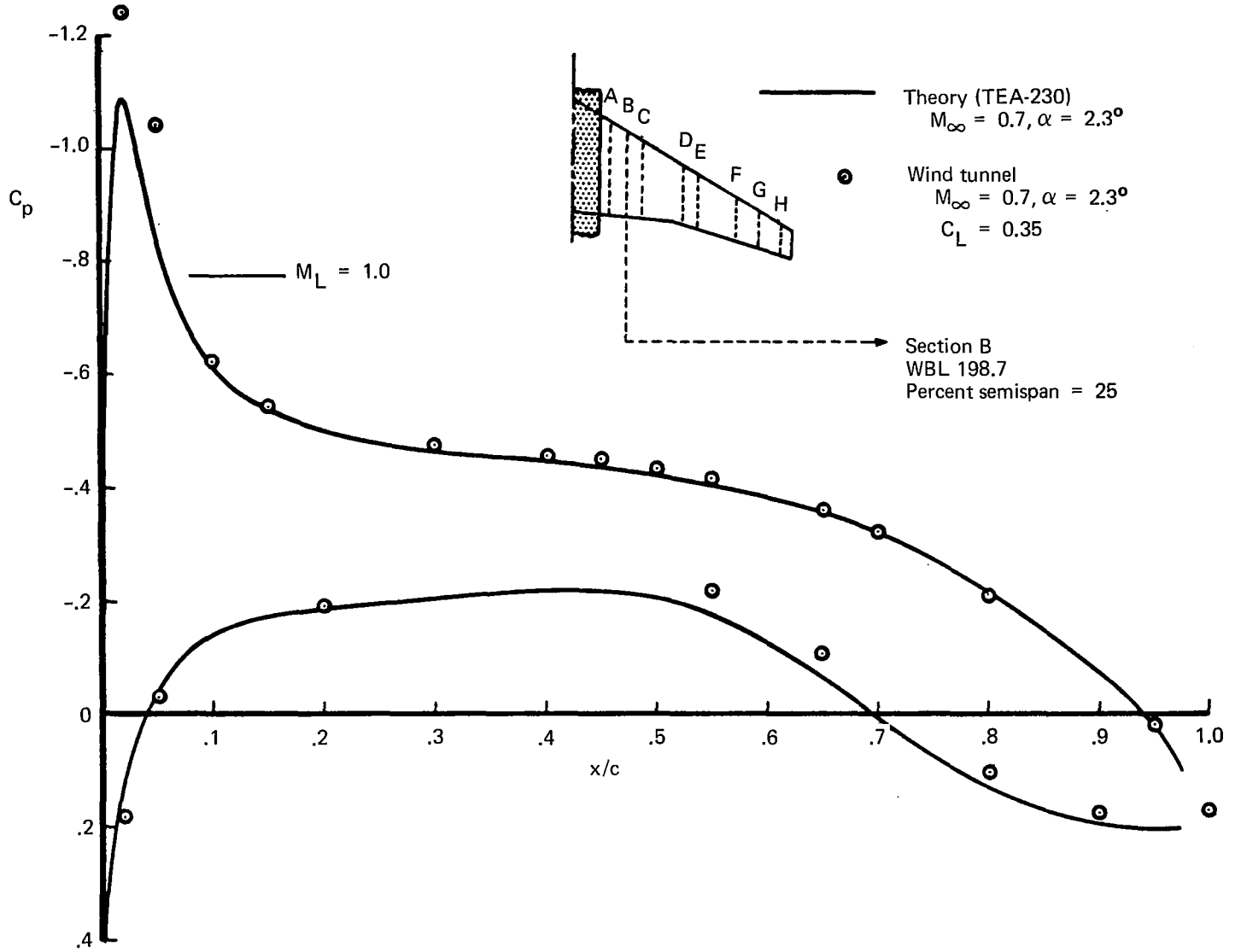

FIGURE 30.–COMPARISON OF WING PRESSURE DISTRIBUTION FROM TEA-230 ANALYSIS WITH WIND TUNNEL DATA–WING-BODY CONFIGURATION

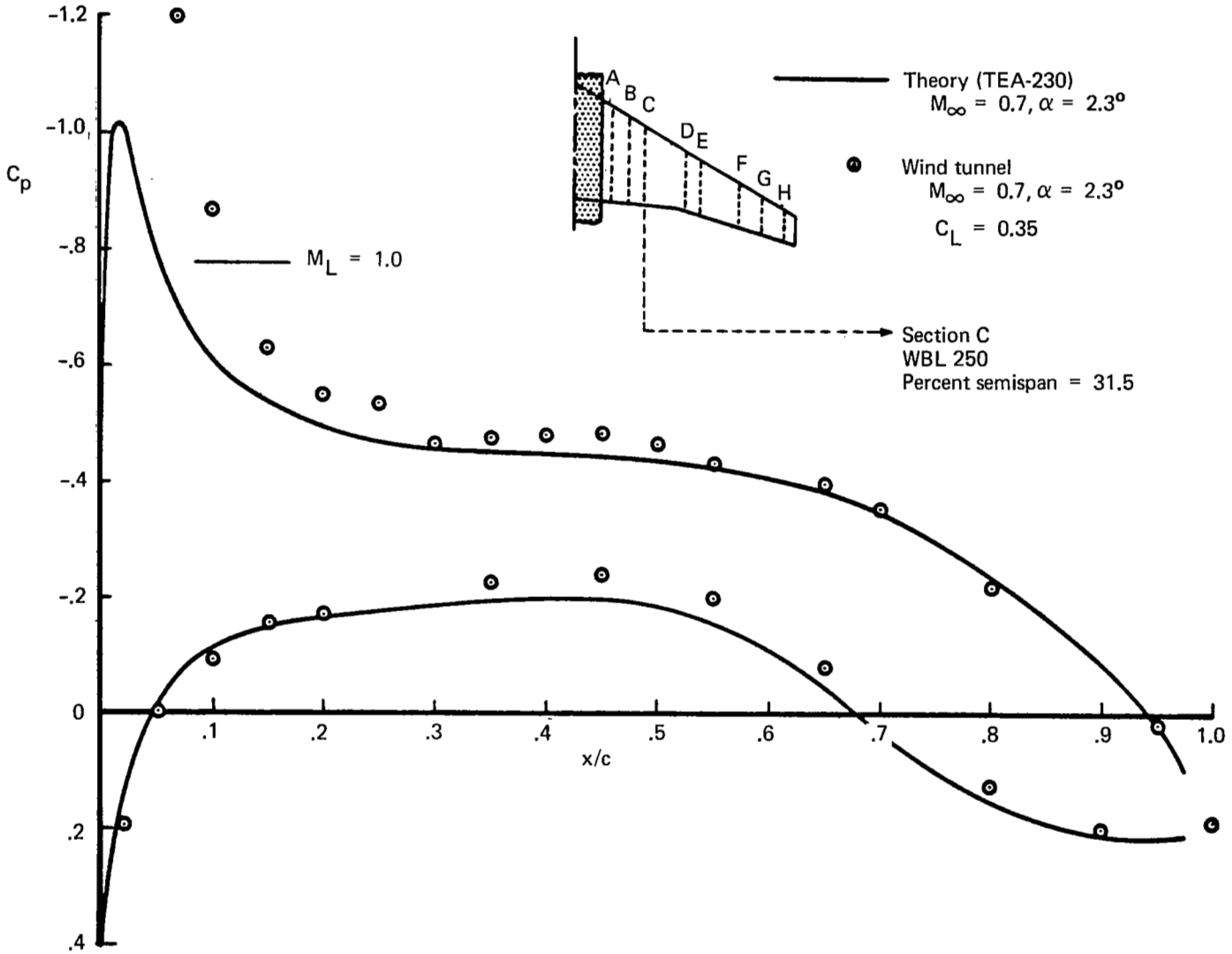

FIGURE 31.—COMPARISON OF WING PRESSURE DISTRIBUTION FROM TEA-230 ANALYSIS WITH WIND TUNNEL DATA—WING-BODY CONFIGURATION

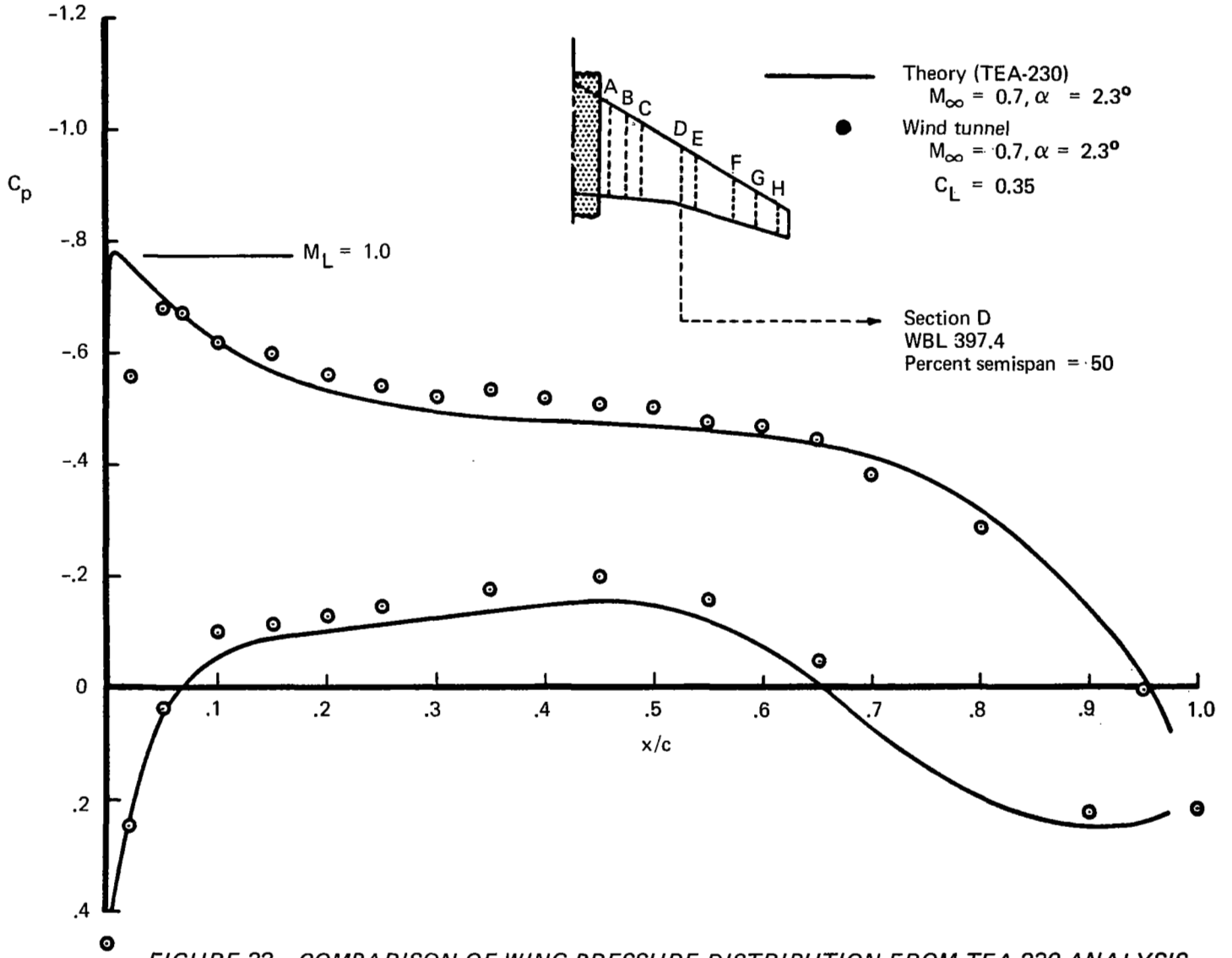

FIGURE 32.—COMPARISON OF WING PRESSURE DISTRIBUTION FROM TEA-230 ANALYSIS WITH WIND TUNNEL DATA—WING-BODY CONFIGURATION

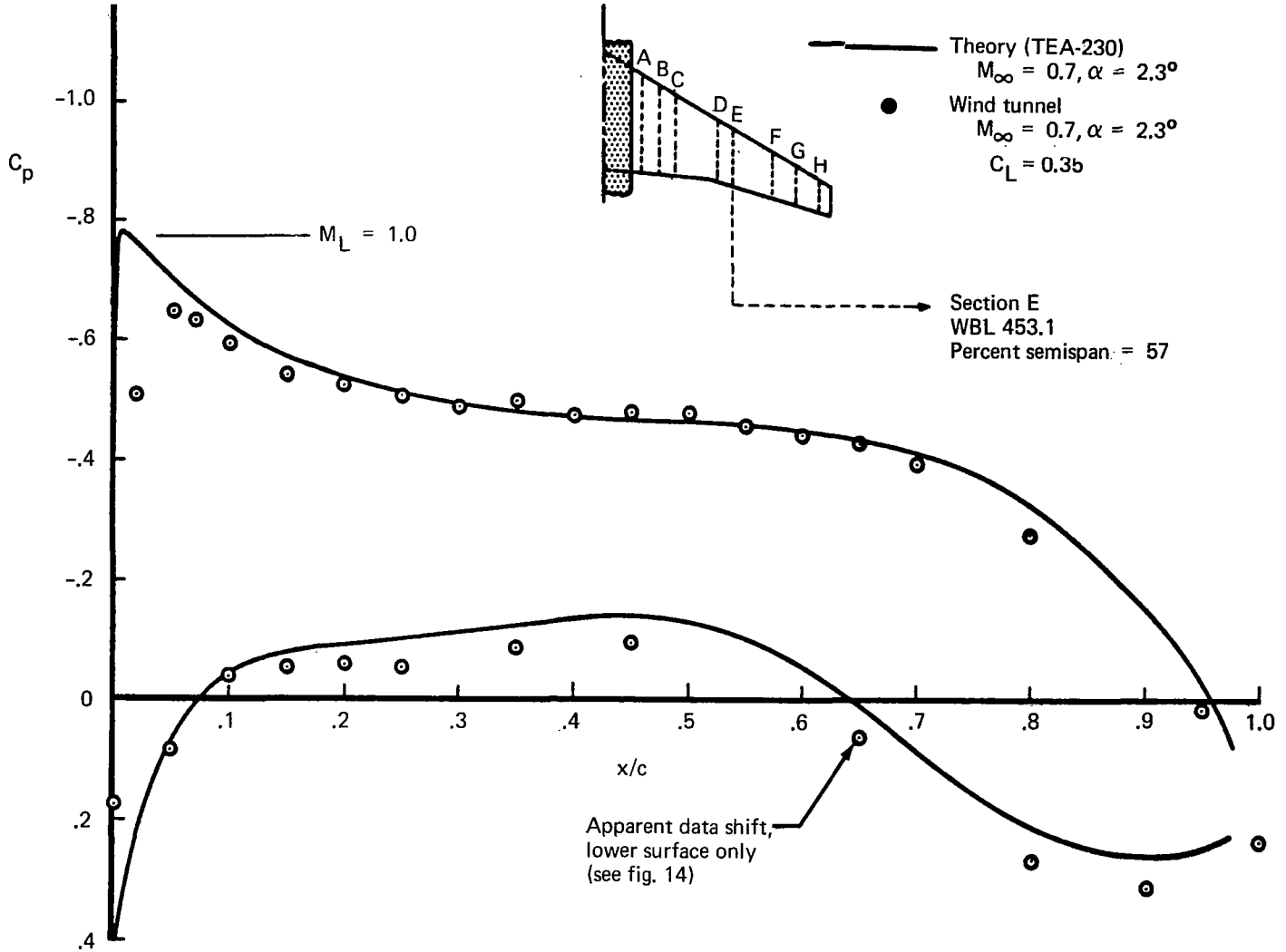

FIGURE 33.—COMPARISON OF WING PRESSURE DISTRIBUTION FROM TEA-230 ANALYSIS WITH WIND TUNNEL DATA—WING-BODY CONFIGURATION

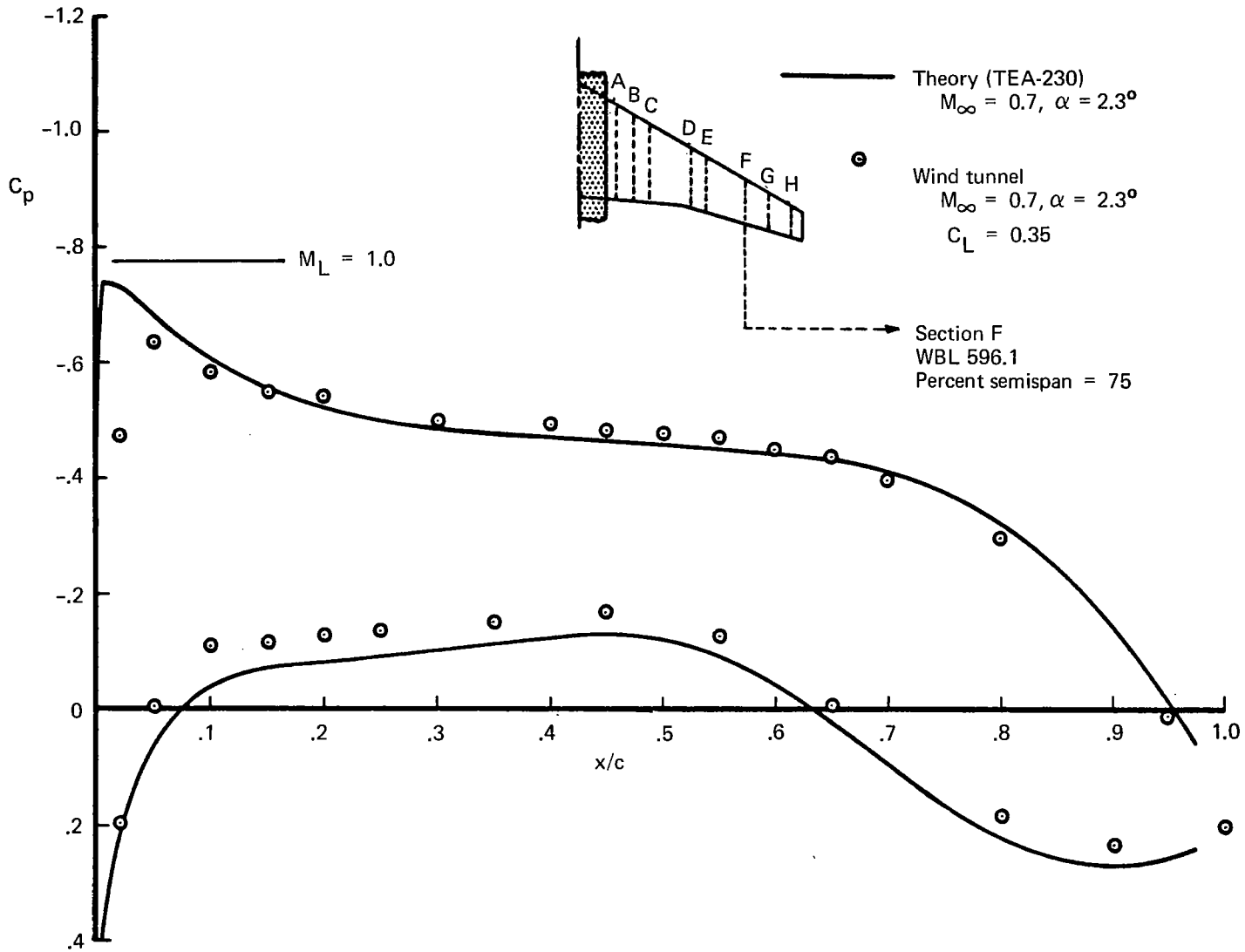

FIGURE 34.—COMPARISON OF WING PRESSURE DISTRIBUTION FROM TEA-230 ANALYSIS WITH WIND TUNNEL DATA—WING-BODY CONFIGURATION

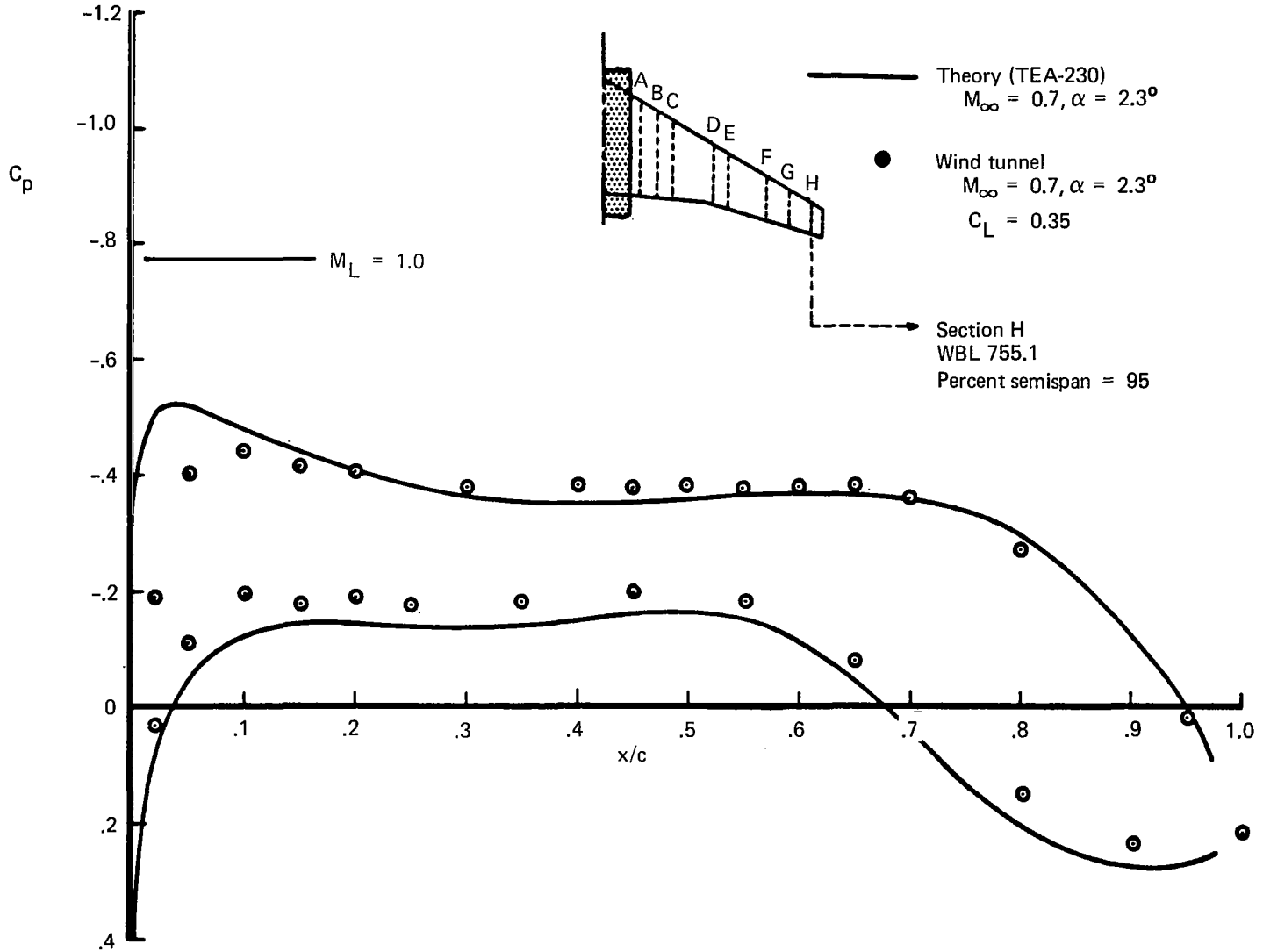

FIGURE 35.—COMPARISON OF WING PRESSURE DISTRIBUTION FROM TEA-230 ANALYSIS WITH WIND TUNNEL DATA—WING-BODY CONFIGURATION

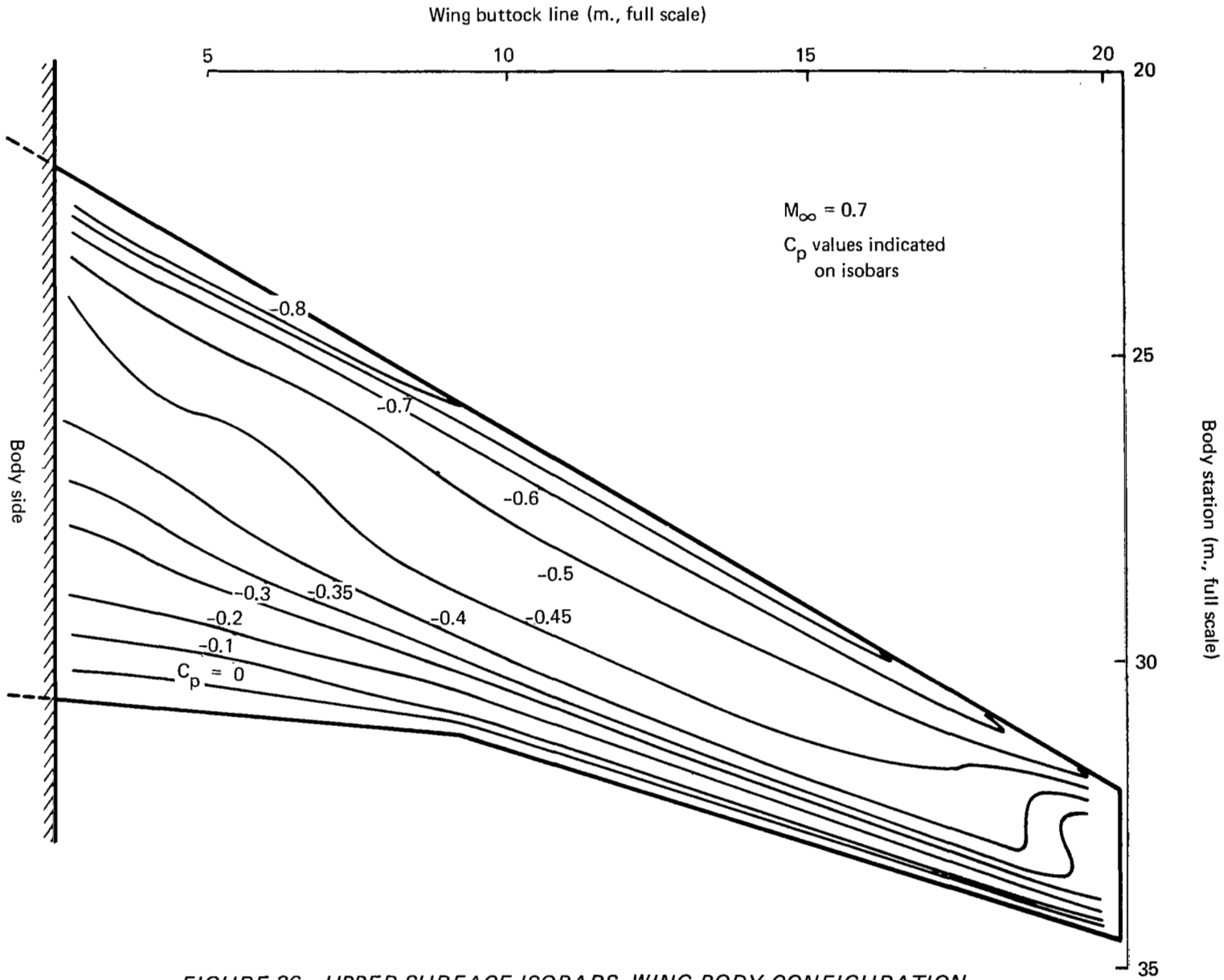

FIGURE 36.—UPPER-SURFACE ISOBARS, WING-BODY CONFIGURATION TEA-230 ANALYSIS

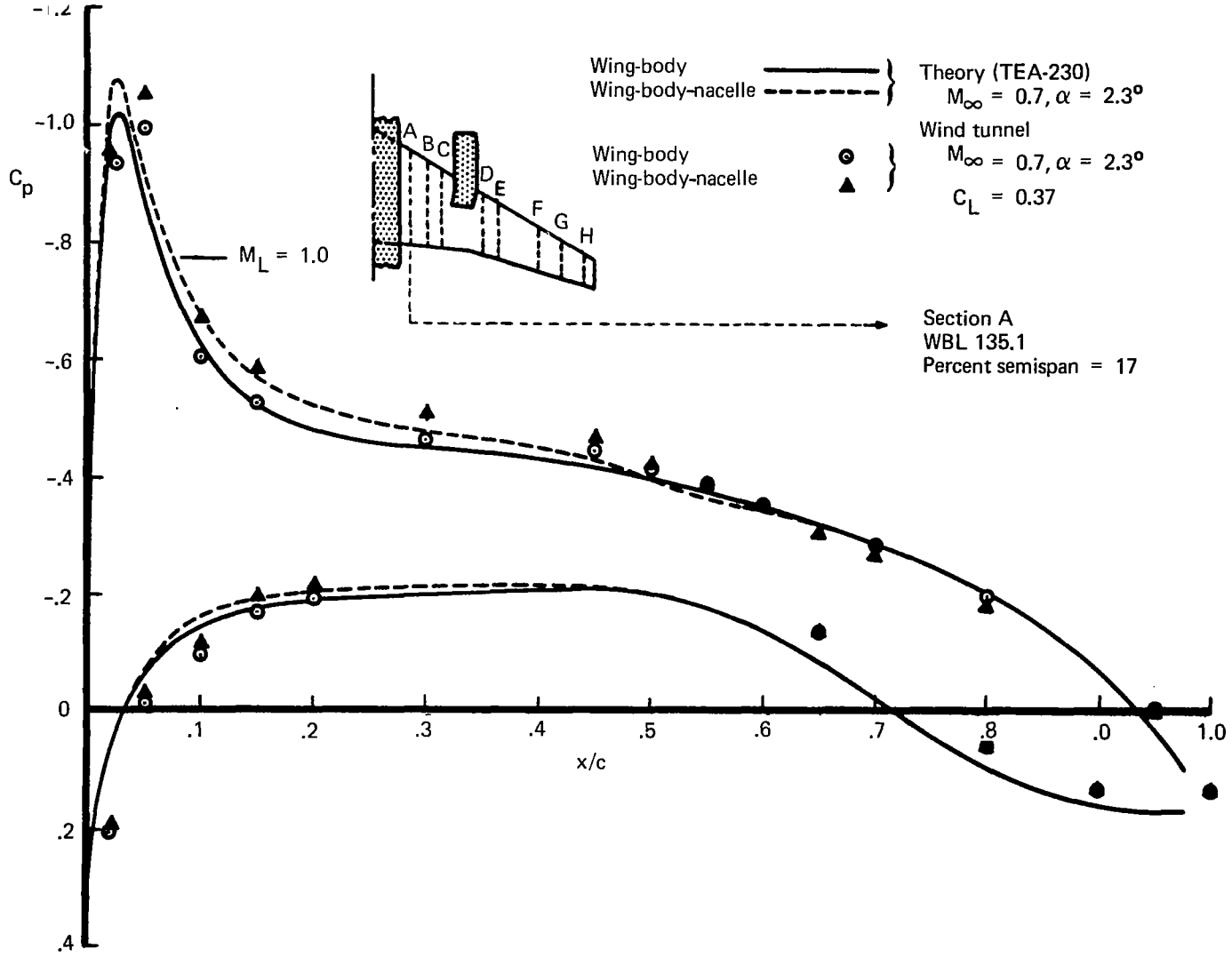

FIGURE 37.—COMPARISON OF WING PRESSURE DISTRIBUTION FROM TEA-230 ANALYSIS WITH WIND TUNNEL DATA—WING-BODY-NACELLE CONFIGURATION

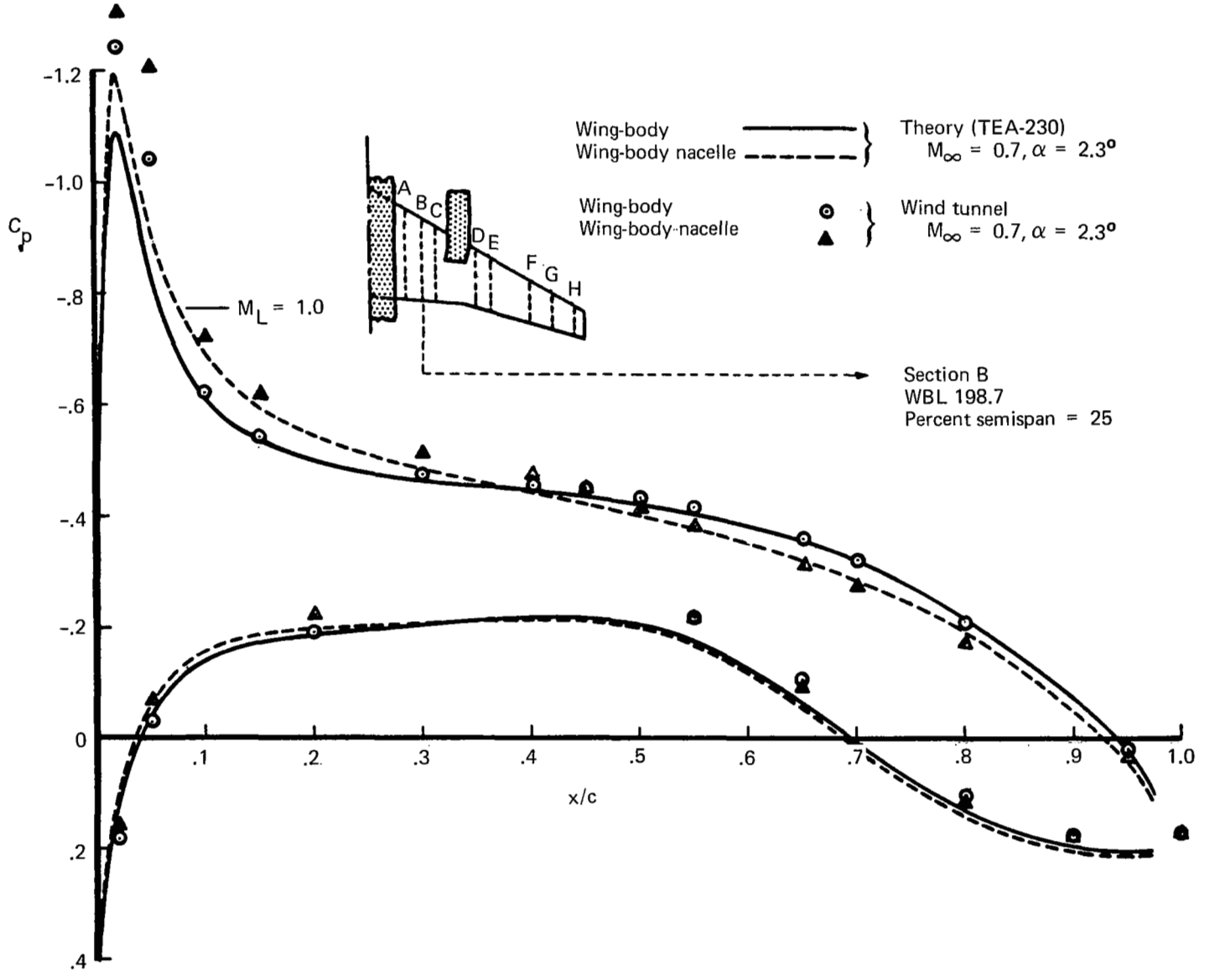

FIGURE 38.–COMPARISON OF WING PRESSURE DISTRIBUTION FROM TEA-230 ANALYSIS WITH WIND TUNNEL DATA–WING-BODY-NACELLE CONFIGURATION

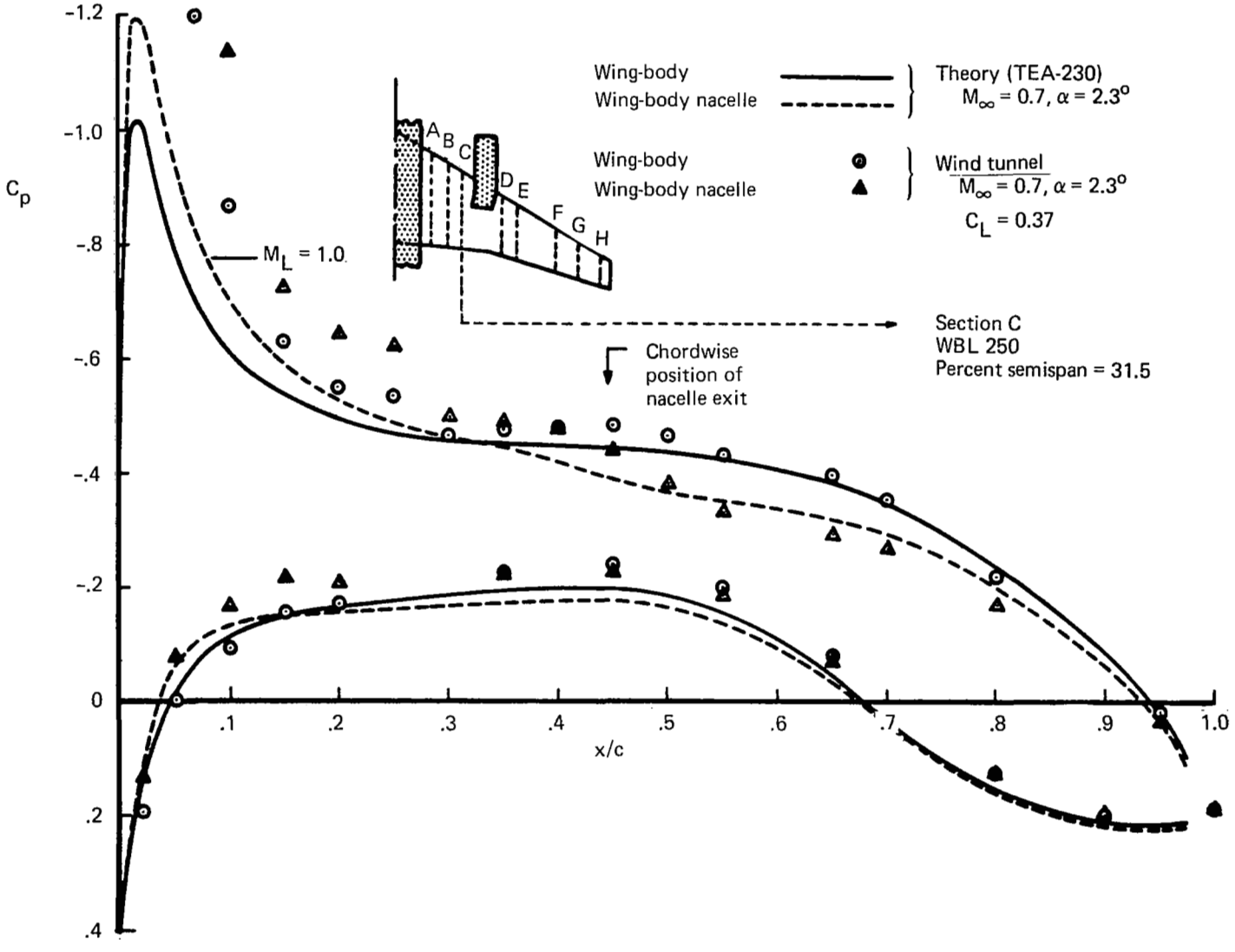

FIGURE 39.–COMPARISON OF WING PRESSURE DISTRIBUTION FROM TEA-230 ANALYSIS WITH WIND TUNNEL DATA–WING-BODY-NACELLE CONFIGURATION

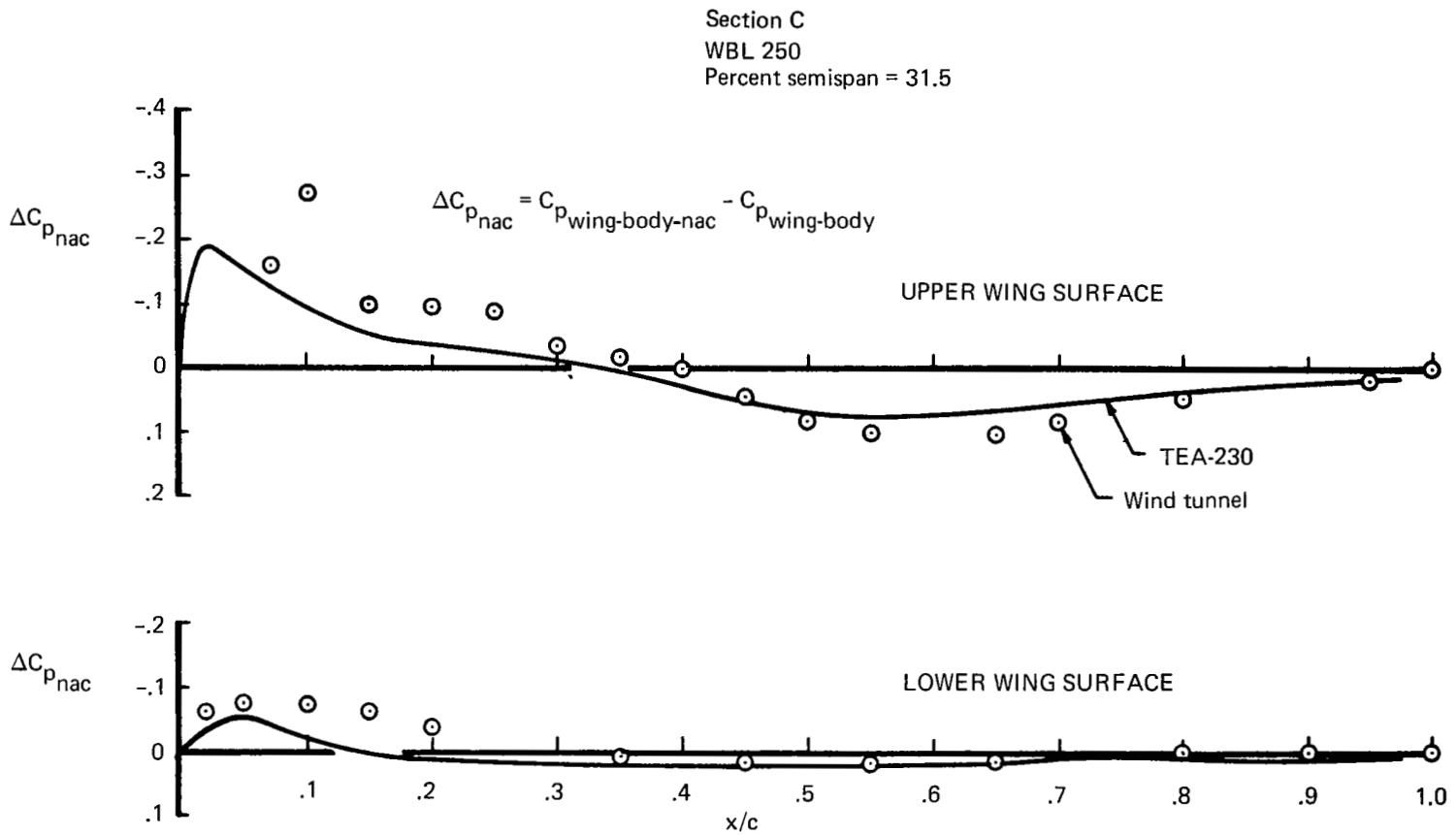

FIGURE 40.—INCREMENT IN CHORDWISE C_p DISTRIBUTION AT SECTION C DUE TO ADDITION OF NACELLE—TEA-230 VS WIND TUNNEL DATA

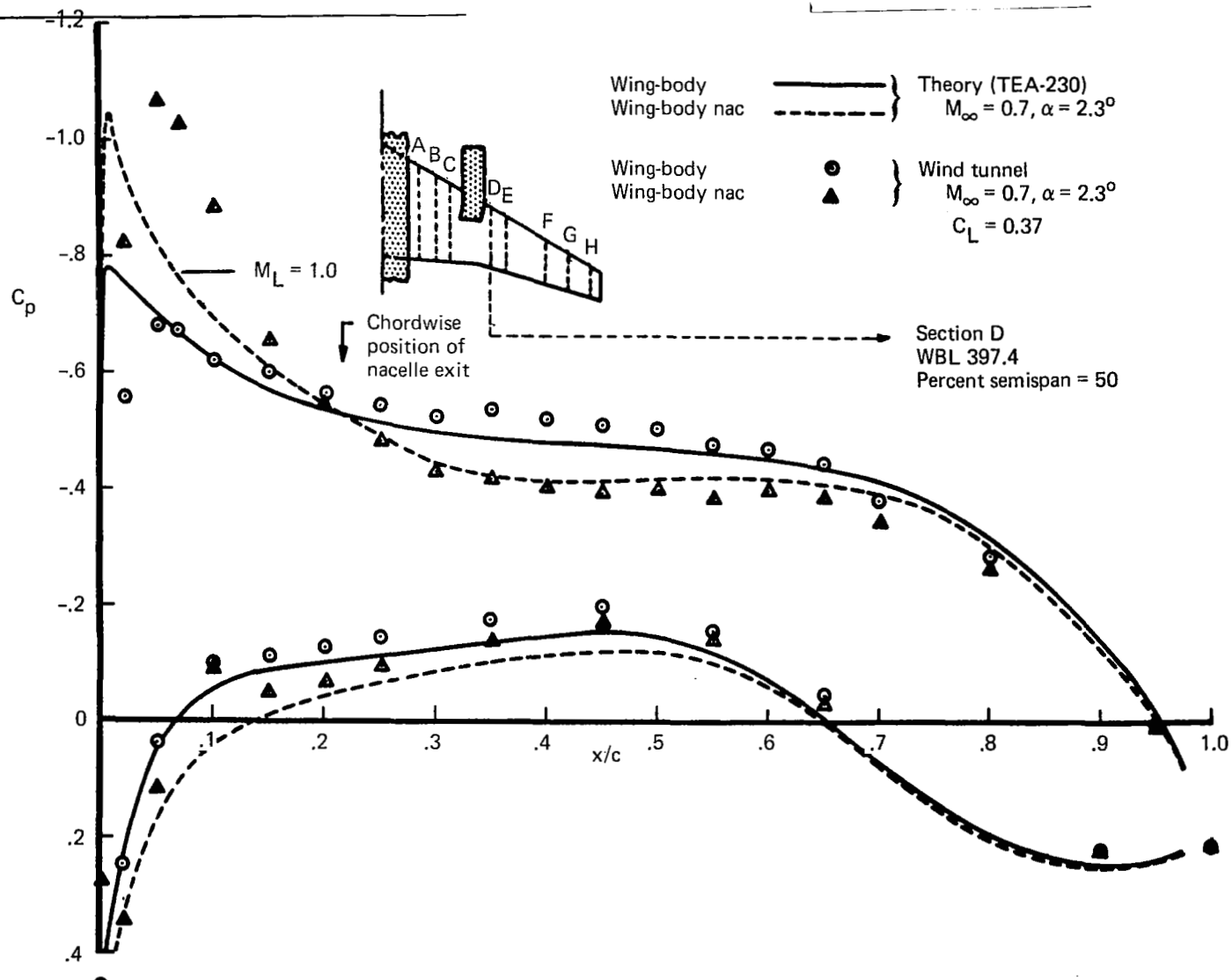

FIGURE 41.—COMPARISON OF WING PRESSURE DISTRIBUTION FROM TEA-230 ANALYSIS WITH WIND TUNNEL DATA—WING-BODY-NACELLE CONFIGURATION

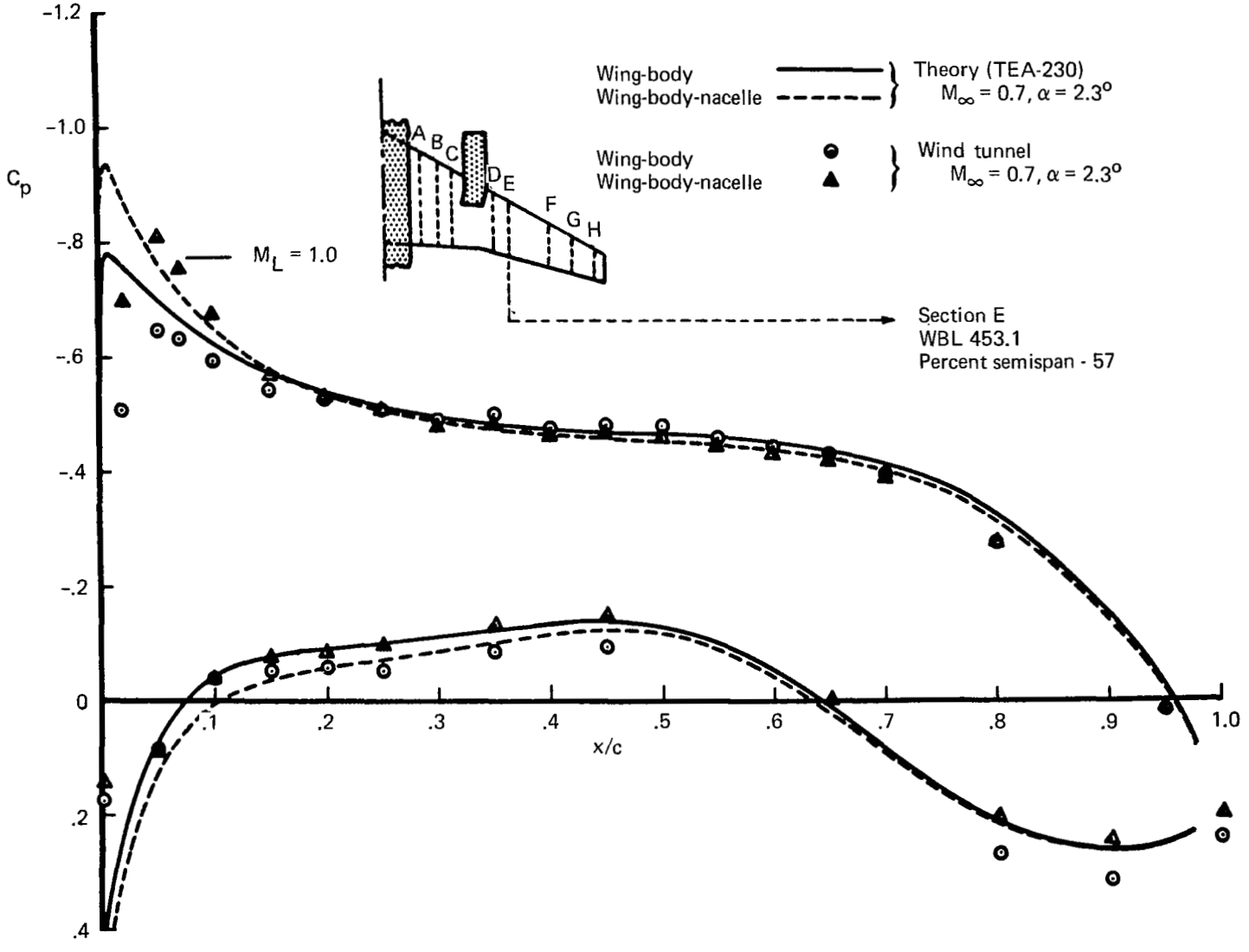

FIGURE 42.–COMPARISON OF WING PRESSURE DISTRIBUTION FROM TEA-230 ANALYSIS WITH WIND TUNNEL DATA FOR THE ELECTRONIC CONFIGURATION

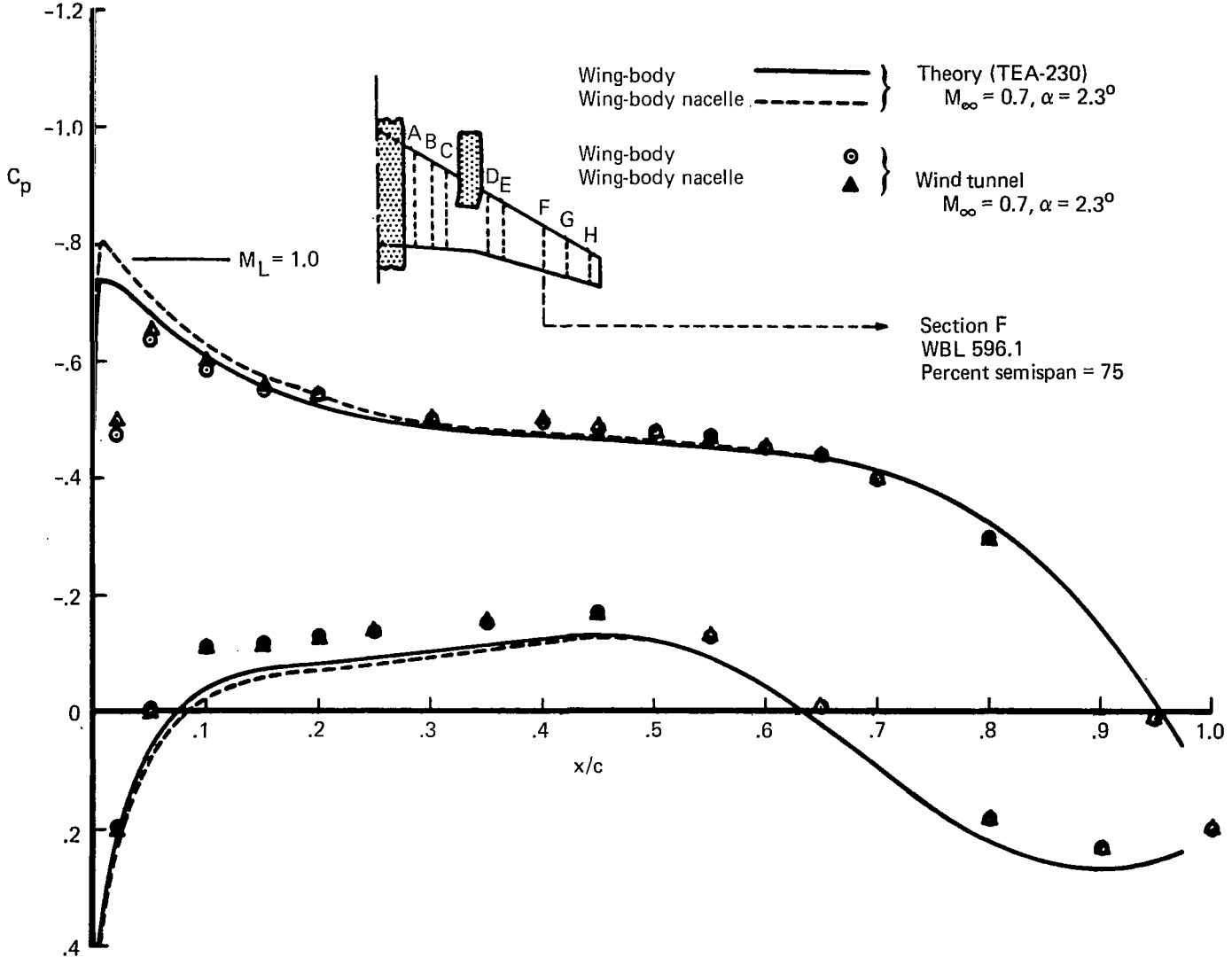

FIGURE 43.–COMPARISON OF WING PRESSURE DISTRIBUTION FROM TEA-230 ANALYSIS WITH WIND TUNNEL DATA–WING-BODY-NACELLE CONFIGURATION

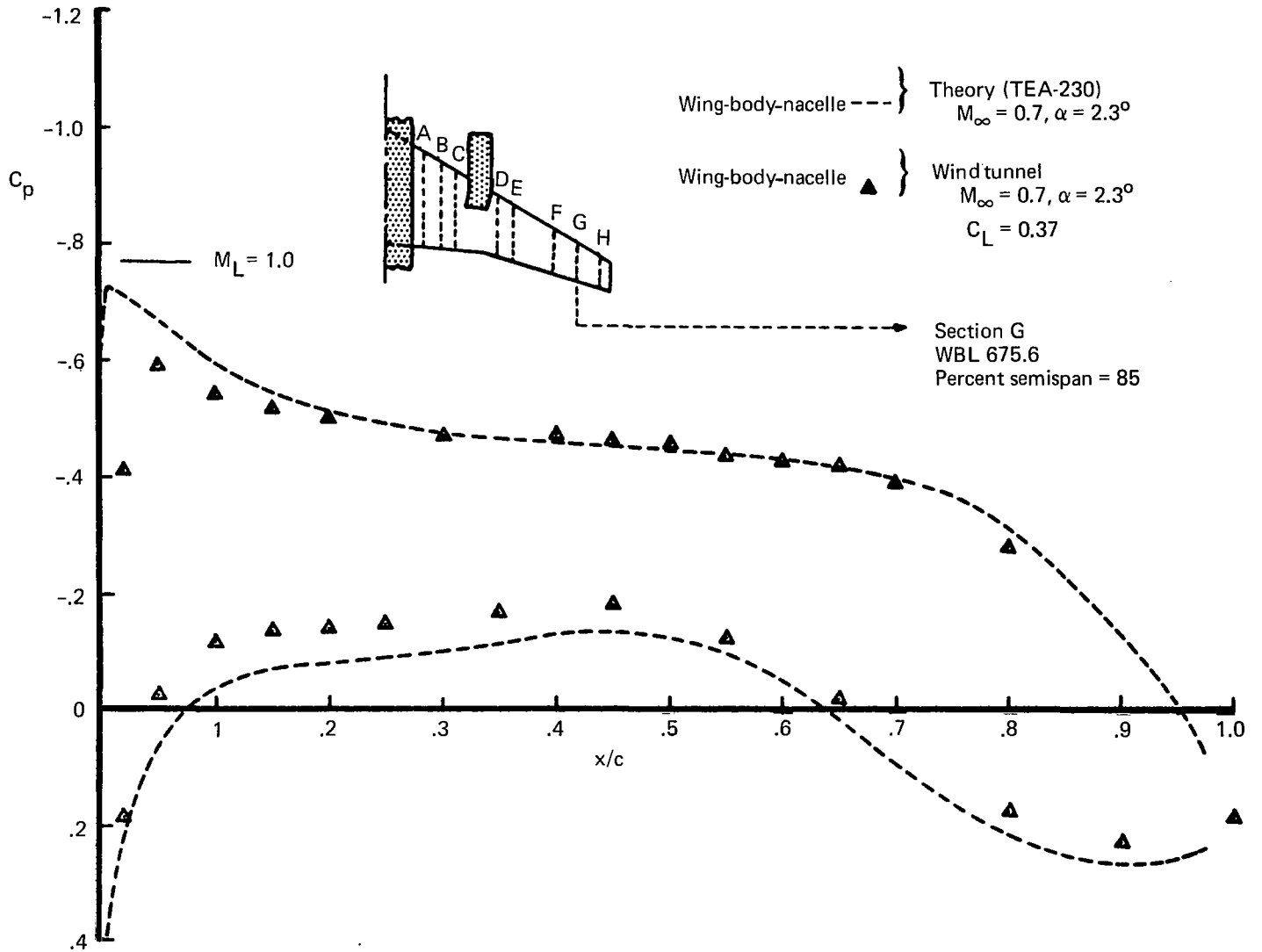

FIGURE 44.—COMPARISON OF WING PRESSURE DISTRIBUTION FROM TEA-230 ANALYSIS WITH WIND TUNNEL DATA—WING-BODY-NACELLE CONFIGURATION

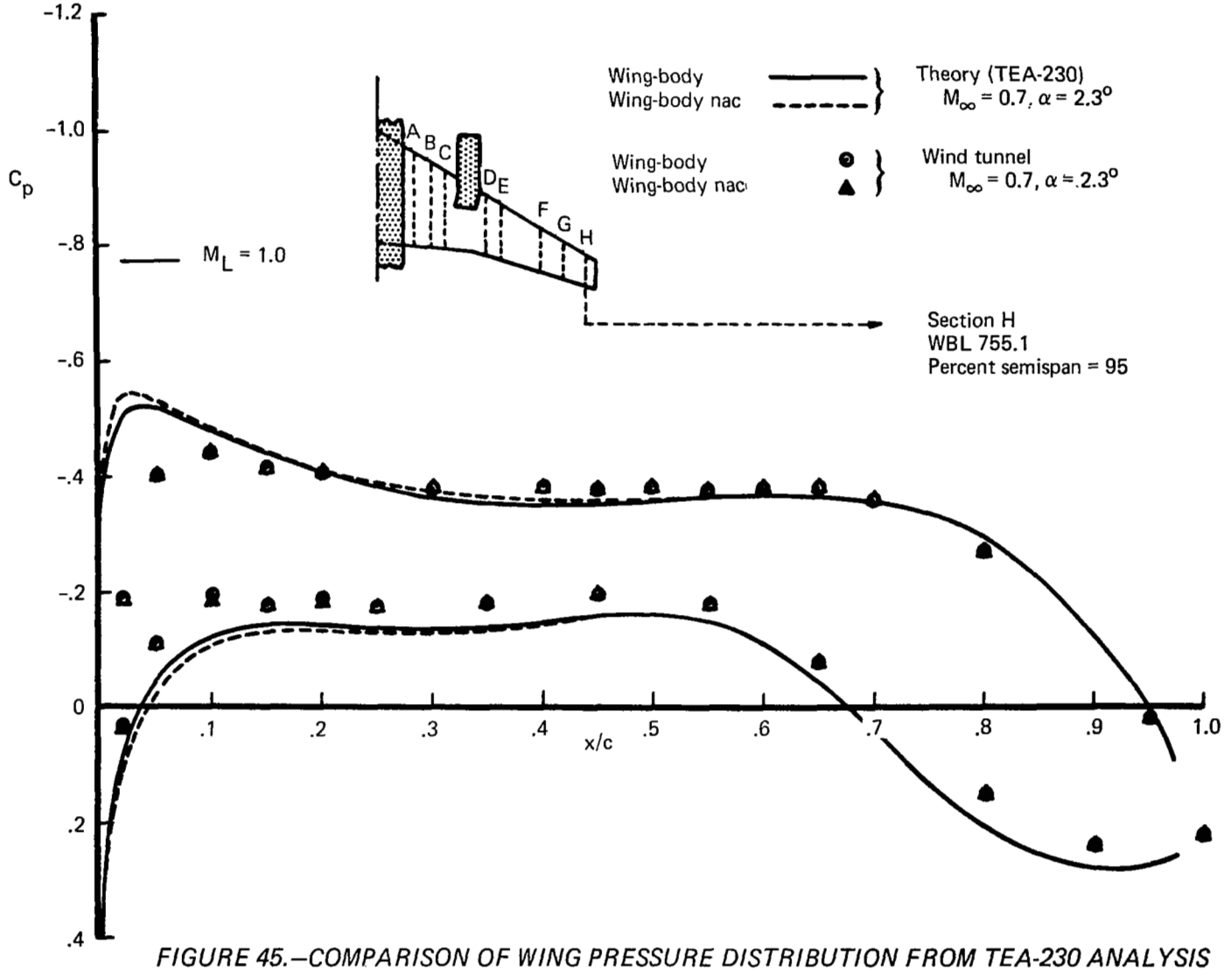

FIGURE 45.—COMPARISON OF WING PRESSURE DISTRIBUTION FROM TEA-230 ANALYSIS WITH WIND TUNNEL DATA—WING-BODY-NACELLE CONFIGURATION

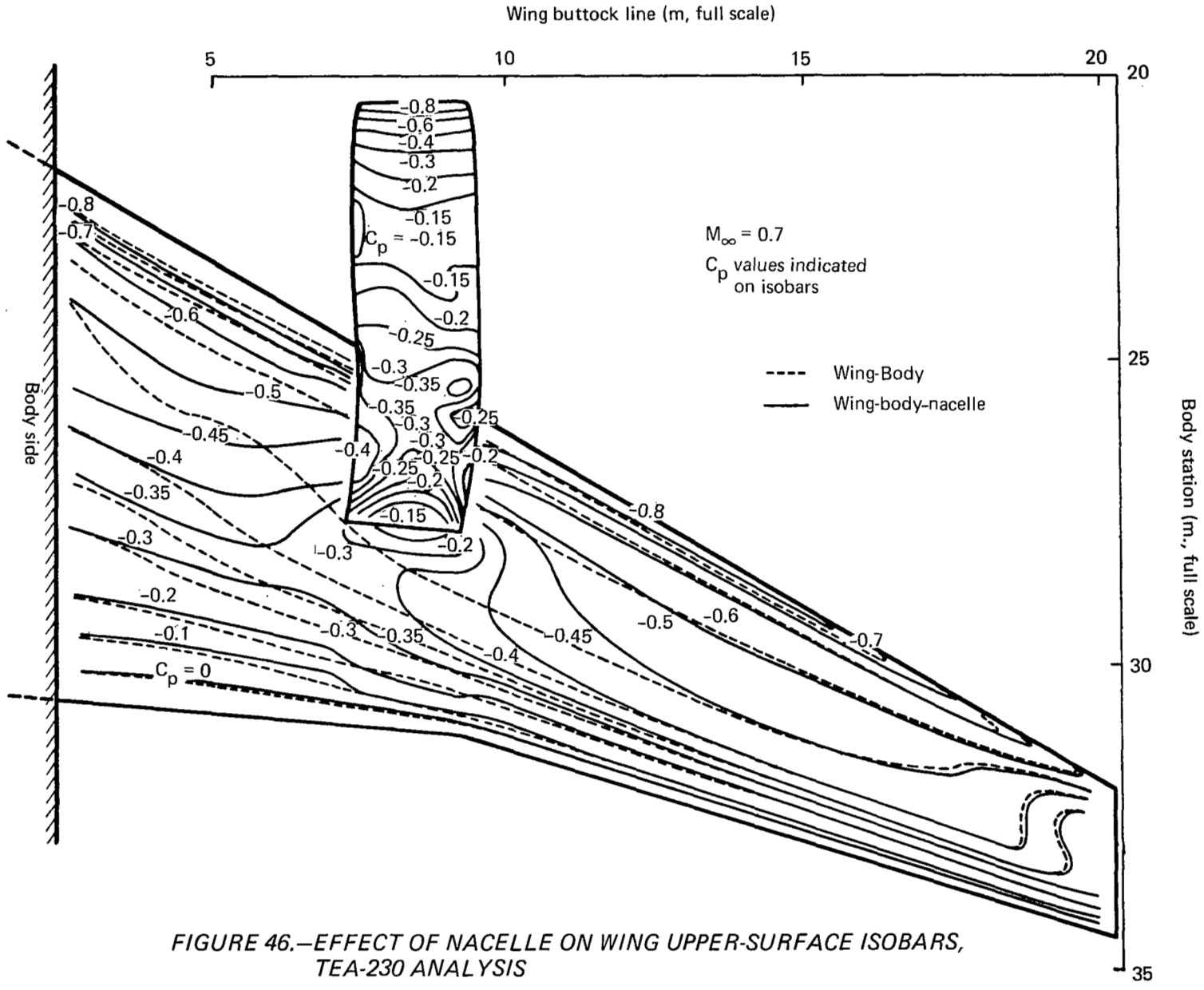

FIGURE 46.—EFFECT OF NACELLE ON WING UPPER-SURFACE ISOBARS, TEA-230 ANALYSIS

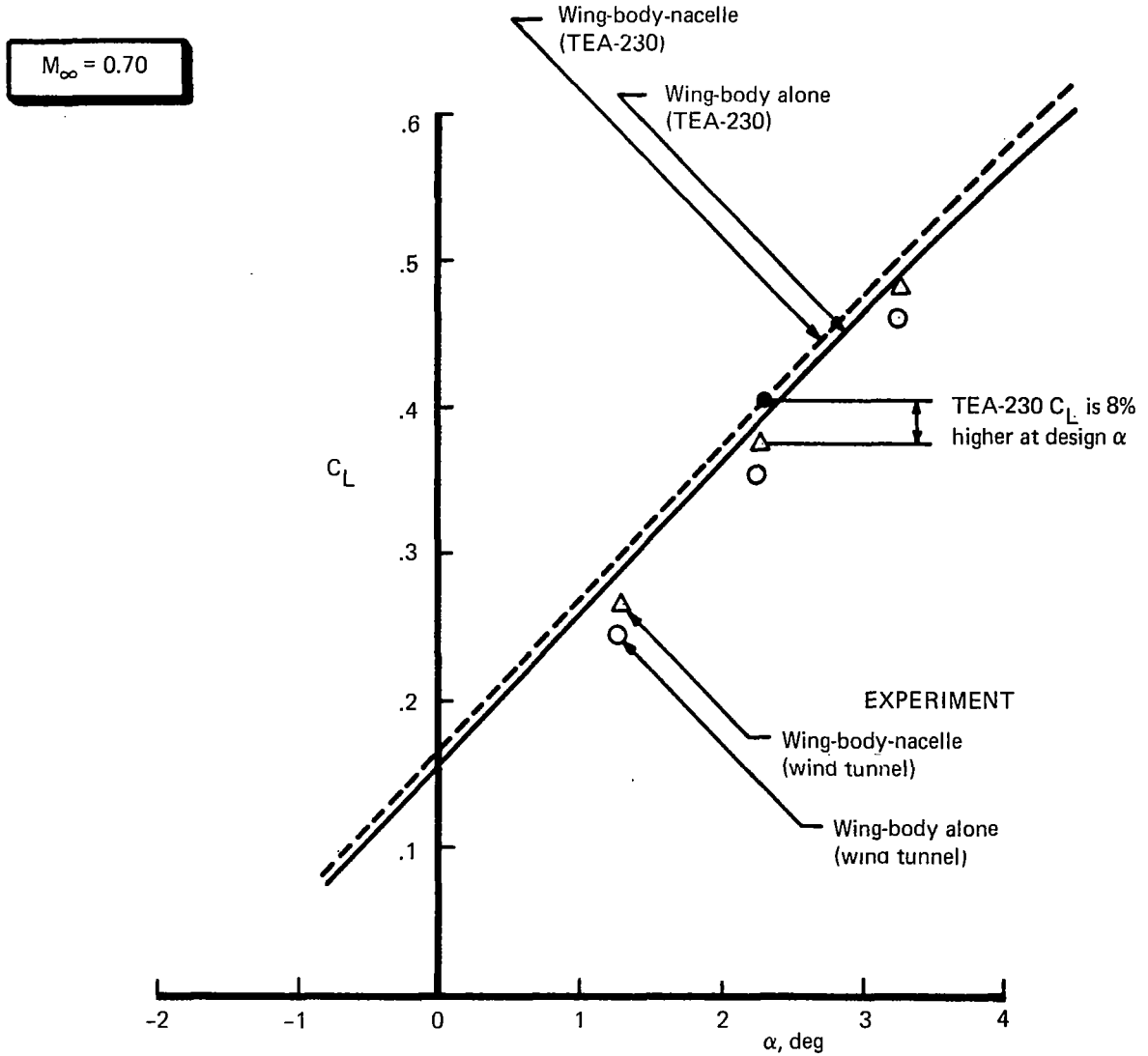

FIGURE 47.—EFFECT OF NACELLE ON WING-BODY LIFT CURVE—THEORY VS EXPERIMENT

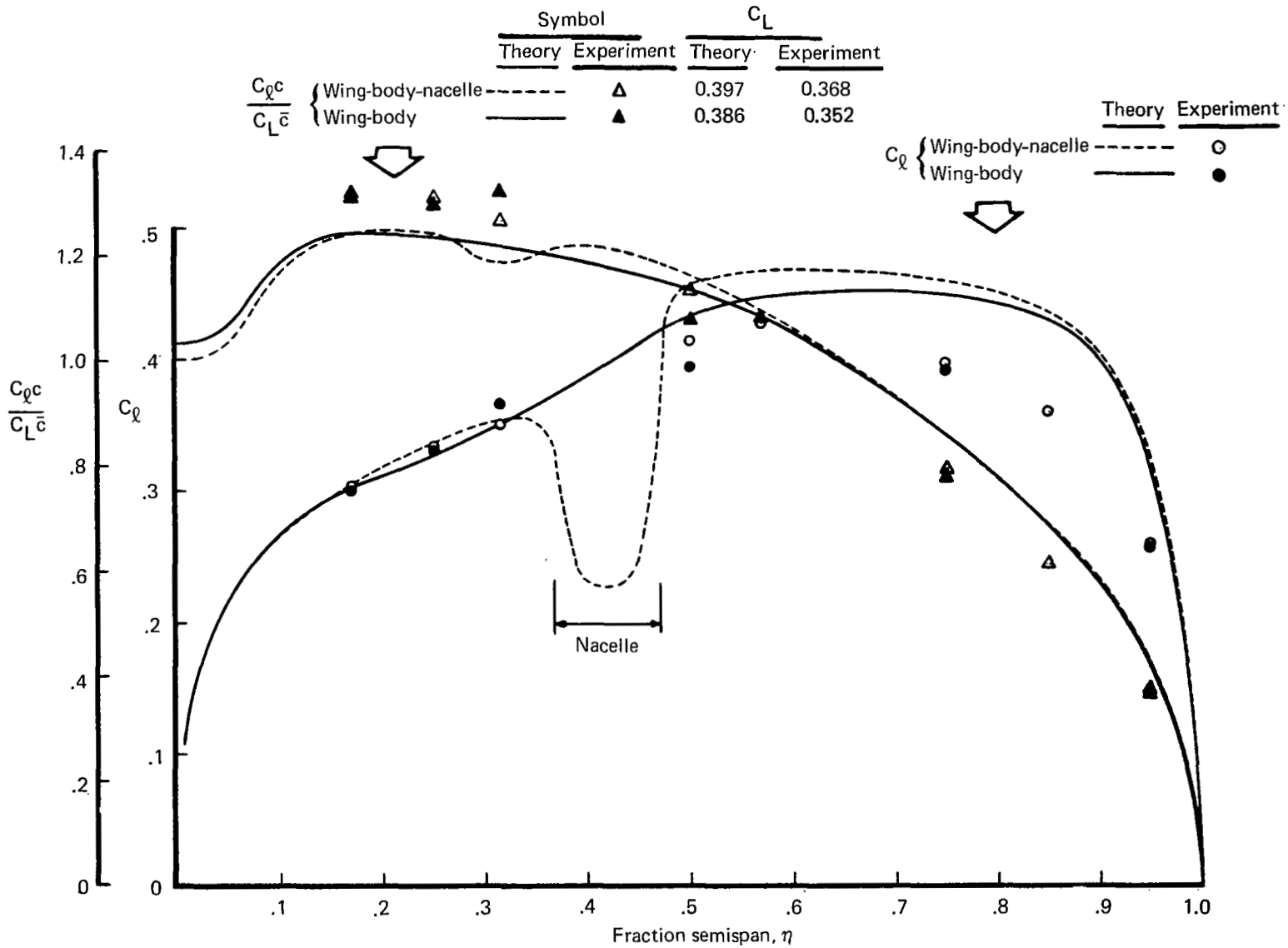

FIGURE 48.–EFFECT OF NACELLE ON WING LOAD DISTRIBUTION AND SECTIONAL LIFT DISTRIBUTION–THEORY VS EXPERIMENT

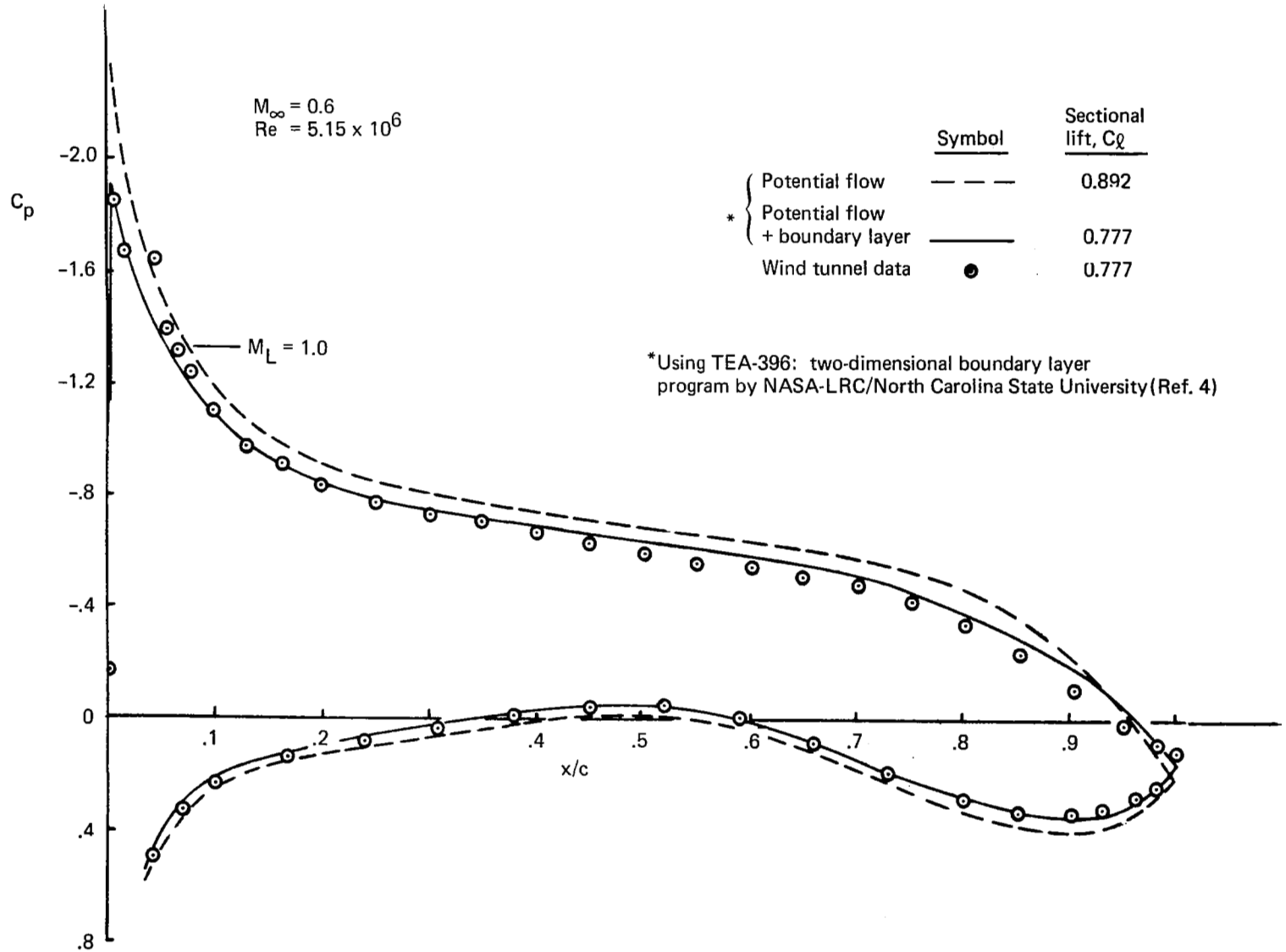

FIGURE 49.—EFFECT OF BOUNDARY LAYER ON POTENTIAL-FLOW C_p DISTRIBUTION OF TYPICAL REAR-LOADED AIRFOIL

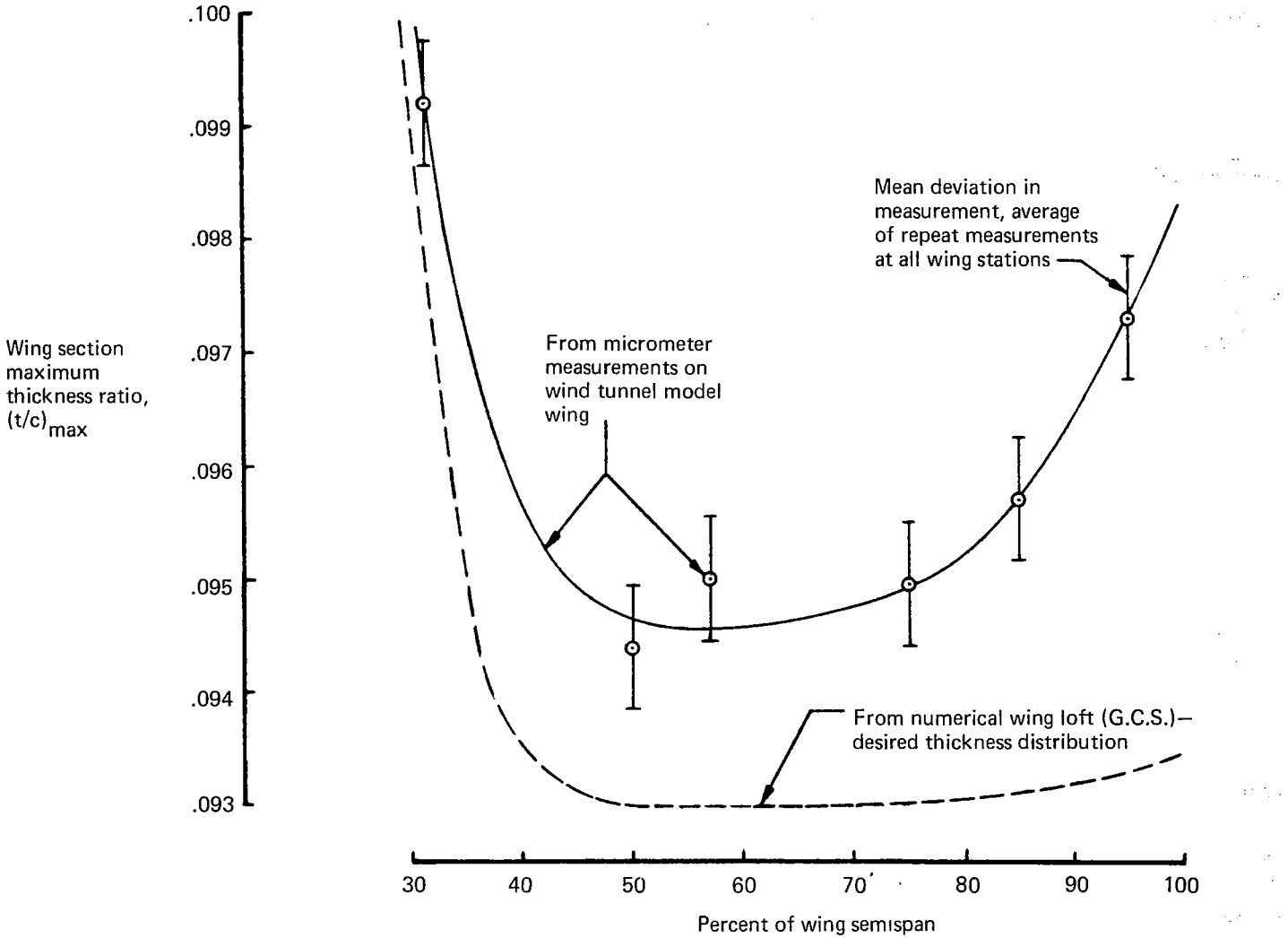

FIGURE 50.–DESIRED VS MEASURED MAXIMUM THICKNESS DISTRIBUTION ACROSS WIND TUNNEL MODEL WING

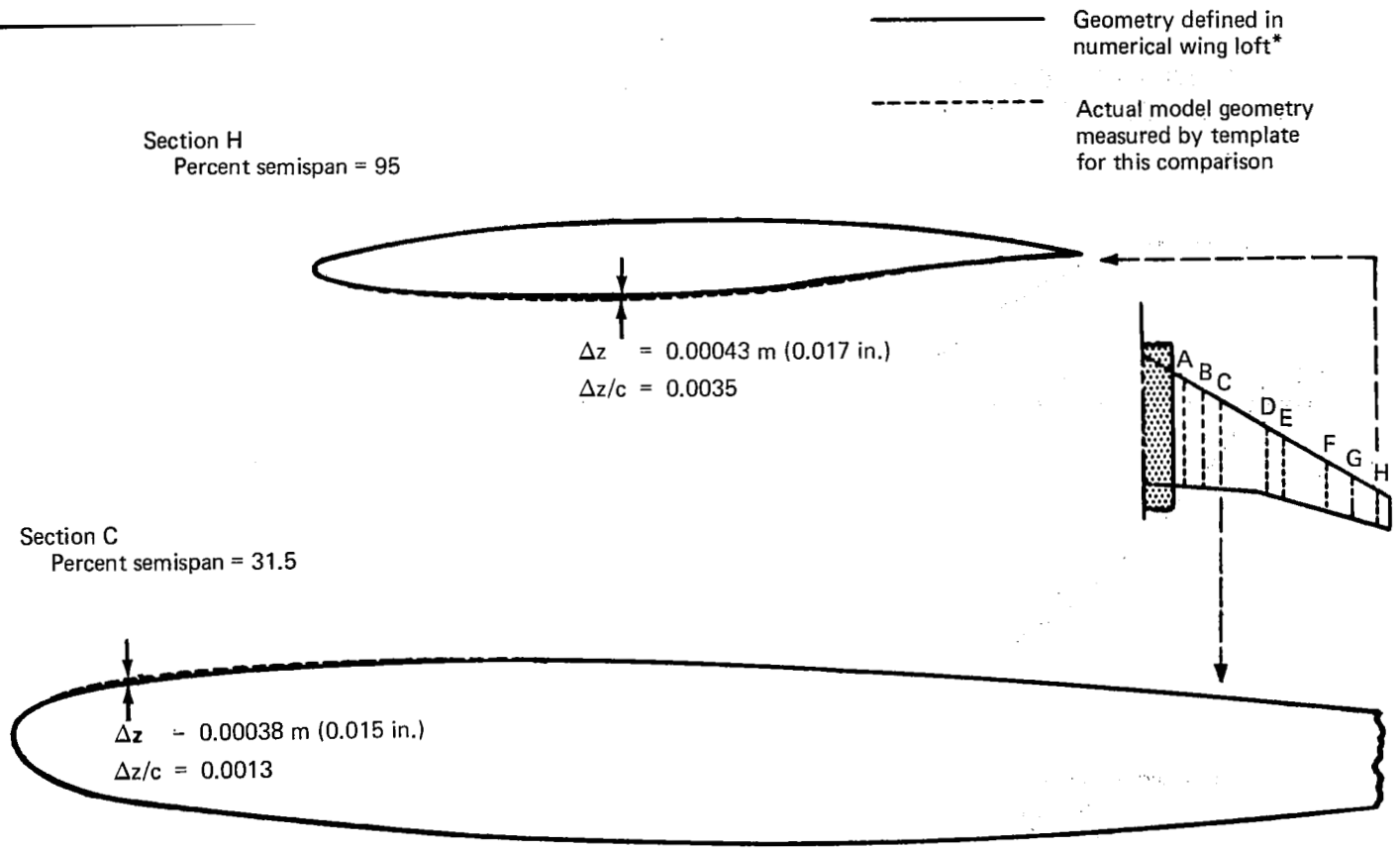

FIGURE 51.—LARGEST DEVIATIONS IN WIND TUNNEL WING MODEL GEOMETRY

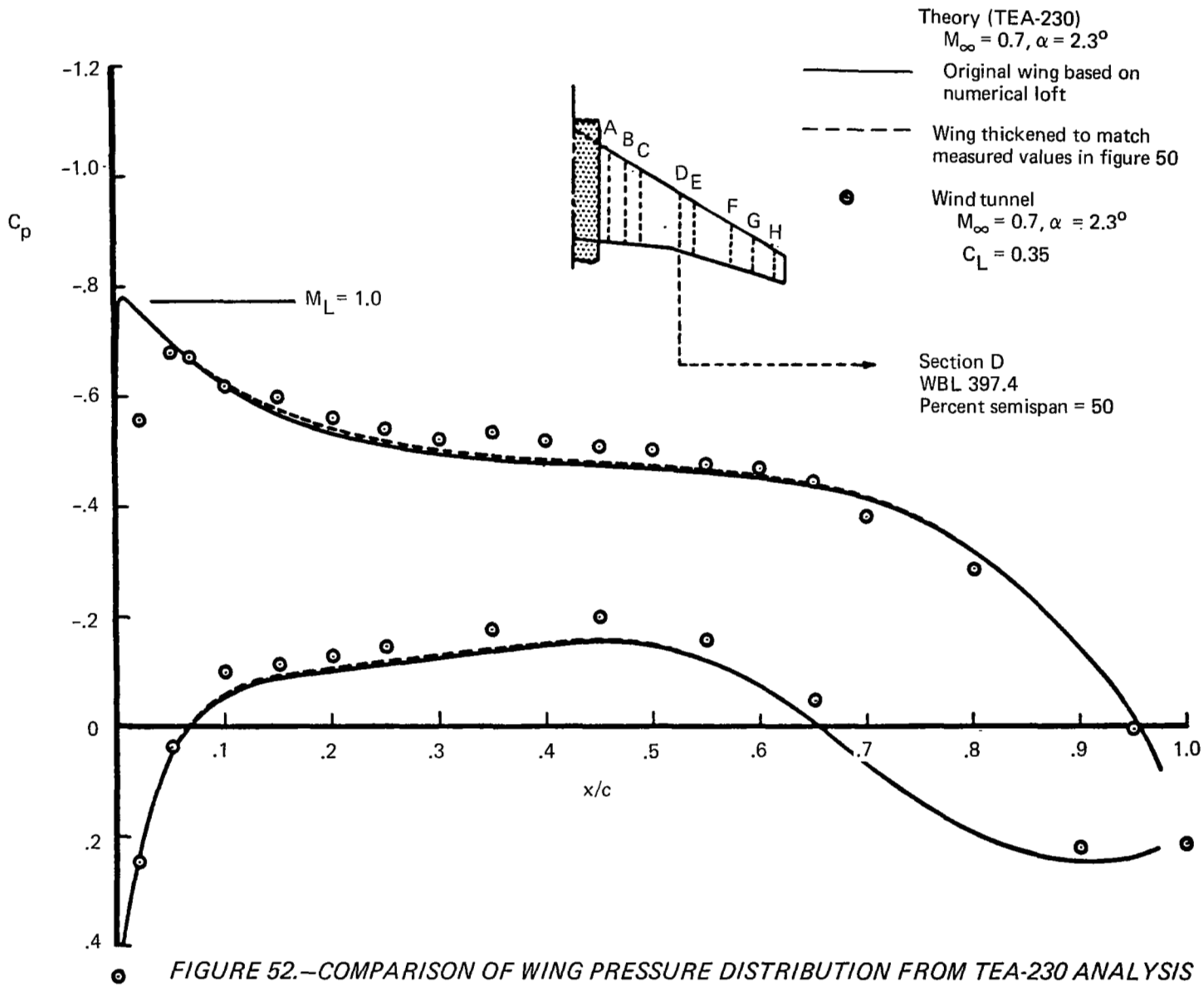

FIGURE 52.–COMPARISON OF WING PRESSURE DISTRIBUTION FROM TEA-230 ANALYSIS WITH WIND TUNNEL DATA, WING-BODY CONFIGURATION–EFFECT OF THICKER WIND TUNNEL MODEL WING

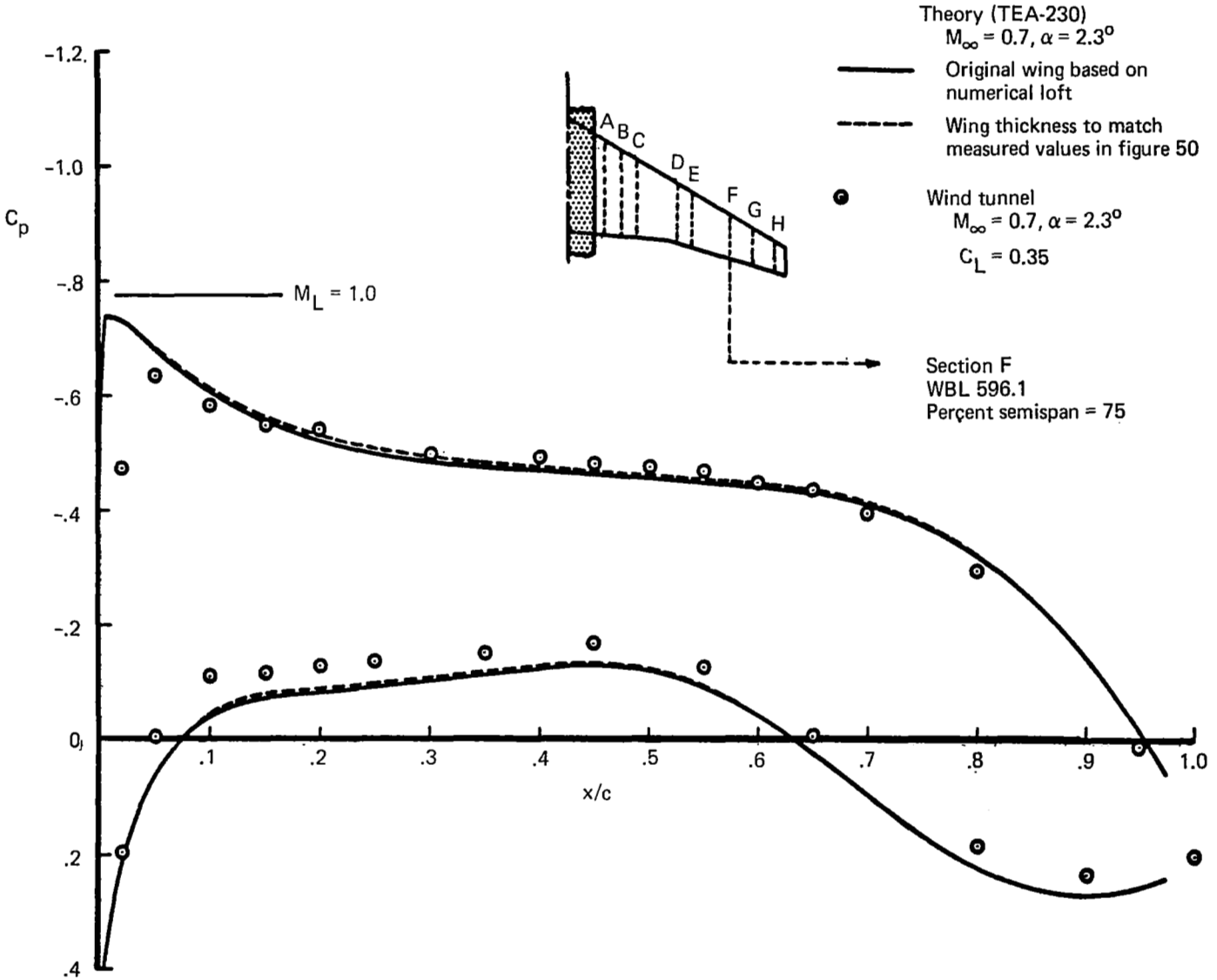

FIGURE 53.–COMPARISON OF WING PRESSURE DISTRIBUTION FROM TEA-230 ANALYSIS WITH WIND TUNNEL DATA, WING-BODY CONFIGURATION–EFFECT OF THICKER WIND TUNNEL MODEL WING

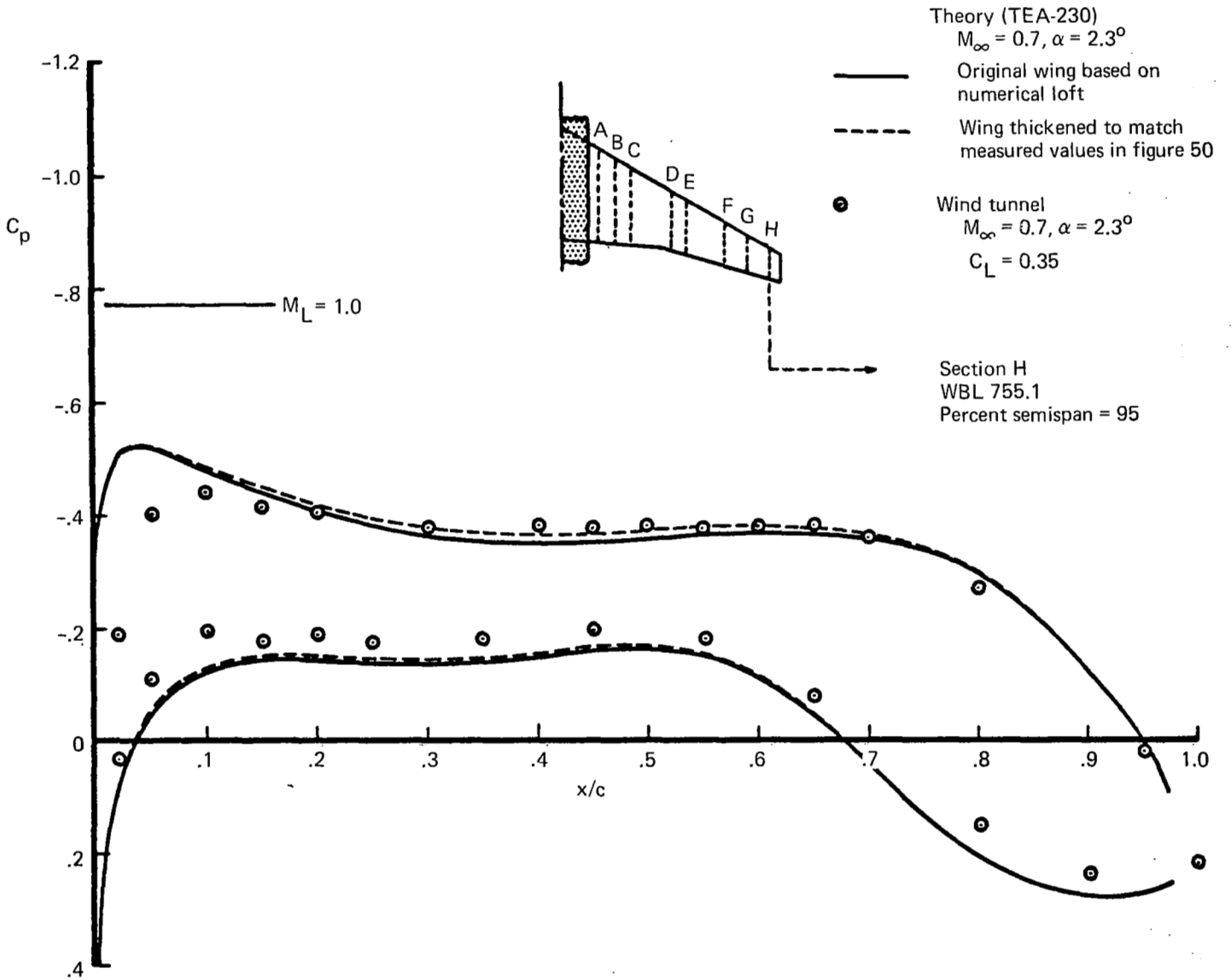

FIGURE 54.—COMPARISON OF WING PRESSURE DISTRIBUTION FROM TEA-230 ANALYSIS WITH WIND TUNNEL DATA, WING-BODY CONFIGURATION—EFFECT OF TUCKER WIND TUNNEL MODEL WING

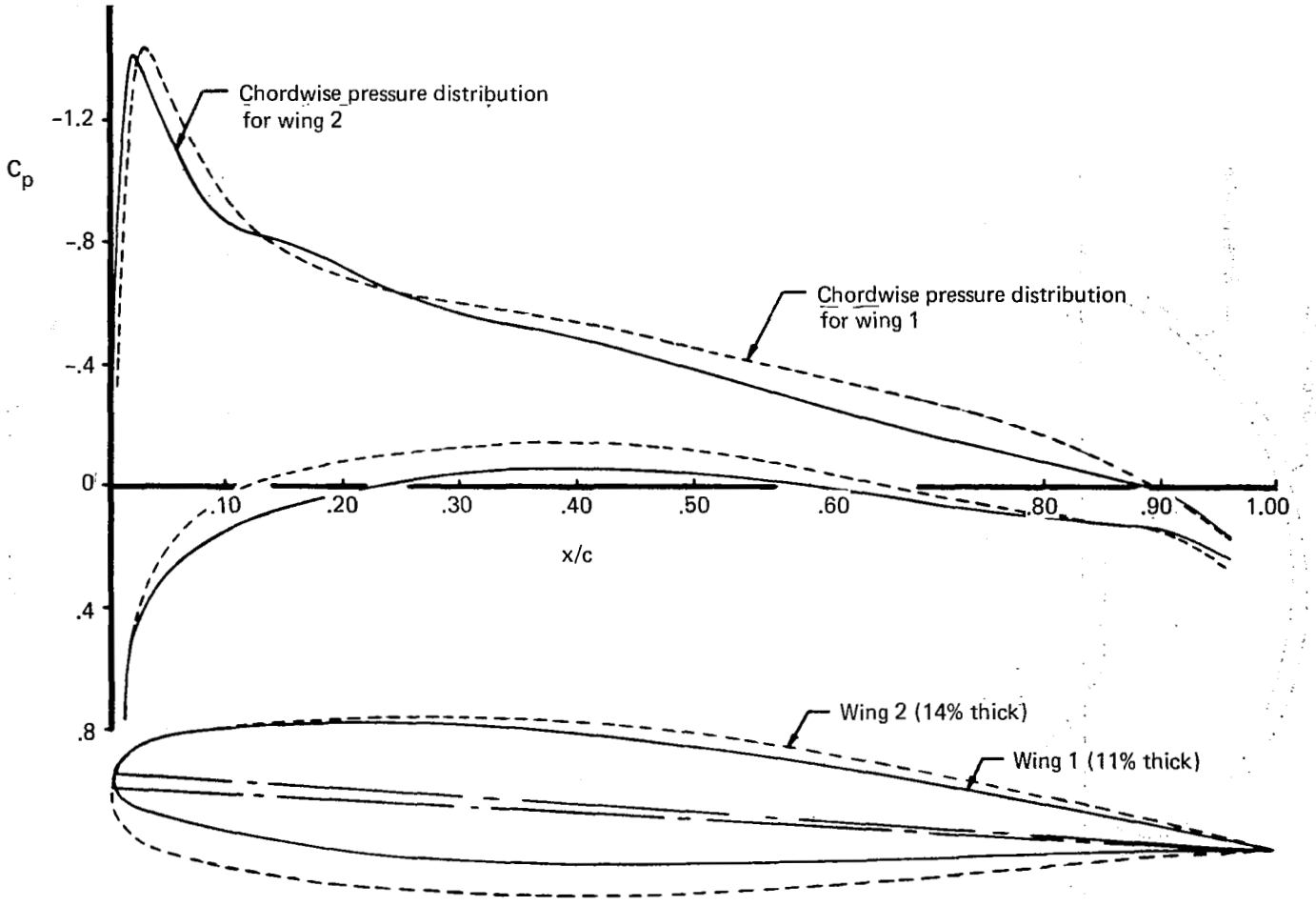

FIGURE 55.—POTENTIAL-FLOW PRESSURES FOR DIFFERENT WING SECTION SHAPES ON AN INFINITE YAWED WING OF 30° SWEEP

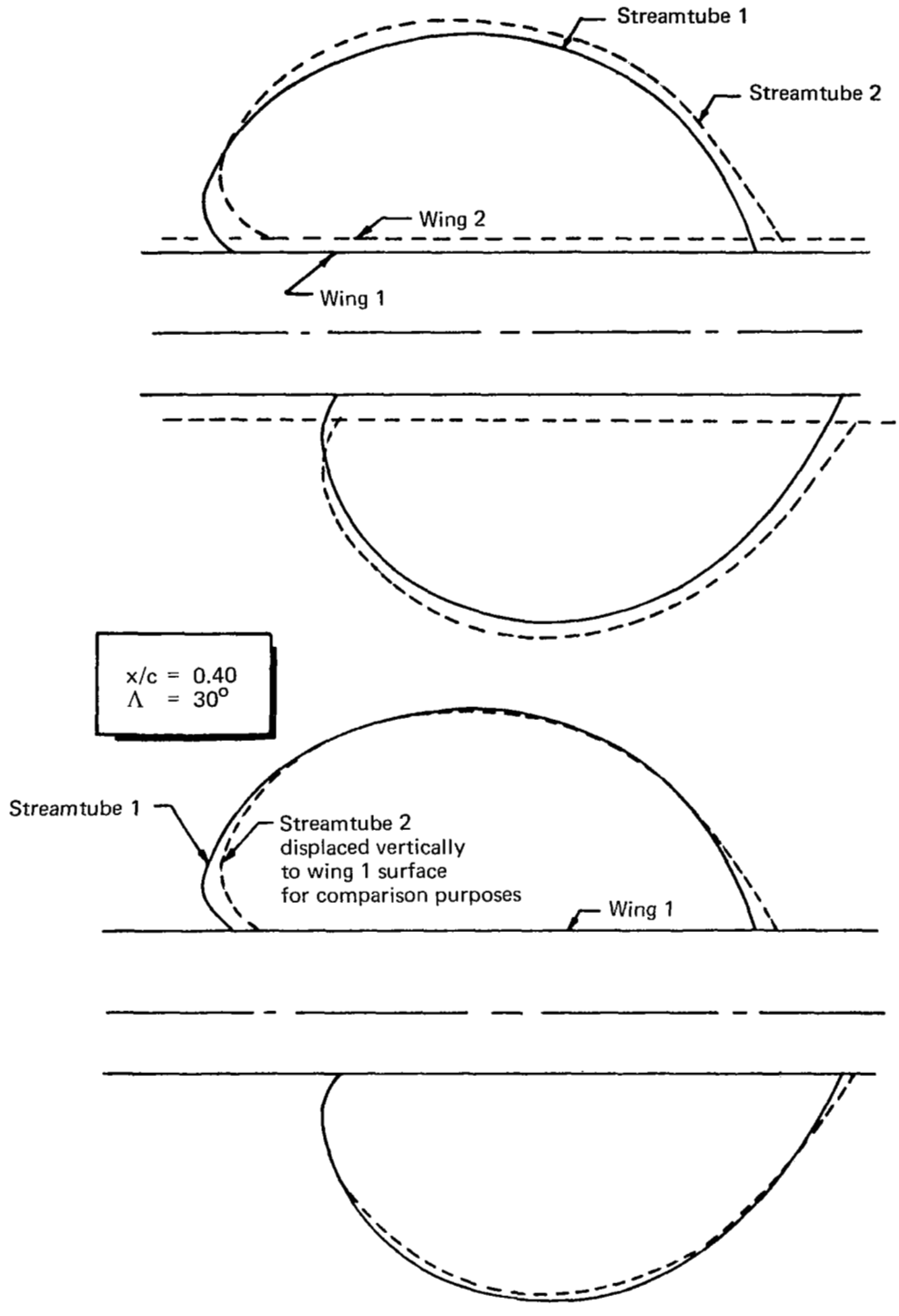

FIGURE 56.—EFFECT OF CHORDWISE PRESSURE DISTRIBUTION ON STREAMTUBE DISPLACEMENT

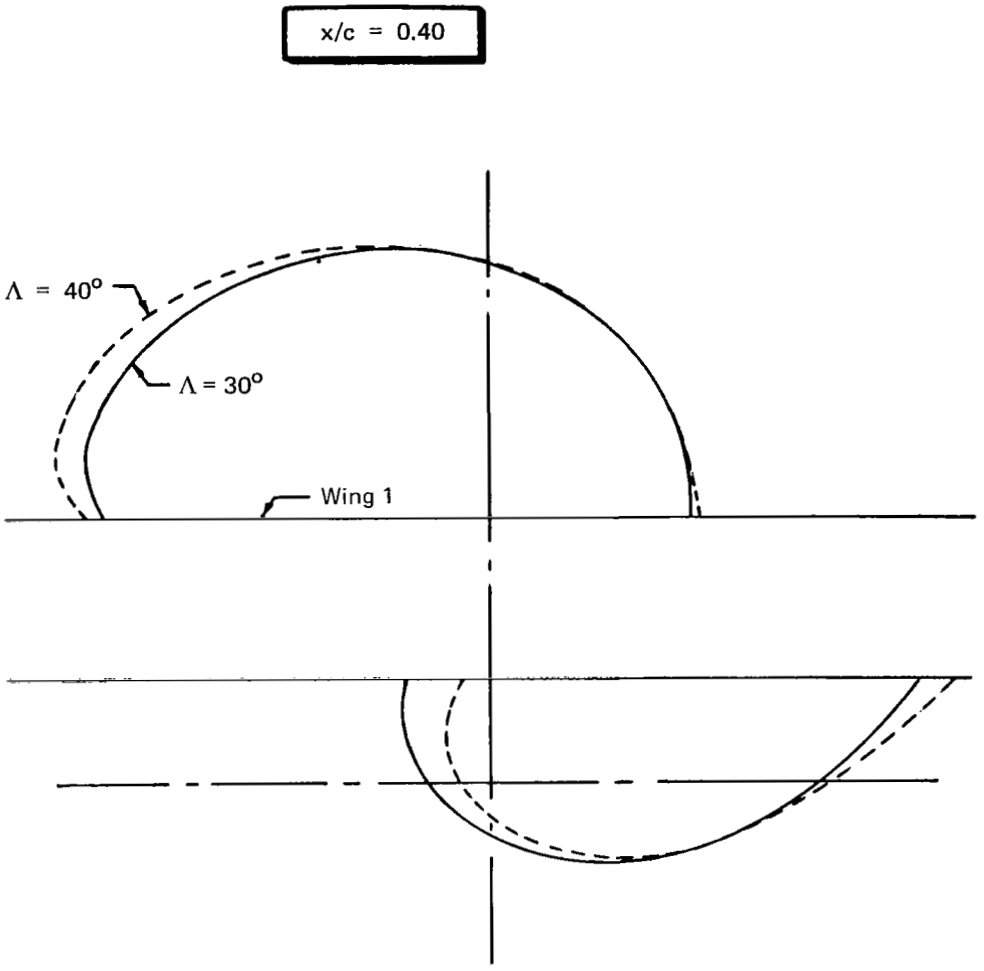

FIGURE 57.–EFFECT OF WING SWEEP ON STREAMTUBE DISPLACEMENT

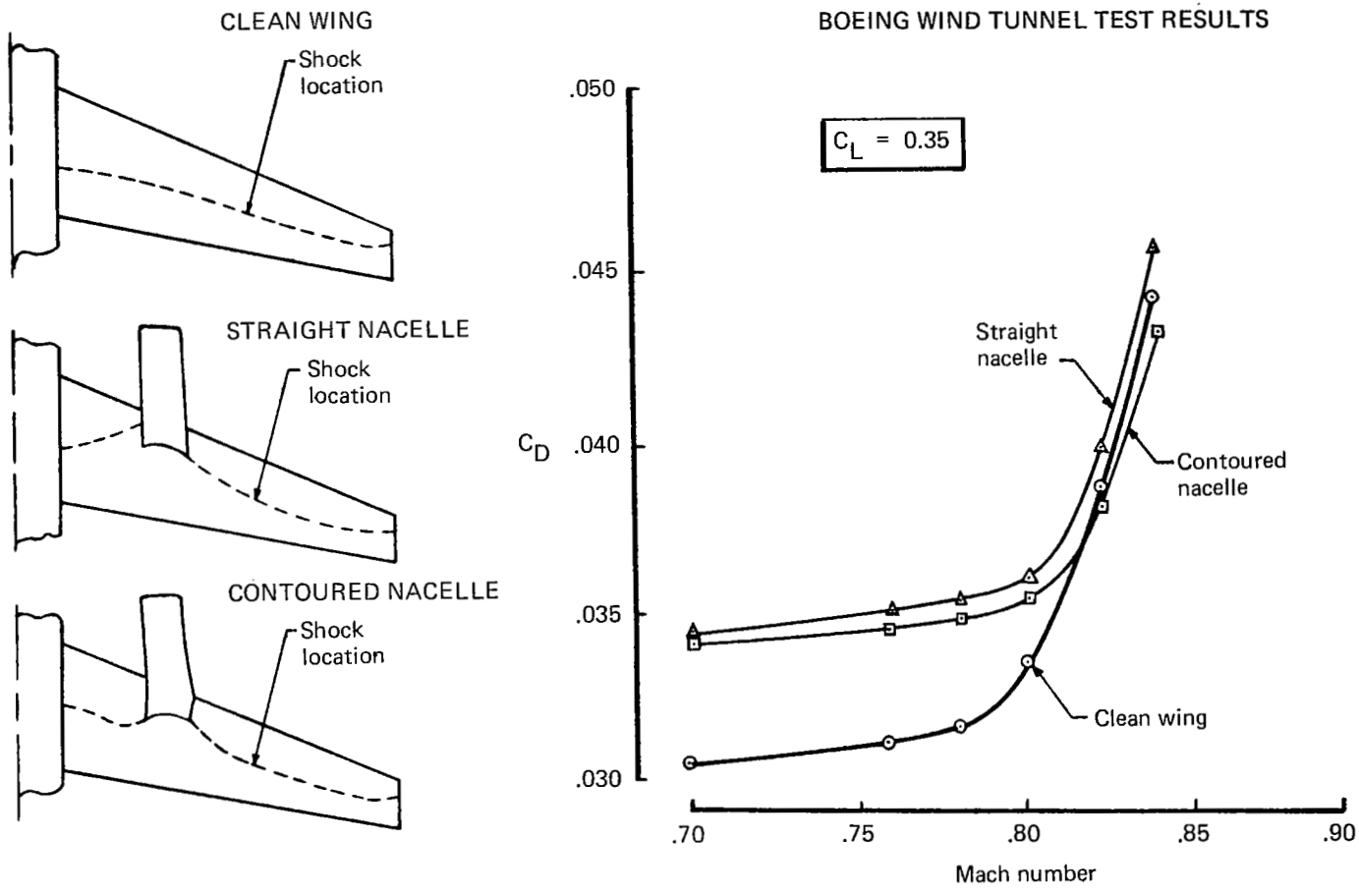

FIGURE 58.—INSTALLATION OF OVERWING ENGINE ON HIGH-SPEED WING

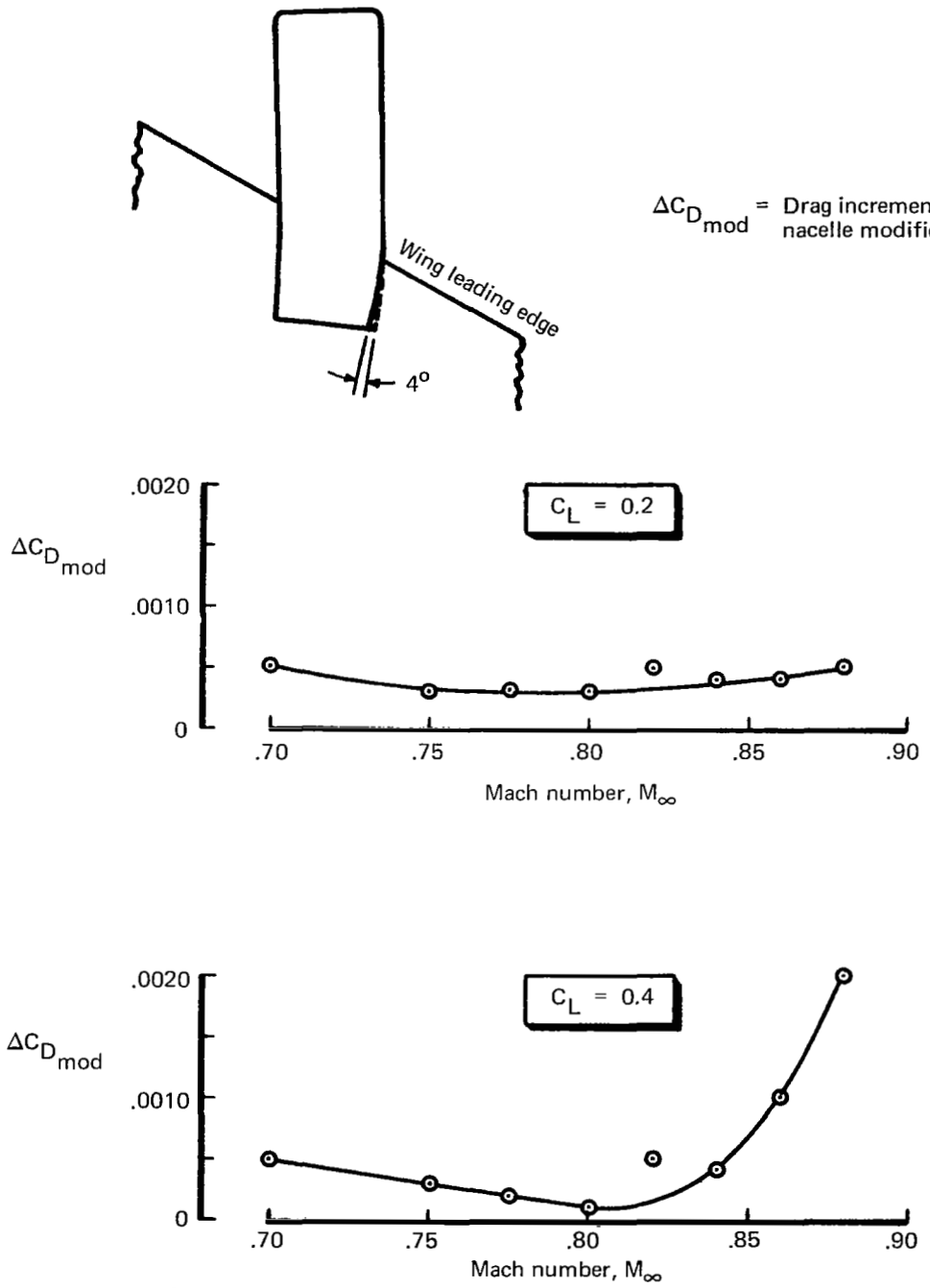

FIGURE 59.–EFFECT OF REDUCED OUTBOARD BOATTAIL ON NACELLE DRAG

REFERENCES

1. Gillette, W. B.; Mohn, L. W.; Ridley, H. G.; and Nark, T. C.: *Upper-Surface Blowing Nacelle Design Study for a Swept Wing Airplane at Cruise Conditions.* NASA CR-2427, September 1974.

2. Rubbert, P. E.; and Saaris, G. R.: "Review and Evaluation of a Three Dimensional Lifting Potential Flow Analysis Method for Arbitrary Configurations." Paper presented at AIAA 10th Aerospace Sciences Meeting, San Diego, California, January 1972.

3. Rubbert, P. E., et al: *A General Method for Determining the Aerodynamic Characteristics of Fan-in-Wing Configurations.* Volume 1, Theory and Application. Technical report 67-61A, USAAVLABS, 1967.

4. Smetana, F. D., et al: *Aircraft Lift, Drag, and Moment Prediction: A Review and Analysis.* NASA CR-2523, to be released.